

---

# Molecule Detection by Resonantly Enhanced Third Harmonic Generation of Mid-Infrared Laser Pulses

---

Moleküldetektion durch resonant überhöhte Frequenzverdreifachung mittelinfraroter Laserpulse  
Dissertation von Jan Frederic Kinder, September 2021



TECHNISCHE  
UNIVERSITÄT  
DARMSTADT

Fachbereich Physik  
Institut für Angewandte Physik  
Nichtlineare Optik / Quantenoptik



# **Molecule Detection by Resonantly Enhanced Third Harmonic Generation of Mid-Infrared Laser Pulses**

Vom Fachbereich Physik  
der Technischen Universität Darmstadt

zur Erlangung des Grades  
eines Doktors der Naturwissenschaften  
(Dr. rer. nat.)

genehmigte Dissertation von  
M.Sc. Jan Frederic Kinder  
aus Dieburg

Referent: Prof. Dr. Thomas Halfmann  
Korreferent: Prof. Dr. Thomas Walther

Tag der Einreichung: 30. September 2021

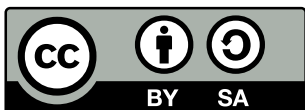
Tag der Prüfung: 10. November 2021

Darmstadt 2021

D17

Jan Frederic Kinder: Molecule Detection by Resonantly Enhanced Third Harmonic  
Generation of Mid-Infrared Laser Pulses  
Darmstadt, Technische Universität Darmstadt  
Jahr der Veröffentlichung der Dissertation auf TUPrints: 2021  
URN: urn:nbn:de:tuda-tuprints-199622

Tag der mündlichen Prüfung: 10. November 2021



Veröffentlicht unter CC BY-SA 4.0 International - Creative Commons, Attribution  
Share-alike

<https://creativecommons.org/licenses/by-sa/4.0/>

---

# Contents

<b>Introduction</b>	<b>1</b>
<b>1 Basic theory of resonantly enhanced THG in molecules</b>	<b>3</b>
1.1 THG with focused Gaussian beams	3
1.2 Nonlinear susceptibility and resonance enhancement	5
1.3 Phasematching considerations	7
<b>2 Experimental setup</b>	<b>10</b>
2.1 Laser system	10
2.1.1 Preamplifier OPA stage	12
2.1.2 Power OPA stage	14
2.1.3 Spectral linewidth of the OPA output	17
2.2 Relevant spectroscopic properties of HCl	19
2.3 Sample gas setup	23
2.4 Focusing conditions	24
2.5 Detection setup	25
2.5.1 Calibration of the mid-infrared monitoring setup	26
2.5.2 Calibration of the THG detection setup	27
<b>3 Experimental results of THG</b>	<b>31</b>
3.1 Spectroscopic investigations	31
3.1.1 Two-photon resonance	34
3.1.2 Three-photon resonance	37
3.2 Intensity dependence	38
3.3 Pressure dependence of the THG signal	40
3.3.1 THG spectra at low HCl pressures	40
3.3.2 THG simulation	43
3.3.3 Pressure dependence	44
3.3.4 Discussion of the detection limit	45
3.4 Collisional broadening and shifts	47
3.4.1 Line broadening mechanisms	47
3.4.2 Self-broadening of two- and three-photon resonances	49
3.4.3 Foreign-gas broadening	51
3.4.4 Pressure-induced shifts	52
3.5 Conclusion	53
<b>4 Experimental results of SFM</b>	<b>54</b>
4.1 SFM Simulation	55
4.2 Experimental setup	57
4.3 SFM spectroscopy	59
4.4 Intensity dependence	62
4.5 Analysis of the SFM background signal	62
4.6 Pressure dependence of the SFM signal	65

4.7 Conclusion . . . . .	69
<b>Conclusion and outlook</b>	<b>70</b>
<b>Zusammenfassung</b>	<b>72</b>
<b>Appendix</b>	<b>74</b>
A Refractive index of HCl . . . . .	74
B Pressure sensor . . . . .	75
C Simulation results for CO <sub>2</sub> . . . . .	76
<b>Bibliography</b>	<b>77</b>
<b>Publications and contributions to conferences</b>	<b>82</b>
<b>Supervisions and contributions to teaching</b>	<b>83</b>
<b>Erklärung gemäß §9 Promotionsordnung</b>	<b>85</b>

# Introduction

Nonlinear laser spectroscopy offers a variety of techniques for sensitive detection of molecular species, with a multitude of applications in trace gas analysis [1], combustion diagnostics [2], environmental sensing [3], or microscopy [4]. Stimulated Raman scattering (SRS) or coherent anti-Stokes Raman scattering (CARS) are commonly used for such purposes [5–7]. CARS relies on a resonantly enhanced four-wave mixing process, driven by a pump laser pulse and a Stokes laser pulse, typically with wavelengths in the visible regime. The laser wavelengths are tuned to two-photon resonance with vibrational states in the electronic ground state of a molecular species, generating a signal pulse. The signal yield in CARS benefits from the large transition dipole moment between the electronic ground and electronic excited states, as well as two-photon resonance with vibrational states. However, the pump and Stokes laser are usually very far detuned (typically in the range of many  $1000 - 10000 \text{ cm}^{-1}$ , expressed in units of wave numbers) from the single-photon transition to the excited electronic state. As two photons from the pump laser are involved in the frequency conversion process of CARS, these large detunings appear twice as limiting factors in the third-order nonlinear polarization, which greatly reduces the achievable signal strength. Moreover, CARS typically requires two laser pulses. Thus, for applications in trace gas detection it would be desirable to find an alternative nonlinear technique, which requires only a single driving laser beam and permits operation at small (or zero) detunings at *all* single- and multi-photon transitions, involved in the frequency conversion process, thereby enabling a large signal yield.

Third harmonic generation (THG) is the lowest-order frequency conversion process, which occurs in any medium [8]. THG is a degenerate four-wave mixing process, i.e., it requires only a single driving field. The signal frequency is three times the fundamental frequency, hence, separation of the fundamental and signal fields is straightforward. Maker and Terhune first experimentally demonstrated THG in 1965 [9]. Off-resonant THG does not give spectral selectivity, which is required to detect atomic or molecular species. THG via resonances enhances the signal yield [10] and provides the required spectral selectivity. It is a parametric process, i.e., no energy from the incident fundamental radiation is deposited in the sample. This makes THG very well suited to investigate sensitive samples (e.g., from biology), and it meanwhile evolved into a standard technique for laser-based, nonlinear microscopy [11, 12].

Resonant THG at vibrational transitions is a promising route towards trace molecule detection under realistic conditions. We note, that shortly after experimental implementations of resonantly enhanced THG in atomic vapors the potential of the method was proposed for molecules, which possess strong vibrational resonances in the mid-infrared region leading to high nonlinear susceptibilities [13, 14]. Already in 1976 first experimental realizations were demonstrated using  $\text{CO}_2$  lasers in  $\text{SF}_6$  and  $\text{CO}$  [15]. However, these experiments were limited to few transitions, accessible with  $\text{CO}_2$  lasers. The nonlinear process requires sufficiently intense laser pulses with tunability in the mid-infrared (i.e., in the regime of so-called vibrational "fingerprint" spectra) and narrow spectral bandwidth  $< 1 \text{ GHz}$  (i.e., to maintain spectral selectivity also for

closely spaced resonances, e.g., from neighboring states [16]). Such laser systems became only available in the last decades, mostly in home-made experimental setups and with spectral bandwidths typically still quite far above the Fourier-transform limit [17]. Recently, Miyamoto *et al.* applied a narrowband, mid-infrared laser system for coherent two-photon excitation and THG in hydrogen molecules [18]. However, the latter experiment was implemented in cryogenically cooled molecules at large pressures around 1 bar, thus, far beyond realistic conditions for trace detection, and THG was studied on a single resonance only. Hence, in this work, we implement resonantly enhanced THG with narrowband mid-infrared fundamental radiation for molecule detection of hydrogen chloride (HCl) and compare it to a numerical simulation.

As an extension we consider a second approach to molecule detection. Two-photon resonant sum frequency mixing (SFM) combines the benefits of resonantly enhanced THG and CARS. For THG, we enhance the nonlinear susceptibility with vibrational resonances. Hence, all detunings are low, but the transition dipole moments are orders of magnitude smaller than the electronic transition dipole moments, which CARS takes advantage of, albeit with large detunings. We propose an approach in between THG and CARS: We resonantly excite a molecule to a two-photon resonance and add a second, intense, fixed-frequency laser field with a lower wavelength. Hence, we benefit from low single- and two-photon detunings as well as large electronic transition dipole moments. Pellin and Yardley originally suggested this method and calculated the nonlinear susceptibility in HCl [14]. Dolzhikov *et al.* conducted experimental studies in various molecules [19]. However, due to the lack of continuously tunable, narrowband laser sources in the mid-infrared we found no further studies on this method, even though calculations highlighted the potential [20]. Recently, Traverso *et al.* applied a related approach to enhance the nonlinear susceptibility of Raman scattering via a two-photon vibrational resonance in methane molecules [21]. However, the authors operated with broadband picosecond pulses, which do not provide the spectral resolution necessary to resolve rotational transitions, which can be applied, e.g., to determine the temperature of the sample.

This work is structured in four chapters. First, we describe the basic theory of third harmonic generation in molecular gases. In the second chapter, we characterize the experimental setup, which is necessary to generate continuously tunable narrowband mid-infrared nanosecond laser pulses. Further, we discuss the electronic, vibrational, and rotational energy structure for our sample molecule HCl. We discuss the detection setup for mid-infrared and near-infrared signal pulse energies. In the third chapter, we present and discuss experimental data of resonantly enhanced THG in HCl. In systematic studies, we check the intensity and pressure dependencies of the THG signal. We discuss the detection limit for HCl molecules and investigate pressure-induced broadening and line-shifts. Finally, we present the results of a first test of SFM in HCl and compare the results of both approaches.

# Chapter 1

## Basic theory of resonantly enhanced THG in molecules

In this chapter we introduce the basic theoretical framework for nonlinear frequency conversion in molecular gases. We consider the example of THG, i.e., the lowest order frequency conversion process present in isotropic media. Our goal is the explicit calculation of the power of the third harmonic field, which emerges from the sample gas HCl under excitation with focused laser pulses. We find from a quantum mechanical description of the nonlinear susceptibility, that molecular resonances enhance the THG energy by orders of magnitude. We also analyse the focus geometry to find the optimal parameters for an experimental implementation. A more comprehensive treatment on nonlinear frequency conversion can be found in textbooks [8, 22, 23] and review articles [24, 25].

### 1.1 THG with focused Gaussian beams

Starting with the Maxwell equations we formulate the wave equation of nonlinear optics. For a compact discussion, we discuss assumptions and approximations: We assume the nonlinear medium to be nonmagnetic, isotropic and free of charges and free currents. These assumptions are valid for a thin molecular gas. We further assume the electric field  $E$  to propagate in  $z$  direction. The wave equation is [8]

$$\Delta E(z, t) - \frac{1}{c_0^2} \frac{\partial^2}{\partial t^2} E(z, t) = \frac{1}{\epsilon_0 c_0^2} \frac{\partial^2}{\partial t^2} P(z, t), \quad (1.1)$$

with the speed of light in vacuum  $c_0$  and the vacuum permittivity  $\epsilon_0$ . Note, that we discuss scalar quantities. In general the electric field  $E(z, t)$  and the polarization  $P(z, t)$  are vector quantities. We consider the polarization  $P(z, t)$  as a power series in the electric field strength [8]

$$P = \epsilon_0 \chi^{(1)} E + \epsilon_0 \chi^{(2)} E^2 + \epsilon_0 \chi^{(3)} E^3 + \dots \quad (1.2)$$

In general, the susceptibilities are multidimensional tensors. We consider scalar quantities, which are selected by symmetry consideration for an isotropic medium and permutations of the frequencies of the involved fields. We separate the expression for the polarization into the linear component  $P_1 = \epsilon_0 \chi^{(1)} E$  and all nonlinear contributions  $P_{\text{NL}} = \epsilon_0 \chi^{(2)} E^2 + \epsilon_0 \chi^{(3)} E^3 + \dots$ . With this definition we formulate the nonlinear wave equation, including dispersion, as

$$\Delta E(z, t) - \frac{n^2}{c_0^2} \frac{\partial^2}{\partial t^2} E(z, t) = \frac{1}{c_0^2} \frac{\partial^2}{\partial t^2} P_{\text{NL}}(z, t), \quad (1.3)$$

with the linear refractive index  $n = \sqrt{1 + \chi^{(1)}}$ , which contains the linear susceptibility  $\chi^{(1)}$ . When we apply Eqn. (1.3) to molecular gases, we can assume an isotropic medium, i.e., the second order susceptibility  $\chi^{(2)}$  is negligible in most cases.  $\chi^{(3)}$  is the lowest order nonlinear susceptibility that is present in every medium. We restrict our further discussions on the THG process, which we implemented in the experiment. Hence, we describe the susceptibilities  $\chi^{(1)}$  and  $\chi^{(3)}$  in more detail in the following sections.

It is convenient to express Eqn. (1.3) in a frame defined by the propagation direction  $z$  and radius  $r$  (in polar coordinates), which parameterize the transversal profile of the electric field. We choose the ansatz  $E(z, t) = A(r, z) \exp[i(kz - \omega t)] + c.c.$  for the electric field with the wave vector  $k$  and  $P_{\text{NL}}(z) = p_{\text{NL}}(z, t) \exp[i(k'z - \omega' t)] + c.c.$  for the nonlinear polarization. We apply the slowly varying envelope approximation [8] and get the paraxial wave equation

$$2i k \frac{\partial}{\partial z} A(r, z) + \nabla_{\text{T}}^2 A(r, z) = -\frac{\omega^2}{\epsilon_0 c_0^2} p_{\text{NL}}(r, z) \exp[i \Delta k z], \quad (1.4)$$

with the Laplace operator  $\nabla_{\text{T}}^2$ , expressed in polar coordinates and the polarization, induced by the nonlinear interaction of the fundamental field with the molecules.  $\Delta k = k' - k$  is the wave vector mismatch of the wave vectors of the harmonic and fundamental electric fields. We now consider the special case of THG, where the amplitude of the polarization is  $p_{\text{NL}}(r, z) = \epsilon_0 \chi^{(3)} A_1^3(r, z)$ , with the amplitude of the fundamental wave  $A_1(r, z)$ . We solve the paraxial wave equation by an ansatz of focused Gaussian beams (compare [26])

$$A_q(r, z) = \frac{\tilde{A}_q(z)}{1 + 2i z/b} \exp\left[-\frac{q r^2}{w_0^2(1 + 2i z/b)}\right], \quad (1.5)$$

with  $q = 1$  for the fundamental amplitude and  $q = 3$  for the harmonic amplitude and the confocal parameter  $b = 2\pi w_0^2/\lambda$  ( $w_0$ : minimal  $1/e^2$  radius of the Gaussian beam,  $\lambda$ : fundamental wavelength). Inserting this ansatz into Eqn. (1.4) yields

$$\frac{d\tilde{A}_3}{dz}(z) = i \frac{3\omega}{2n_3 c_0} \chi^{(3)} \tilde{A}_1^3(z) \frac{\exp[i \Delta k z]}{(1 + 2i z/b)^2}, \quad (1.6)$$

with the refractive index of the harmonic wave  $n_3$ . The power of the third harmonic field is  $P_3(z) = \pi n_3 \epsilon_0 c_0 w_0^2 |\tilde{A}_3(z)|^2$ . We obtain the amplitude of the electric field of the third harmonic by integration of Eqn. (1.6) over  $z$ . The integral over the complex denominator in Eqn. (1.6) is the phasematching integral

$$J_3 = \frac{2}{b} \int_0^L \frac{\exp[-i \Delta k z']}{(1 + 2i(z' - z_0)/b)^2} dz', \quad (1.7)$$

which we will discuss below. We apply the approximation  $n_3 \approx 1$  which is valid, as the refractive index of thin molecular gases is typically  $(n_3 - 1) \ll 10^{-4}$ , and include losses due to reabsorption of the third harmonic by Beer's law with the absorption coefficient  $\alpha_3$  and the sample length  $L$ . With these steps we arrive at the result from

Kildal and Deutsch [15]

$$P_3 = \frac{3\mu_0^2 \omega^2}{4\lambda^2} |\chi^{(3)}|^2 |J_3|^2 P_1^3 \exp[-\alpha_3 L], \quad (1.8)$$

with the wavelength of the fundamental radiation  $\lambda$  and the magnetic permeability of free space  $\mu_0$ . Hence, the power of the third harmonic mainly depends on

$$P_3 \sim |\chi^{(3)}|^2 |J_3|^2 P_1^3. \quad (1.9)$$

Therefore, we can increase the THG yield by increasing the nonlinear susceptibility  $\chi^{(3)}$ , fulfill phase matching conditions in  $|J_3|^2$  or increase the fundamental peak intensity. The particle density enters the equation via the nonlinear susceptibility, yielding a quadratic dependence of the THG power upon the gas pressure (provided the pressure is sufficiently low to neglect phase mismatch). We discuss resonance enhancement of the nonlinear susceptibility and the influence of phase matching upon the THG process in the following sections.

## 1.2 Nonlinear susceptibility and resonance enhancement

The nonlinear susceptibility  $\chi^{(3)}$  includes the energetic structure, transition probabilities and external influences, e.g., the pressure and temperature dependence of the linewidth. These features strongly depend on the fundamental wavelength and distinguish different molecules and, hence, allow the identification of molecules based on measurements of the spectral dependence of  $\chi^{(3)}$ . Higher orders of the nonlinear susceptibility would also allow molecule detection, albeit with significantly lower signal yields. We consider resonance enhancement in the electronic ground state of HCl with rovibrational states as intermediate states. In the degenerate case of THG we consider a single incident field with frequency  $\omega$ . We can neglect all other contributions to  $\chi^{(3)}$  in the four-level system, due to large detunings. Fig. 1.1 shows the three possible level schemes for resonantly enhanced THG in a molecule (for more details on the states in our sample molecule HCl see Sec. 2.2). For simplicity we introduced the detunings  $\Delta_{1p} = \omega_{ba} - \omega$  to the one-photon resonance with the state  $\nu = 1$ , the two-photon detuning  $\Delta_{2p} = \omega_{ca} - 2\omega$  with the state  $\nu = 2$  and the three-photon detuning  $\Delta_{3p} = \omega_{da} - 3\omega$  with the state  $\nu = 3$ . From the level schemes it is evident, that  $\chi^{(3)}$  increases, if the first, second or third photon of the fundamental field is resonant to molecular states.

We determine the nonlinear susceptibility with the assumption, that the initial population is located solely in the vibrational ground state with  $\nu = 0$ , which is parameterised by the rotational ground state  $|a\rangle$ . Further intermediate states are  $(\nu = 1, b)$ ,  $(\nu = 2, c)$  and the state  $(\nu = 3, d)$  (compare Sec. 2.2) with the term energies  $E_a < E_b < E_c < E_d$ . The nonlinear susceptibility for THG with frequency  $\omega$  then is [27]

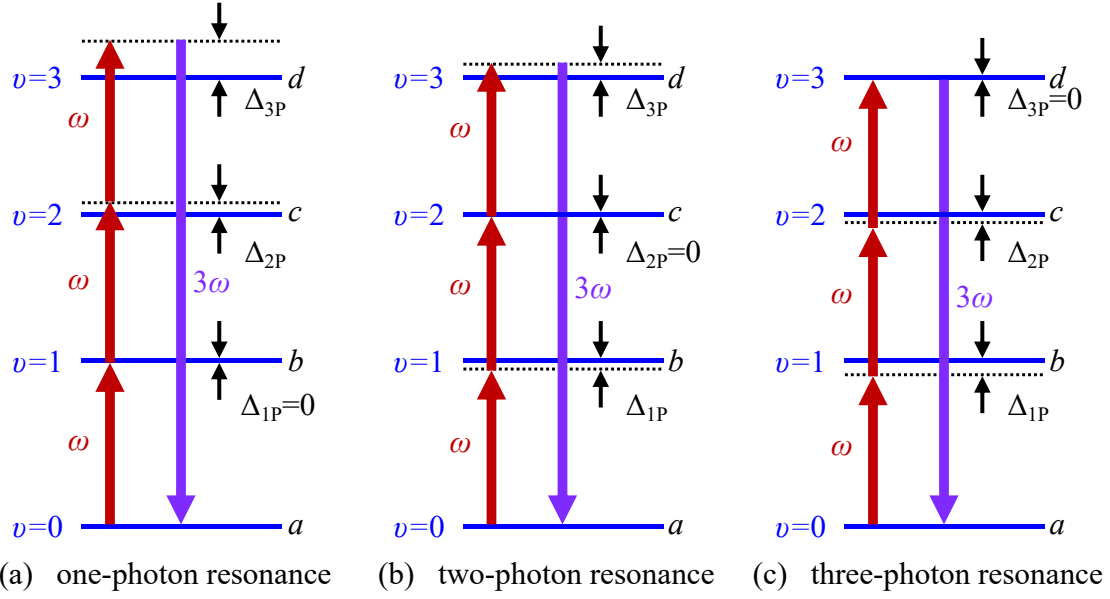


**Figure 1.1:** Resonant THG coupling schemes with states  $a, b, c$  and  $d$ , parameterized by the vibrational quantum number  $v$  in the electronic ground state. Note, that we omit rotational substructure in the plots.

$$\chi^{(3)}(\omega) \propto \frac{1}{\epsilon_0 \hbar^3} \sum_{a,b,c,d} \rho_a \mu_{ba} \mu_{cb} \mu_{dc} \mu_{da} \left[ \begin{aligned} & \frac{1}{(\omega_{da} - 3\omega - i\gamma_{da})(\omega_{ca} - 2\omega - i\gamma_{ca})(\omega_{ba} - \omega - i\gamma_{ba})} \\ & + \frac{1}{(\omega_{da} + \omega + i\gamma_{da})(\omega_{ca} - 2\omega - i\gamma_{ca})(\omega_{ba} - \omega - i\gamma_{ba})} \\ & + \frac{1}{(\omega_{da} + \omega + i\gamma_{da})(\omega_{ca} + 2\omega + i\gamma_{ca})(\omega_{ba} - \omega - i\gamma_{ba})} \\ & + \frac{1}{(\omega_{da} + \omega + i\gamma_{da})(\omega_{ca} + 2\omega + i\gamma_{ca})(\omega_{ba} + 3\omega + i\gamma_{ba})} \end{aligned} \right], \quad (1.10)$$

with the number density of molecules  $\rho_a$  in the ground state, which includes the population of the rotational ground state, isotopic abundance and information of pressure and temperature according to the ideal gas equation. The parameters  $\mu_{ij}$  are the transition dipole moments for the transitions with frequency  $\omega_{ij}$  between two states  $|i\rangle$  and  $|j\rangle$ . The dephasing rates  $\gamma_{ij}$  describe the linewidth of the corresponding resonances due to decay rates and collisional broadening (see Sec. 3.4.1). The first resonance term in Eqn. 1.10 describes the situation of Fig. 1.1. Here, the photon energies add to the energy of the ground state  $E_a$  and the THG has a frequency according to the energy difference  $E_d - E_a$ . The other resonance terms describe further combinations, which are relevant for the nonresonant contribution of  $\chi^{(3)}$ .

The ladder-type level scheme of a molecule (compare Fig. 1.1) increases the computational complexity for the calculation of  $\chi^{(3)}$ . For each ground state, we have

to consider detunings to all four-level systems, which are allowed by selection rules for rovibrational transitions (compare Sec. 2.2). For more details on the numerical implementation see [28].

We can separate Eqn. (1.10) in a resonant  $\chi_{\text{res}}^{(3)}$  and a nonresonant part  $\chi_{\text{nr}}^{(3)}$ . Consider for example resonance enhancement of the nonlinear susceptibility by tuning the fundamental frequency to a two-photon resonance  $\Delta_{2\text{p}} \approx 0$ . Note, that the discussion of one- and three-photon resonance is analogous. We assume, that the detunings to the other states  $\nu = 1$  and  $\nu = 3$  are larger than the corresponding dephasing rates. Hence, Eqn. (1.10) simplifies to

$$\chi^{(3)}(\omega) \approx \chi_{\text{nr}}^{(3)} + \frac{\rho_a}{\epsilon_0 \hbar^3} \frac{1}{\Delta_{2\text{p}} - i\gamma_{ca}} \sum_{b,d} \frac{\mu_{ba} \mu_{cb} \mu_{dc} \mu_{da}}{(\Delta_{3\text{p}} - i\gamma_{da})(\Delta_{1\text{p}} - i\gamma_{ba})}. \quad (1.11)$$

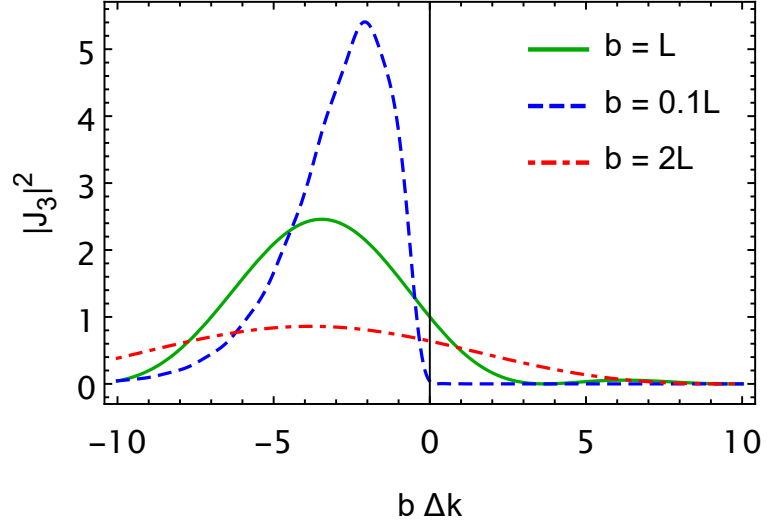
Note, that even though we have selected a ground state  $|a\rangle$  and a resonant state  $|c\rangle$ , we have to sum over all possible intermediate states  $|b\rangle$  and  $|d\rangle$ . On two-photon resonance,  $\Delta_{2\text{p}} = \omega_{ca} - 2\omega$  vanishes and  $\chi^{(3)}$  is an imaginary quantity and proportional to  $\gamma_{ca}^{-1}$ . In thin molecular gases the dephasing rate  $\gamma_{ca}$ , i.e., the linewidth of the two-photon resonance, is in the range of GHz, mainly due to Doppler broadening and collisional self-broadening (see Sec. 3.4.1). Hence, on two-photon resonance  $\chi^{(3)}$  is significantly increased, as typically  $\gamma_{ca} \ll \Delta_{1\text{p}}, \Delta_{2\text{p}}$  and  $\Delta_{3\text{p}}$ . The laser linewidth of the fundamental radiation is in the order of 0.1 GHz. Therefore,  $\gamma_{ca}$  limits the gain by resonance enhancement in our case. We roughly estimate the resonance enhancement by comparing the resonant  $\chi^{(3)}$  with an off-resonant value for  $\chi^{(3)}$ , i.e., far from resonances, where we can neglect the dephasing rates in Eqn. (1.11). Consider for example Eqn. (1.11) with a two-photon detuning of  $\Delta_{2\text{p}} = 300$  GHz (or  $10 \text{ cm}^{-1}$  when expressed in wave numbers). Here, we get an enhancement factor of  $\Delta_{2\text{p}}/\gamma_{ca} \approx 300$ . The nonlinear susceptibility enters the generated THG power in Eqn. (1.8) quadratically, hence, we expect significant resonance enhancement factors of  $10^4 - 10^5$ .

### 1.3 Phasematching considerations

The phase matching integral, given by Eqn. (1.7), describes the influence of wave vector mismatch and focus geometry upon the power of the third harmonic field. For this quantity, we have to explicitly calculate the wave vector mismatch, and, hence, the refractive index of HCl, which in turn depends on the linear susceptibility via  $n = \sqrt{1 + \chi^{(1)}}$ .

We can calculate the linear susceptibility of a molecule by adaption of the quantum mechanical description of a free atom, which interacts with an external field. In the perturbative regime, i.e., at peak intensities  $< 10 \text{ TW/cm}^2$  [29], we can calculate the averaged induced electric dipole moment  $\langle \mu \rangle$  from a density matrix approach [8]. Hence, we can derive the linear susceptibility from the equation for the linear polarisation:  $P = \rho \langle \mu \rangle = \epsilon_0 \chi^{(1)} E$ , with the molecular number density  $\rho$  [8]. The linear susceptibility then is

**Figure 1.2:** Absolute square value of the phasematching integral vs. the dimensionless parameter  $b\Delta k$ , i.e., phase mismatch. The green line indicates confocal focusing, i.e.,  $b = L$ , the dashed blue line shows tight focusing with  $b = 0.1L$  and the red dot-dashed line gives an example for loose focusing ( $b = 2L$ ). For this calculation, we assumed, that the focus is in the center of the cell, i.e.,  $z_0 = 0.5L$ .



$$\chi^{(1)}(\omega) = \frac{1}{3\epsilon_0 \hbar} \sum_{a,b} \rho_a |\mu_{ba}|^2 \left[ \frac{1}{\omega_{ab} - \omega - i\gamma_{ab}} + \frac{1}{\omega_{ab} + \omega + i\gamma_{ab}} \right], \quad (1.12)$$

with transition frequencies  $\omega_{ab}$ , dephasing rates  $\gamma_{ab}$  and transition dipole moments  $|\mu_{ab}|$  for transitions between the states  $\nu = 0 \rightarrow 1$  for the fundamental and  $\nu = 0 \rightarrow 3$  for the third harmonic radiation. The factor  $1/3$  originates from symmetry considerations in an isotropic medium [8]. We discuss the refractive index of our sample gas HCl in appendix A.

With the refractive index at the fundamental and harmonic wavelength we calculate the wave vector mismatch  $\Delta k = k(\lambda/3) - 3k(\lambda)$ , with the wave vector  $k(\lambda, p, T) = 2\pi/\lambda n(\lambda, p, T)$ . Note, that there is no uniform sign convention for the wave vector mismatch, hence, we follow the definition of Bjorklund [25] and get

$$\Delta k(\lambda, p, T) = \frac{6\pi}{\lambda} [n(\lambda/3, p, T) - n(\lambda, p, T)]. \quad (1.13)$$

Note, that the refractive index is a complex quantity. Hence, the wave vector is complex, too. However, we find, that the imaginary part of  $k$  is  $\text{Im}[k] = \alpha/2$  with the linear absorption coefficient  $\alpha$ . Therefore, the phasematching integral incorporates Beer's absorption law with the (real) integral over the exponent  $\exp[-(\alpha_3 - 3\alpha_1)z']$  with the absorption coefficients of the harmonic and fundamental wave and the integration coordinate  $z'$ . Hence, absorption of the harmonic and fundamental wave will reduce the THG yield.

Typically, the literature discusses the phasematching integral  $J_3$  in two limits: Tight focusing, where the confocal parameter is much smaller than the length of the interaction region:  $b \ll L$ . Here, the Gouy phase shift of  $\pi$ , which the radiation accumulates by propagation through the focus, limits the THG process to negative wave vector mismatch  $\Delta k < 0$  ( $|J_3|^2 = 0$  for  $\Delta k \geq 0$ ) [12]. In the other limit, the confocal parameter is larger than the length of the medium  $b \gg L$ , i.e., loose focusing. An example is the approximation of plane waves and a sample with finite length. In this case  $|J_3|^2$  integrates analytically to a  $\text{sinc}^2$  function, which is symmetrical

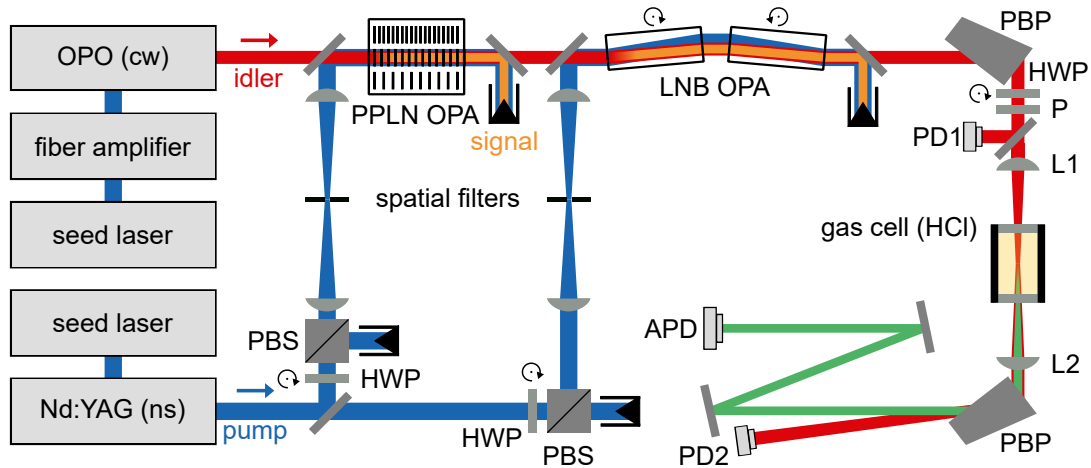
with regard to  $\Delta k = 0$ , albeit at considerably lower absolute values for  $|J_3|^2$ . In the experiment we consider intermediate, or confocal focusing, i.e.,  $b \approx L$ . Here, we cannot find an analytical solution for Eqn. (1.7). Hence, we solve the integral numerically.

Fig. 1.2 shows a comparison of different focusing conditions. In the tight focusing case,  $|J_3|^2$  is zero for zero or positive phase mismatches. But the peak value is the largest result at  $b\Delta k \approx -2$ . Hence, we would benefit from choosing the phase mismatch to match this value. This process is called phase matching. For example, in a sample gas with anomalous dispersion for THG, the correct choice of the pressure yields perfect phase matching. On the other hand it is possible to add a buffer gas with anomalous dispersion for THG, to reach phase matching [25].

## Chapter 2

### Experimental setup

The experiments require a tunable mid-infrared laser system with narrow spectral bandwidth (i.e., in the range of the Doppler broadening for molecular gases at room temperature) and pulse energies in the mJ regime (i.e., to drive frequency conversion, even at low gas pressures). Towards this goal, we designed and constructed a laser system, which provides tunable, mid-infrared, nanosecond (ns) laser pulses. Short pulses with durations in the range of some nanoseconds prove to be a good compromise of a bandwidth slightly lower than the Doppler broadening bandwidth and reasonably high peak intensity in the range of  $100 \text{ MW/cm}^2$ , i.e., sufficient intensities to observe nonlinear response of third order from thin molecular gases. We give an overview of the experimental setup in Fig. 2.1. For proof of principle investigations in HCl we choose a gas cell geometry. We discuss the individual components of the experimental setup in the following chapter.



**Figure 2.1:** Experimental setup, with optical parametric oscillator (OPO), optical parametric amplifiers (OPA), periodically poled Lithium Niobate crystal (PPLN), bulk Lithium Niobate crystals (LNB), Pellin Broca prisms (PBP), photovoltaic detectors (PD), InGaAs avalanche photodiode (APD), thin film polarizer (TFP), half wave plates (HWP), mid-infrared Rutile polarizer (P) and polarizing beamsplitter cubes (PBS).

### 2.1 Laser system

The laser setup involves a commercial continuous wave (cw) optical parametric oscillator (OPO, Argos Model 2400-C, Aculight/Lockheed Martin), which provides an idler wave with tunability in the spectral interval of  $3.2 - 3.9 \mu\text{m}$ , at a spectral bandwidth with a full-width at half-maximum  $< 1 \text{ MHz}$  (FWHM, single longitudinal

mode) and output power beyond 1 W. The OPO serves as a seed source for home-made pulsed optical parametric amplifier (OPA) stages.

A distributed feedback fiber amplifier (YAR-15K-1064-LP-SF) with an internal single longitudinal fiber seed laser (Koheras, NKT Photonics) delivers (cw) pump radiation at 1064 nm for the OPO. Due to a defect we had to replace the fiber seed laser with an external fiber-coupled seed laser (Koheras Adjustik Y10, NKT Photonics). The gain medium is a periodically poled Lithium Niobate (PPLN) crystal with poling periods in "fan-out" configuration. This configuration permits us to fulfill the quasi-phase-matching condition for different wavelengths by shifting the crystal and, hence, select a region with appropriate poling period (see Fig. 2.2). According to this condition the pump radiation divides in a long wavelength idler radiation with  $3.2 - 3.9 \mu\text{m}$  and a short wavelength signal radiation with  $1.46 - 1.60 \mu\text{m}$ .

We use a temperature controlled oven to set the crystal to a constant temperature. We extended the commercial OPO with a translation stage for the PPLN crystal (for details see [30, 31]). The cavity is singly-resonant to the signal wave and an uncoated intracavity etalon with a free spectral range of 400 GHz selects a single longitudinal mode.

We accomplish continuous tunability of the OPO output idler wave by alignment in three steps from coarse to fine adjustment: With the crystal position we change the signal wavelength in discrete steps of 400 GHz, given by the free spectral range of the etalon. With adjustment of the etalon angle we change the signal wavelength in discrete steps of  $\approx 30$  GHz. The discretization is due to "OPO inertia", according to the manufacturer [30]. Finally, we tune the OPO output idler wave by tuning the pump laser frequency, while the signal wave remains constant. The fiber seed laser allows two ways of wavelength tuning: Fast tuning of 10 GHz by piezoelectric strain and slow tuning of 200 GHz by temperature tuning of the fiber seed laser. Hence, the OPO delivers mode-hop free tunability of the output idler wavelength on the spectral range of  $3.2 - 3.9 \mu\text{m}$  (for details see [31]).

We apply a Fizeau-based wavemeter (WS6-600, High Finesse, measurement resolution of 20 MHz) to measure the central wavelength of the fiber seed laser. We measure the signal wavelength with an optical spectrum analyser (OSA, AQ-6315A, Ando) with a fraction of the signal output sampled with a pick-off window, coupled to a single mode fiber. This permits determination of the idler wavelength with an accuracy of 6.5 GHz (given by the frequency resolution of the OSA). This is sufficient to monitor potential jumps between longitudinal modes of the OPO cavity, which are separated by 30 GHz. However, this coarse measurement does not yet permit precise calibration of the idler wavelength for molecular transitions in HCl. Usually, for detunings smaller than 10 GHz, the idler wavelength only depends on the wave-

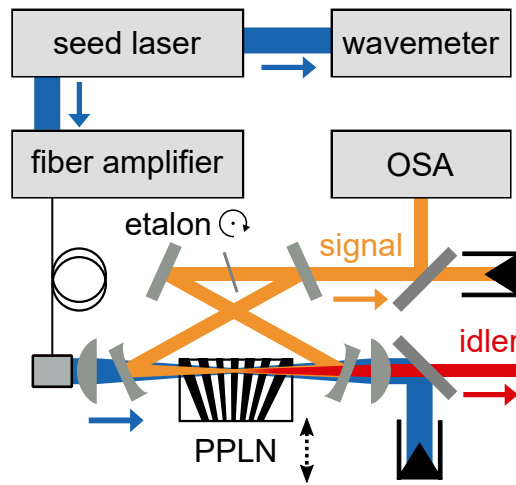


**Figure 2.2:** Schematic view of the (cw) OPO and wavelength diagnostics, including an optical spectrum analyser (OSA).

length of the pump radiation (which we measure with the wavemeter). This is due to the intracavity etalon, which fixes the signal wavelength of the OPO. For precise calibration of the idler wavelength, we measure the transmission spectrum in HCl (see Fig. 2.11) and determine the wavelength offset to the vacuum wavelengths of absorption lines in HCl (HITRAN2016 [32]).

### 2.1.1 Preamplifier OPA stage

The aforementioned OPO serves as a seed source for a home-built three-stage OPA system pumped by a (ns) Nd:YAG laser. In this work we use two different pump lasers: Firstly, a compact, free-running Nd:YAG laser (Brilliant, Quantel) with a repetition rate of 10 Hz, a mean pulse duration of 4.4(2) ns (FWHM), and a bandwidth of  $\approx 1 \text{ cm}^{-1}$  (FWHM). Secondly, an injection seeded Nd:YAG laser (Pro Lab 230, Spectra Physics, equipped with ROCK fiber laser seeder, NP Photonics) with a repetition rate of 20 Hz, pulse duration 8.0(1) ns (FWHM), and nearly Fourier transform-limited bandwidth  $< 0.003 \text{ cm}^{-1}$ . We measured the pulse durations with a photo detector (PD, UPD-200-UD, Alphas, rise time:  $< 175 \text{ ps}$ , bandwidth:  $> 2 \text{ GHz}$ ), sampled by a digital oscilloscope (WaveRunner 104Xi, Le Croy) with a bandwidth of 1 GHz. To reduce variations in the intensity profile of the (ns) pump radiation we use a spatial filter, which provides a Gaussian beam profile. We determine the beam quality factor  $M^2$  for the spatially filtered (ns) pump radiation from measurements with a home-built camera-based beam profiler (daA1280-54um, Basler) to 1.3 in the horizontal and 1.6 in the vertical axis (according to ISO-norm 11146, [33]).

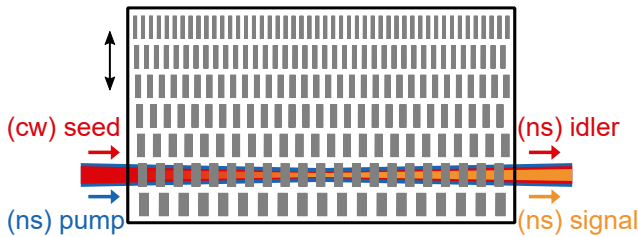


**Figure 2.3:** Side view on the PPLN crystal with 7 different poling periods (length  $\times$  height  $\times$  width =  $50 \times 12 \times 1 \text{ mm}^3$ ). We use the poling period with  $29.8 \mu\text{m}$ . Both facets have anti reflection coatings.

2.3). Combined with a PID-regulated temperature control unit (HC Photonics), this permits quasi-phase-matching in a spectral range of  $3.2 - 4.6 \mu\text{m}$ . All experiments in this work use the poling period with  $29.8 \mu\text{m}$ , which allows quasi-phase-matching in the spectral range  $3.44 - 3.71 \mu\text{m}$ .

As we mix the (ns) pump pulses with a (cw) seed there are no timing issues. However, we can employ a chopper which operates on the repetition rate of the pump laser to reduce the average power of the focused mid-infrared (cw) seed radiation, which may damage the optical elements of the experimental setup. We operate the OPA with collimated (ns) pump radiation and focus the (cw) seed radiation with a confocal parameter of  $\approx 10 \text{ cm}$  into the crystal (compare [34]). We measure the beam profile of the (cw) seed radiation with a home-built, single-detector, moving-aperture

In the first (preamplifier) OPA stage we apply a Magnesium oxide (MgO) doped PPLN crystal (HC Photonics, compare Fig. 2.3). PPLN is well suited for a single pass preamplifier due to its high effective nonlinear susceptibility and the missing Poynting vector walk-off, as all fields have the same polarization. The PPLN crystal contains several separated sections with different poling periods  $27.17 - 30.45 \mu\text{m}$  (compare Fig.

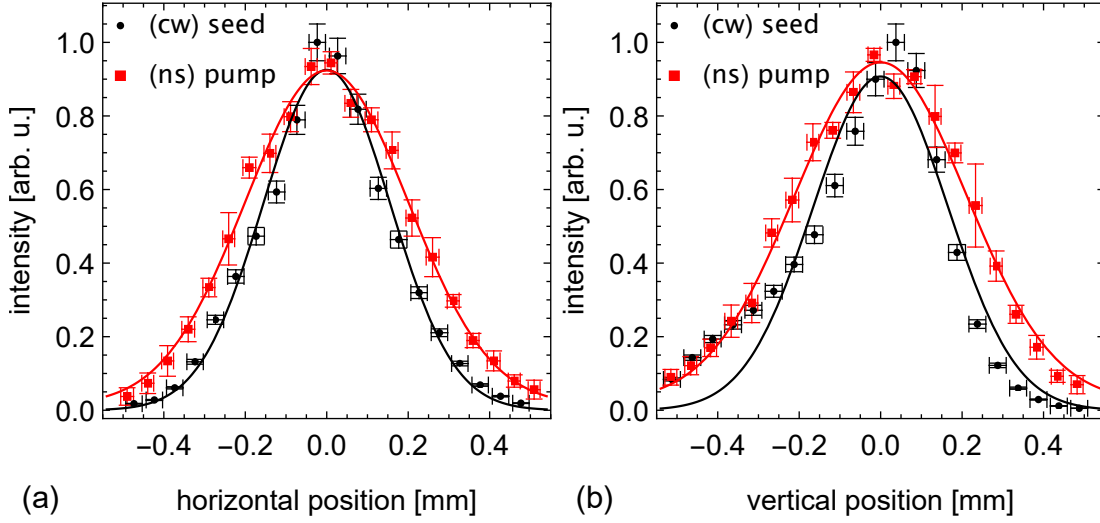


**Figure 2.4:** Beam profiles (intensity vs. spatial position) of the (cw) idler seed beam and the (ns) pump beam in the PPLN OPA stage (thickness: 1 mm). Cuts in horizontal and vertical direction. Solid lines indicate Gaussian fits to the experimental data with  $1/e^2$  widths of the (cw) seed: horizontal:  $620\ \mu\text{m}$ , vertical:  $670\ \mu\text{m}$ , and the (ns) pump: horizontal  $1/e^2$  width of  $800\ \mu\text{m}$ , vertical:  $850\ \mu\text{m}$ .

beam profiler ( $50\ \mu\text{m}$ -diameter aperture, detector: P13243-011MA, Hamamatsu). Fig. 2.4 shows the overlap of the (ns) pump radiation and the (cw) seed radiation in position of the entry facet of the crystal. We notice a structure on the left side of the (cw) beam profile in Fig. 2.4 (b). This is due to diffraction, probably in the OPO cavity.

As a disadvantage of the Gaussian beam profile of the (ns) pump radiation, we get a Gaussian-shaped gain profile, which leads to gain guiding [35]. Due to the high gain in the center of the transverse profile we observe strong narrowing of the transverse idler and signal profiles. This limits the conversion efficiency and leads to low beam quality of the amplified idler pulses. We note, that PPLN is susceptible to self focusing [36] and photorefractive degradation [37]. To prevent such processes, the LNB material is doped with 5% MgO [38]. Nevertheless, we notice photorefractive degradation, e.g., by beam profile distortion of the depleted pump radiation or loss of conversion efficiency. These processes occur predominantly at crystal temperatures lower than  $130\ ^\circ\text{C}$ . This is due to local changes of the refractive index at high pump intensities (for details see [34]). In our case, most changes due to photorefractive degradation are reversible by heating the crystal to  $200\ ^\circ\text{C}$  for more than one hour.

To evaluate the performance of the preamplifier OPA stage we measure the dependence of the idler pulse energy versus (ns) pump pulse energy and (cw) seed power. In the case of an undepleted pump field the small signal gain is  $G = 1/4 \exp[2\Gamma L]$ , with crystal length  $L$  and  $\Gamma \propto \sqrt{|d_{\text{eff}}|^2 I_p}$ , where  $d_{\text{eff}}$  is the effective nonlinear susceptibility and  $I_p$  the pump intensity [39]. In Fig. 2.5 (a) the idler pulse energy follows the expectation up to a pump pulse energy of  $\approx 200\ \mu\text{J}$ . For higher pump pulse energies the idler pulse energy saturates. We reach idler pulse energies of  $\approx 35\ \mu\text{J}$  with a pump pulse energy of  $600\ \mu\text{J}$ . This behaviour is caused by depletion of the pump field (for details see [34]). Due to energy conservation this idler pulse energy corresponds

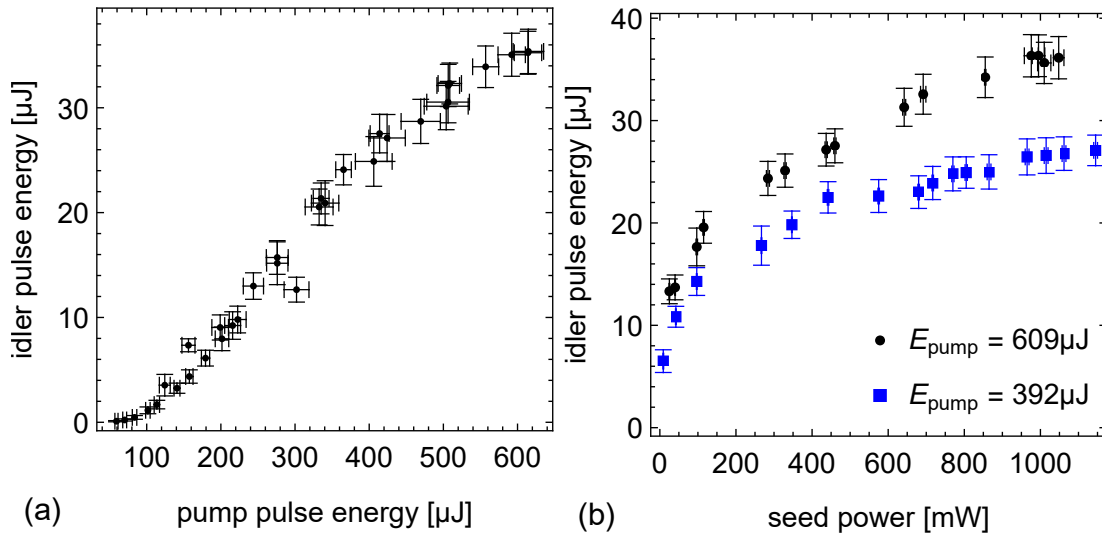


**Figure 2.5:** Output idler pulse energy (a) vs. pump pulse energy with a (cw) seed power of 915 mW or (b) vs. (cw) seed power at fixed pump pulse energies, stated in the plot legend. Error bars indicate standard deviations.

to a signal pulse energy of  $82 \mu\text{J}$  with the factor of 2.35 being the fraction of the wavelengths:  $\lambda_{\text{idler}}/\lambda_{\text{signal}}$ , with  $\lambda_{\text{idler}} = 3565 \text{ nm}$  and  $\lambda_{\text{signal}} = 1516.6 \text{ nm}$ . Therefore, the OPA has a conversion efficiency of  $\approx 20 \%$ . This is already a considerable value, in particular, when we consider the imperfect spatial overlap of the pump and seed radiation in the crystal [35].

The idler pulse energy also depends on the (cw) seed power. For an undepleted pump field we expect a linear dependence, as the small signal gain only depends on the pump pulse energy. In Fig. 2.5 (b) we observe saturation of the idler pulse energy above  $\approx 200 \text{ mW}$ , which corresponds to a pulse energy of  $0.9 \text{ nJ}$ .

## 2.1.2 Power OPA stage

As indicated above, the first OPA stage with the PPLN crystal yields an output idler pulse energy in the range of a few  $10 \mu\text{J}$ . This is due to the damage threshold of PPLN with regard to the driving pump pulse energy (roughly  $0.6 \text{ mJ}$  in our case). To proceed towards larger pulse energy, we add a power OPA stage with two bulk LNB crystals (doped with 5% MgO, length  $\times$  height  $\times$  width =  $30 \times 8 \times 8 \text{ mm}^3$ ,  $\theta \approx 45^\circ$ ,  $\phi = 30^\circ$ , supplied by Castech), employing angle tuning to provide phase matching.

One major drawback of critical phasematching, when compared to quasi-phase-matching is the occurrence of a Poynting vector walk-off. In our case the pump-beam has a walk-off angle of  $\approx 2.1^\circ$  with regard to the idler- and signal-beam. To prevent the problem, we arrange the two LNB crystals in a geometry of walk-off compensation (see Fig. 2.1) and choose a slightly larger Gaussian beam profile for the seed radiation. The length of the two crystals is limited by the individual Poynting vector walk-off, back conversion, as well as the acceptance bandwidth of the mixing process. The latter scales linearly with the crystal length. With a length of  $3 \text{ cm}$ , the acceptance bandwidth is  $\approx 6 \text{ cm}^{-1}$  (or  $180 \text{ GHz}$ ), i.e., no limitation for nanosecond pulses with

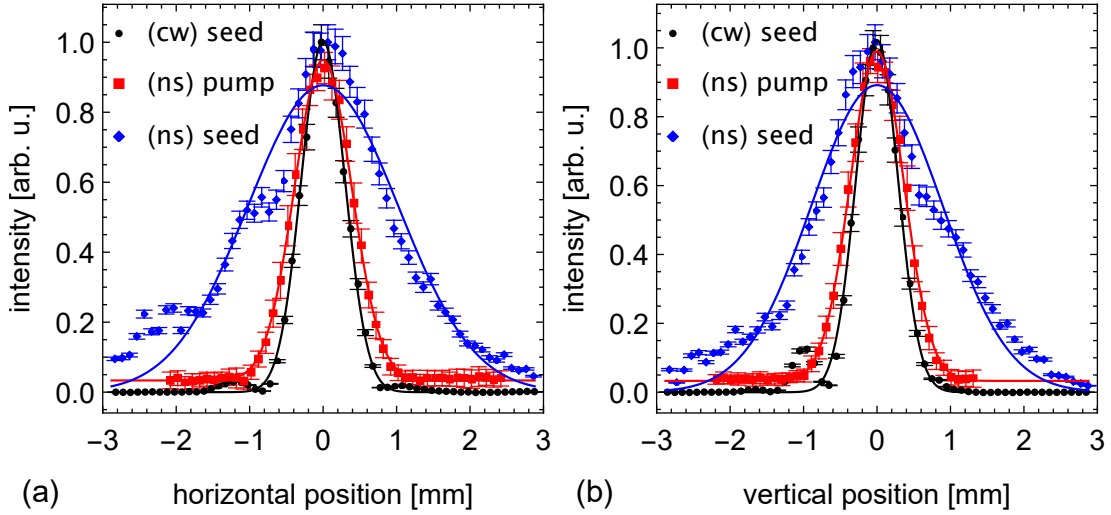


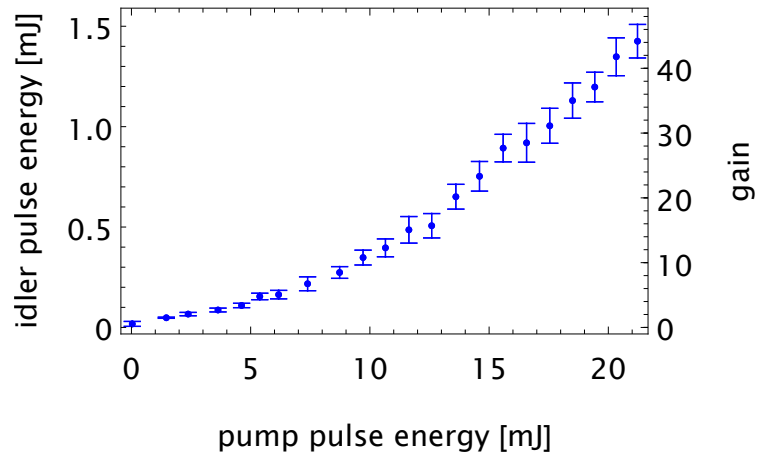
**Figure 2.6:** Beam profiles (intensity vs. spatial position) of the (cw) idler beam, (ns) seed beam and the (ns) pump beam in the power OPA stage. Cuts in (a) horizontal and (b) vertical direction. Solid lines indicate Gaussian fits to the experimental data with  $1/e^2$  width of: (ns) seed: horizontal: 4.1 mm, vertical: 3.6 mm; (cw) seed horizontal  $1/e^2$  width: 1.2 mm, vertical: 1.2 mm; (ns) pump: horizontal  $1/e^2$  width of 1.6 mm, vertical: 1.5 mm.

bandwidths in the range of  $< 100$  MHz. To prevent back conversion we block the signal output of the preamplifier OPA stage with a long-pass filter (#68653, Edmund Optics).

For an optimal conversion efficiency in the OPA, seed and pump profile should be approximately the same size. To precompensate gain guiding or Poynting vector walk-off it might even be beneficial to choose a larger pump profile. Fig. 2.6 compares the spatial beam profiles at the entrance of the power OPA stage. The beam profile of the (ns) seed radiation is much larger than the beam profile of residual (cw) seed radiation and shows some deviations in comparison with the Gaussian fit. This is due to the photorefractive effect and self focusing in the preamplifier OPA stage. The beam profile of the (ns) pump radiation is smaller than the beam profile of the (ns) seed radiation. We could not perfectly optimize the beam profile of the mid-infrared (ns) seed radiation, as an additional telescope introduced reflection losses upon the seed pulse energy (due to uncoated  $\text{CaF}_2$  optics) and was difficult to align. We could not further enlarge the beam profile for the pump radiation either, as the damage threshold of the high-power pinhole of the spatial filter limited the pump pulse energy. Moreover, the pump pulse energy is limited by the damage threshold of the beam combiner for idler and pump radiation (experimentally measured to be close to a fluence of  $2.8 \text{ J/cm}^2$ , corresponding to a pulse energy of  $\approx 25$  mJ in our setup, 1064 nm, 8 ns and 20 Hz).

Fig. 2.7 gives the idler pulse energy obtained from the power OPA stage vs. pump pulse energy. The gain of the power OPA stage exceeds 40. The conversion efficiency of the LNB OPA is  $\approx 21\%$ , which is comparable to the preamplifier OPA stage. We notice some distortions in the beam profile of the residual pump radiation behind the two crystals that indicate saturation or back conversion into the pump field. Nevertheless, the beam profile of the mid-infrared idler radiation remains unaffected.

**Figure 2.7:** Output idler pulse energy vs. pump pulse energy for the power OPA stage. The seed pulse energy from the preamplifier OPA stage was  $32\ \mu\text{J}$  at an idler wavelength of  $3534\ \text{nm}$ . The right axis gives the single-pass gain for the idler pulse energy in the power OPA stage. Error bars indicate standard deviations.



We separate the idler radiation from residual pump radiation by a dichroic mirror (L-06774, Laseroptik) and from the signal radiation by a  $\text{CaF}_2$  Pellin Broca prism (ADBV-10, Thorlabs). With the prism we also remove radiation from parasitic processes in the OPA chain (e.g., phase-mismatched second harmonic generation of the pump- and signal wave). For the experiments, we always operate the power OPA stage at a maximal pump pulse energy of  $22\ \text{mJ}$  and attenuate the obtained idler pulse energy, if required, afterwards. The variable attenuator consists of a low-order half-waveplate, coated for a central wavelength of  $3.5\ \mu\text{m}$  (WPLH05M-3500, Thorlabs), and a Rutile polarizer for the wavelength range of  $2.2 - 4\ \mu\text{m}$  (GTR8-MIR, Thorlabs).

Tuning of the central wavelength of the idler pulses in the range of  $200\ \text{GHz}$  is straightforward. The OPO defines the wavelength of the (cw) seed radiation (compare Sec. 2.1). The preamplifier OPA stage has a quasi-phase-matching bandwidth of  $\approx 600\ \text{GHz}$  (FWHM) at  $3.56\ \mu\text{m}$  [34]. The LNB crystals of the power OPA stage have a phase matching bandwidth of  $\approx 170\ \text{GHz}$  (FWHM) at  $3.56\ \mu\text{m}$ . Hence, fine tuning of the idler wavelength of the seed OPO in the range of  $< 100\ \text{GHz}$  does usually not require variation of the phase matching conditions in the OPA stages.

We observe a strong dependence of the gain of the power OPA stage upon changing the non-phaseshifting angle  $\phi$ . This is due to interference effects in the LNB crystals with their parallel surfaces - which act like an etalon for the signal radiation, as the reflectivity of the coating for the latter is still around  $8\%$ . Fig. 2.8 (a) illustrates the effect, when we measure the idler output pulse energy of the power OPA stage over a frequency tuning range of  $\approx 220\ \text{GHz}$ . We observe a strong periodic oscillation with an amplitude of up to  $30\%$  of the mean value  $1.0\ \text{mJ}$ . The oscillation period is  $\Delta\tilde{\nu} = 0.072\ \text{cm}^{-1}$ . This corresponds to an etalon with a thickness of  $\approx 32\ \text{mm}$  at an index of refraction  $2.209$  at wavelength  $1522\ \text{nm}$ , i.e., the signal wavelength. This fits with the length  $L = 30\ \text{mm}$  of the LNB crystals. Fig. 2.8 (b) shows how the modulation on the idler pulse energy effects the THG experiment, i.e., the observation of a spectral line. In the detected frequency interval, we expect spectral lines at the fundamental wave numbers  $2830.15$  and  $2830.36\ \text{cm}^{-1}$  (we will discuss the corresponding resonances in more detail in Sec. 3.1). For the red data points we tried to rescale the THG signal pulse energy based upon the intensity dependence

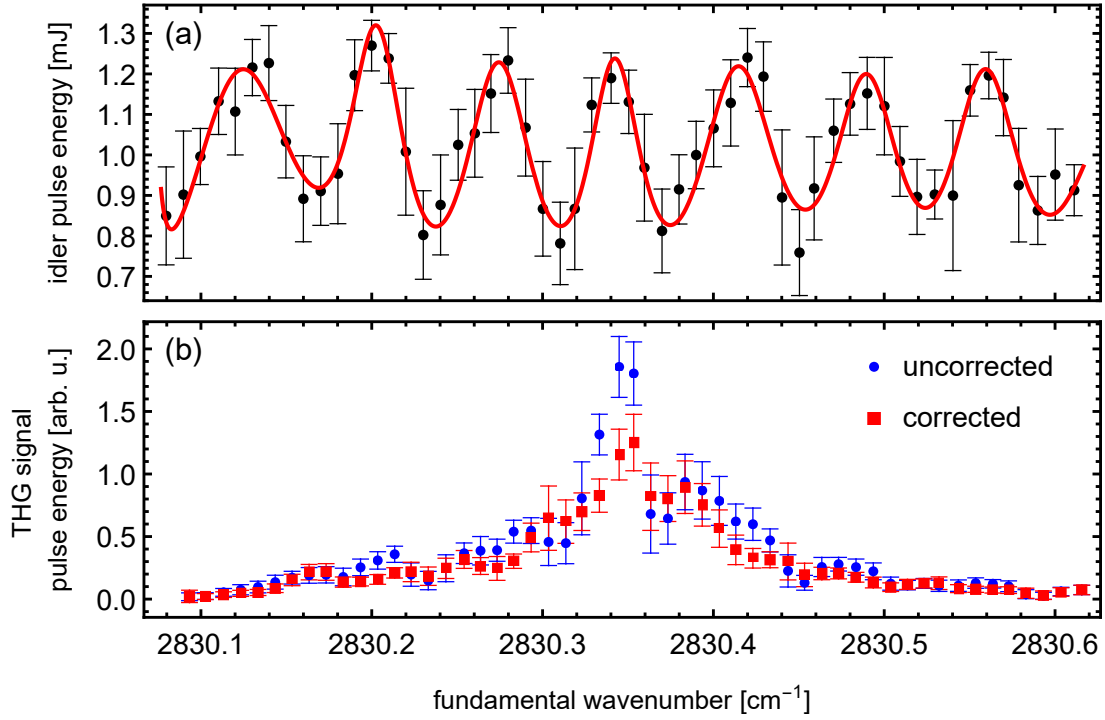


**Figure 2.8:** (a) Idler pulse energy vs. idler frequency modulated by tuning the OPO seed frequency. The pulse energy shows oscillations due to the etalon effect in the power LNB stage. The solid red line indicates a fit (heuristically, a sum of Lorentzian functions). (b) THG spectrum in HCl (see Sec. 3), i.e., THG spectrum, obtained with the idler pulses modulated by the etalon effect. The HCl pressure was 400 mbar. The red data points show the rescaled result, according to Eqn. (2.1) with  $E_{\text{ref}} = 1.02 \text{ mJ}$  and  $\epsilon = 2.2$ . Error bars indicate standard deviations from binning in  $0.01 \text{ cm}^{-1}$  intervals.

according to

$$E_{\text{corr}}(3\omega) = E(3\omega) \times \left( \frac{E_{\text{ref}}(\omega)}{E(\omega)} \right)^\epsilon \quad (2.1)$$

with a reference pulse energy  $E_{\text{ref}} = 1.0 \text{ mJ}$ , the measured pulse energy  $E(\omega)$  and an exponent of the nonlinear process  $\epsilon = 2.2$ . We will discuss the deviation of the exponent from the expected cubic dependence in Sec. 3.2. This simple approach does not fully compensate for the etalon effect in the idler intensity, but already enables determination of resonances at sufficient resolution and signal-to-noise ratio. In an improved version of our setup we will use LNB crystals with wedged surfaces and improved anti-reflection coatings also for the signal wave.

### 2.1.3 Spectral linewidth of the OPA output

We deduce the linewidth of the mid-infrared laser pulses from an absorption spectroscopy in HCl. First, we verify the spectral linewidth of an absorption line of the isotope  $\text{H}^{35}\text{Cl}$  at  $2821.57 \text{ cm}^{-1}$ . At a low HCl pressure of  $\approx 0.1 \text{ mbar}$  the spectral linewidth is given by the Doppler linewidth of  $174 \text{ MHz}$  (FWHM) at room temperature ( $25 \text{ }^\circ\text{C}$ , compare Sec. 3.4.1). In a simultaneous measurement, we detect the transmission of the (ns) mid-infrared pulses through the cell and compare the spectral

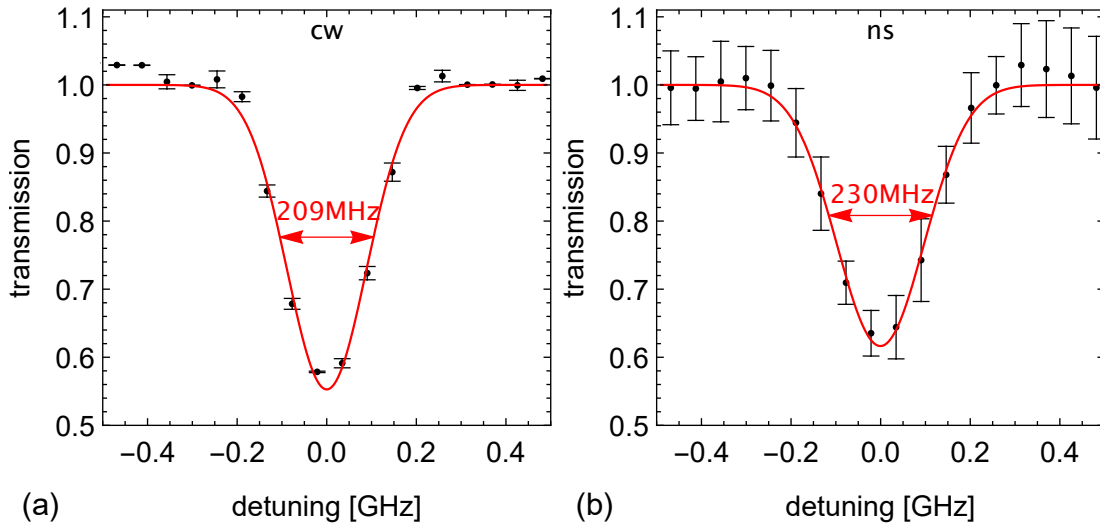


**Figure 2.9:** Transmission vs. fundamental laser detuning on an absorption line at  $\tilde{\nu} = 2821.57 \text{ cm}^{-1}$  ( $N = 3$ ,  $\Delta N = -1$ ,  $H^{35}\text{Cl}$ ) and a HCl-pressure of  $\approx 0.1 \text{ mbar}$  for (a) residual (cw) seed radiation and (b) attenuated nanosecond pulses from the PPLN OPA. Error bars indicate standard deviations, red lines give Gaussian fits to the measurement data.

linewidth with the value for (cw) radiation.

Fig. 2.9 (a) shows the transmission of residual (cw) seed radiation, i.e., the idler output of the commercial OPO, through the 5 cm long gas cell. From a Gaussian fit to the transmission spectrum, we get a spectral linewidth of 209 MHz, i.e., 20% larger than the expected Doppler linewidth. The manufacturer specifies the spectral linewidth of the (cw) OPO output to  $< 1 \text{ MHz}$  (FWHM), i.e., orders of magnitude lower than the observed difference. Hence, the additional bandwidth is probably due to collisional (Dicke) narrowing (compare Sec. 3.12).

We now assume a spectral linewidth of 209 MHz for the resonance in HCl, driven by narrowband (cw) radiation. When we drive the resonance with (ns) pulses, the linewidth increases to 230 MHz, as indicated in Fig. 2.9 (b). This is due to the laser bandwidth of the (ns) pulses. Assuming a convolution of the Gaussian shaped spectral line (linewidth  $\Delta_1$ ) and a Gaussian shaped laser spectrum ( $\Delta_2$ ), we get a convoluted linewidth of  $\Delta_3 = \sqrt{\Delta_1^2 + \Delta_2^2}$ . This calculation yields a laser linewidth of  $\Delta_2 \approx 97 \text{ MHz}$ .

According to the Fourier-transform limit

$$\Delta\tau \Delta\nu \geq \frac{2\ln(2)}{\pi} \approx 0.441, \quad (2.2)$$

with the FWHM of the pulse duration  $\Delta\tau$  and the laser bandwidth  $\Delta\nu$  (FWHM), a laser bandwidth of 97 MHz corresponds to a Fourier limited pulse duration of 4.5 ns. This is lower than the measured pulse duration of the injection seeded pump pulses of the Nd:YAG pump laser pulses with  $\Delta\nu_{\text{pump}} = 8.0 \text{ ns}$ . However, the mid-infrared idler pulses may be shorter than the pump pulses due to the parametric amplification in the power OPA stage. We could not directly determine the pulse duration of the mid-infrared pulses.

From a simplified simulation of the two OPA stages with SNLO [39] we find, that the pulse duration of the idler pulses after the PPLN OPA is equal to the pump pulse duration, as expected. When mixing the idler pulses again with 8 ns long pump pulses in the second and third OPA stage the pulse duration of the amplified idler pulses reduces to  $\approx 6$  ns with an approximately Gaussian shaped temporal pulse profile. The estimated bandwidth of the idler pulses of  $\approx 110$  MHz is larger than the Fourier-limited bandwidth of 74 MHz. This value is not far from the experimentally determined bandwidth. Additional deviations may be due to deformations of the beam profiles by back conversion and Poynting vector walk-off of the pump radiation. Moreover, the bandwidth of the idler pulses may increase due to the large gain and lax quasi-phase-matching conditions in the preamplifier OPA stage [40].

The data discussed above confirms that the spectral bandwidth of the idler pulses from our OPO/OPA setup is quite narrow, i.e., close to the Fourier-transform limit and well below the Doppler-broadened linewidth in HCl. The narrow linewidth is required to efficiently drive THG and permits spectroscopic investigations at large resolution.

## 2.2 Relevant spectroscopic properties of HCl

To demonstrate frequency conversion via rovibrational resonances we require a molecular sample with transitions in the tuning range of our laser system - which at present is defined by the available (cw) OPO. Therefore we choose HCl with an absorption band around  $3.5 \mu\text{m}$  (corresponding to  $2850 \text{ cm}^{-1}$ , expressed in wave numbers). Note, that other molecules like carbon dioxide ( $\text{CO}_2$ ), carbon monoxide (CO) or nitrous oxide ( $\text{NO}_2$ ), i.e., molecules with relevance to combustion processes, may have (according to our estimations) larger nonlinear susceptibilities for THG but their resonances are unavailable with our current laser setup. Nevertheless, future investigations in these molecular species are planned.

We discuss the electronic, vibrational and rotational struc-

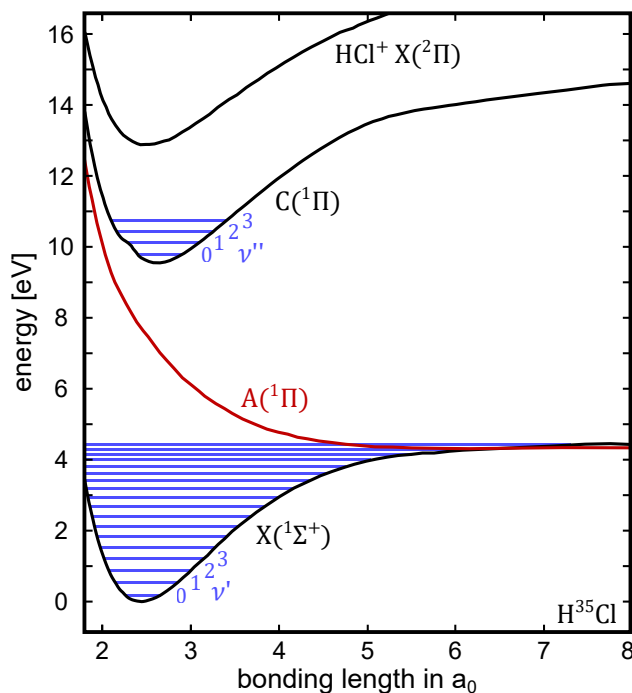


**Figure 2.10:** Potential energy of the ground state  $X(^1\Sigma^+)$  of  $\text{H}^{35}\text{Cl}$ , the first two excited electronic states  $A(^1\Pi)$  and  $C(^1\Pi)$  with optical transitions to the ground state and the ionic state  $X(^2\Pi)$  vs. the internuclear distance given in Bohr radii ( $a_0 = 5.3 \times 10^{-11} \text{ m}$ ) [32, 41–43]. We indicate the vibrational modes of the states  $X(^1\Sigma^+)$  and  $C(^1\Pi)$  by blue lines with vibrational quantum numbers  $v'$  and  $v''$ .

ture of the molecule HCl, which is the relevant molecule for our experimental demonstration. HCl is a simple diatomic molecule with two common isotopes  $\text{H}^{35}\text{Cl}$  ( $\approx 76\%$ ) and  $\text{H}^{37}\text{Cl}$  ( $\approx 24\%$ ) and two less common isotopes  $^2\text{H}^{35}\text{Cl}$  ( $\approx 10^{-2}\%$ ) and  $^2\text{H}^{37}\text{Cl}$  ( $\approx 10^{-3}\%$ ), which we omit in the following discussion. HCl is a relevant molecular species in combustion processes, e.g., waste combustion of polyvinyl chloride (PVC) compounds [44] or biomass [45]. Due to the toxic and corrosive nature, detection of HCl even at low concentrations is highly desirable. Exposure of the human metabolism to HCl can harm the mucous membranes and leads to severe lung conditions [46]. Detection of HCl is further relevant in astrophysics, as HCl is an atmospheric reservoir for chlorine, e.g., on Venus [47].

In addition to electronic states, molecules also possess vibrational and rotational energy levels. HCl has one vibrational stretch mode and rotates around an axis perpendicular to the symmetry axis of the linear molecule. Fig. 2.10 gives the energy levels of the electronic ground state of the isotope  $\text{H}^{35}\text{Cl}$ , the first two excited electronic states with vibrational states for the bound states  $X(^1\Sigma^+)$  and  $C(^1\Pi)$ , as well as the lowest electronic state of the ion  $\text{HCl}^+$ . For illustration purposes we omit rotational states in Fig. 2.10.

Tab. 2.1 summarizes relevant molecular parameters for HCl. We differentiate vibrational constants  $\omega_e$ ,  $\omega_e x_e$  and  $\omega_e y_e$ , as well as rotational constants  $B_e$ ,  $D_e$  and  $\alpha_e$ . These coefficients allow the calculation of the rovibrational energies in HCl of a state, defined by the vibrational quantum number  $\nu$  and the rotational quantum number  $N$  according to the Dunham expansion given by

$$\tilde{E}(\nu, N) = \sum_{k,l} Y_{k,l} (\nu + 1/2)^k [N(N+1)]^l = T_e + \omega_e(\nu + 1/2) + B_e N(N+1) + \dots, \quad (2.3)$$

where  $T_e$  is the minimal electronic energy, given in wave numbers.

Optical transitions are possible between the electronic states  $X(^1\Sigma^+)$  and  $C(^1\Pi)$  in Fig. 2.10. The transition wavelength of electronic transitions is in the ultraviolet spectral range and the transition dipole moments are in the range of  $\mu^{(\text{el})} = 3.7 \times 10^{-30}$  Cm [41]. Furthermore, there are transitions between rotational states in the

**Table 2.1:** Molecular parameters for HCl with corresponding Dunham coefficients  $Y_{k,l}$  [48]. We did not find molecular parameters for the excited state of the isotope  $\text{H}^{37}\text{Cl}$ .

			$X(^1\Sigma^+)$ [49]	$X(^1\Sigma^+)$ [50]	$C(^1\Pi)$ [43]
isotope			$\text{H}^{35}\text{Cl}$	$\text{H}^{37}\text{Cl}$	$\text{H}^{35}\text{Cl}$
$T_e$	$Y_{0,0}$	$\text{cm}^{-1}$	0	0	76092.8
$\omega_e$	$Y_{1,0}$	$\text{cm}^{-1}$	2990.946	2988.660	2817.5
$\omega_e x_e$	$-Y_{2,0}$	$\text{cm}^{-1}$	52.8186	52.720	66.0
$\omega_e y_e$	$Y_{3,0}$	$\text{cm}^{-1}$	0.2243	0.218	-
$B_e$	$Y_{0,1}$	$\text{cm}^{-1}$	10.59341	10.577	9.44
$\alpha_e$	$-Y_{1,1}$	$\text{cm}^{-1}$	0.30718	0.306	0.15
$D_e$	$Y_{0,2}$	$\text{cm}^{-1}$	$5.3194 \times 10^{-4}$	$5.301 \times 10^{-4}$	-
$r_e$		nm	0.127455	-	0.135

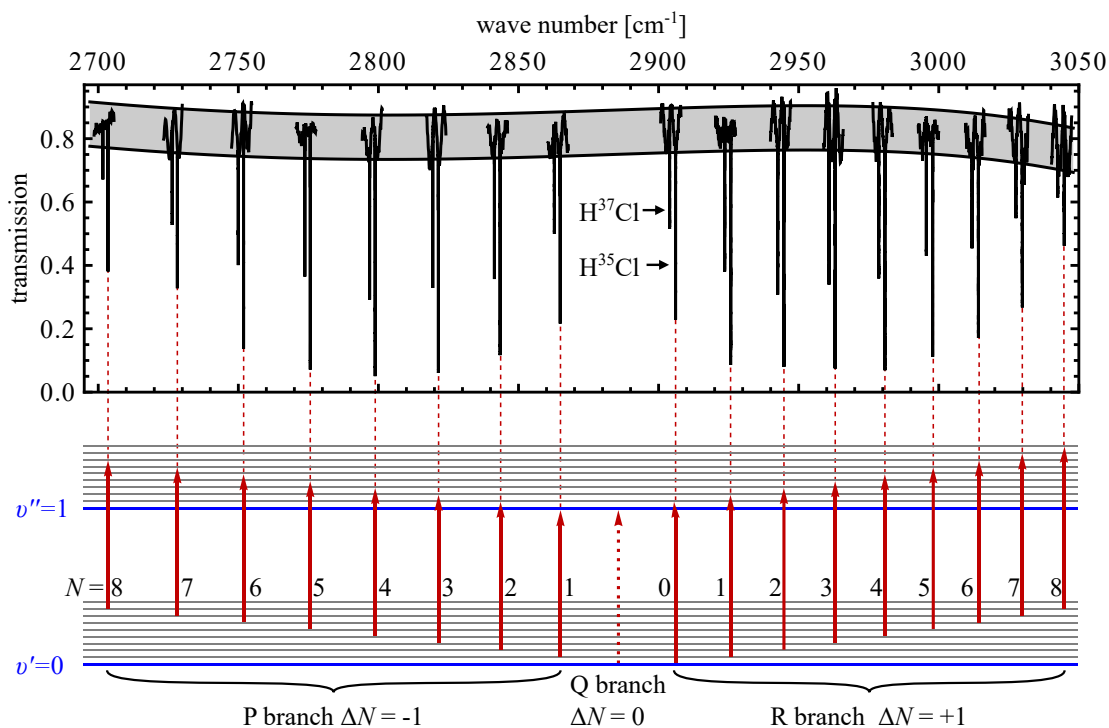


**Figure 2.11:** (upper row) Absorption spectrum of HCl (transmission vs. wave number), measured in a 5 cm long gas cell at a pressure of  $\approx 0.1$  mbar at room temperature  $25^\circ\text{C}$  with narrowband (cw) mid-infrared laser radiation (compare Sec. 2.1). The oscillation of the off-resonant data, indicated by the shaded area, is due to interference in the gas cell. (bottom row) Level schemes of the corresponding transitions in the electronic ground state of  $\text{H}^{35}\text{Cl}$ .

microwave spectral range. Most relevant for our studies are rovibrational transitions, which change the vibrational  $\nu$  and the rotational quantum number  $N$ . These transitions lead to characteristic absorption spectra, typically in the mid-infrared spectral regime for simple molecules. The transition dipole moments are in the range of  $\mu^{(\text{vib})} = 0.2 \times 10^{-30}$  Cm [32], i.e., one order of magnitude smaller, than the electronic transition dipole moments. Optical transitions between electronic states, that also change the vibrational quantum number are called vibronic transitions.

Fig. 2.11 gives an example for the typical absorption spectrum, which we measured at a low HCl pressure. We detected the power of continuously tunable narrowband (cw) laser radiation (compare Sec. 2.1) with photo detectors before and behind a gas cell and calculated the transmission (compare Sec. 2.5.1). In the spectrum we identify sharp spectral lines, which we associate with the two most common isotopes of HCl, i.e.,  $\text{H}^{35}\text{Cl}$  and  $\text{H}^{37}\text{Cl}$  with a mixing ratio of  $\approx 3 : 1$ . Note, that we only measured spectra of  $\approx 200$  GHz in the vicinity of expected resonances to limit the measurement time and to reduce the impact of wall adsorption, i.e., a slight decrease of the cell pressure due to reactions of the HCl molecules with the gas cell [51]. The oscillatory structure, which superimposes the absorption spectrum, originates in an etalon, formed by the uncoated  $\text{CaF}_2$  windows of the gas cell. For further details of the measurement and discussions of the absorption spectrum see [31].

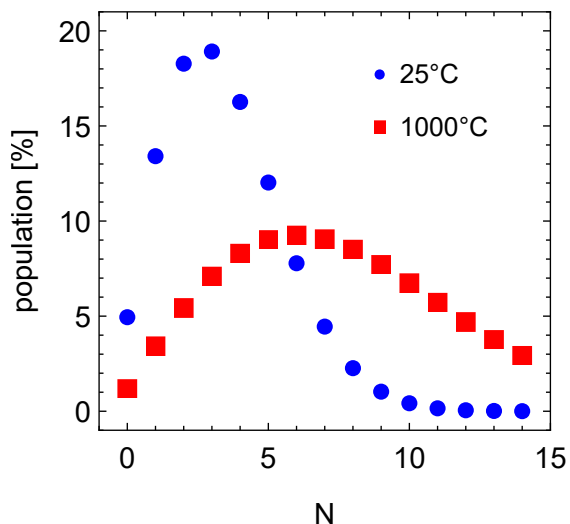


**Figure 2.12:** Thermal population vs. rotational quantum number of the vibrational ground state in  $H^{35}Cl$  for 25 and 1000 °C.

We identify the transitions, corresponding to the detected absorption lines, in the  $\nu = 0 - 1$  band of HCl. The absorption lines are classified in three branches: The band center is called Q branch, where  $\Delta N = 0$ , i.e., the rotational quantum number does not change. This transition is not allowed in the case of HCl, the occurrence of the Q branch depends on the symmetry of the molecule. Transitions on the low energy side of the Q branch reduce the rotational quantum number  $N$  and form the P branch. On the other hand transitions on the high energy side of the Q branch increase the rotational  $N$  quantum number and are part of the R branch. The absorption spectrum

also depends on the thermal occupation of the vibrational ground state  $\nu = 0$ , which follows the normalized Boltzmann distribution

$$\frac{2N + 1}{Z} \exp\left[-\frac{E_{\text{rot}}(N)}{k_B T}\right], \quad (2.4)$$

with the Boltzmann constant  $k_B$ , the energies of the rotational ground states  $E_{\text{rot}}(N) = 100hcB_eN(N + 1) + \dots$  and, as a normalization factor, the sum over all populations  $Z = \sum_{N=0}^{N_{\text{max}}} (2N + 1) \exp[-E_{\text{rot}}(N)/(k_B T)]$ . Fig. 2.12 gives an example of the occupations for the  $H^{35}Cl$  isotope at room temperature (25 °C) and 1000 °C. At 25 °C the state with  $N = 3$  has the highest occupation and only few states have a significant occupation. This is different in the high temperature case. Here, the maximal occupation is reached at  $N = 6$  and the distribution is broader, i.e., the branches of an absorption spectrum would include many more transitions, when compared with our measurement at room temperature (Fig. 2.11).

This is in accordance with our observations in the absorption spectrum, shown in Fig. 2.11. We observe strongest absorption for transitions with the rotational quantum numbers  $N = 2, 3$  and 4 of the ground states. This distribution enables temperature determination with optical methods. It is difficult to determine the precise temperature of HCl from spectroscopic measurements, as the rotational constant  $B_e$  is large. This induces large separations of the absorption lines shown in Fig. 2.11. Therefore, only few rotational states contribute at room temperature [28]. Other molecules, e.g. carbon dioxide ( $CO_2$ ), possess smaller rotational constants  $B_e = 0.39021 \text{ cm}^{-1}$  [49] and are therefore better suited for optical thermometry.

Note, that the selection rule for the vibrational quantum number relaxes in an anharmonic oscillator potential and overtone transitions with  $\Delta \nu = \pm 2, \pm 3, \dots$  are possible, albeit with orders of magnitude smaller transition probabilities, when compared with the strong fundamental absorption band with  $\Delta \nu = \pm 1$ . The second

order Dunham coefficient for the vibrational quantum number,  $x_e$ , in Tab. 2.1 gives an estimate on the relative intensities of the overtone transitions:  $\mu(\Delta\nu = \pm 2) \sim x_e$  and  $\mu(\Delta\nu = \pm 3) \sim x_e^2$  [52]. In the case of  $\text{H}^{35}\text{Cl}$  the parameter is  $x_e = 0.018$ . Hence, the transition moments of the overtone transition with  $\Delta\nu = \pm 3$  are therefore approximately three orders of magnitude smaller than for the  $\Delta\nu = \pm 1$  band. For this reason we expect reabsorption of the third harmonic to be negligible, even in the case of three-photon resonant excitation to states with  $\nu = 3$ . This is a typical case in most molecules.

## 2.3 Sample gas setup

For our investigations we need to setup a gas sample with defined length and control the particle density, i.e., the absolute pressure down to vacuum values. There are essentially two possible experimental arrangements: In a gas cell we can precisely control the HCl pressure and may have a long interaction length. But the damage threshold of the windows used in gas cells limits the maximum fluence of the fundamental radiation. Gas jets allow high peak intensities, as an implementation in a vacuum setup without any optics in the focus region is possible [53]. Due to the size limits of the gas nozzle this approach typically makes implementation of a tight focusing condition necessary. Tight focusing might introduce phasematching issues, that need to be compensated when applying THG, depending on the molecular species [25]. As we have seen in Sec. 1.3, we profit from mild focusing and long interaction lengths. Hence, we choose a gas cell for our measurements.

The gas cell has a length of 5 cm and is sealed with 1 mm thick  $\text{CaF}_2$  windows (CF-W-38-1, ISP Optics). We conduct all measurements in HCl at room temperature (25 °C). The gas has a purity of 99.5% with < 50 ppm residual moisture (supplied by Westfalen). A rotary vane pump (Trivac D16A, Leybold) evacuates the cell down to a residual pressure of  $4 \times 10^{-4}$  mbar (without gas ballast). We control the HCl pressure with a combination of ball (7155G6YMM-ITA, Hoke) and needle valves (orifice of 1°, 1335G6YMM-ITA, Hoke). Fig. 2.13 illustrates the setup.

We monitor the HCl pressure with a corrosion resistant pressure transmitter with a ceramic membrane (Sitrans P200, Siemens). The sensor allows measurements of the absolute pressure down to  $\approx 1$  mbar (see Appendix B). Besides operation at a constant HCl pressure, we can also dilute HCl in nitrogen or maintain a constant flow through the gas cell.

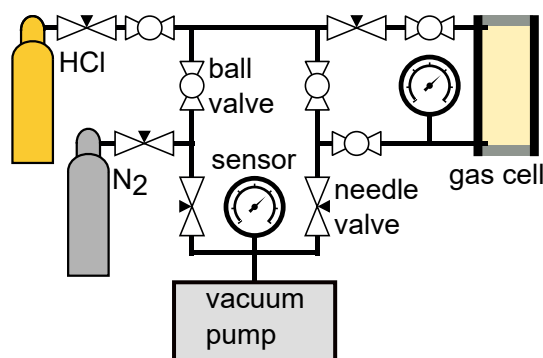
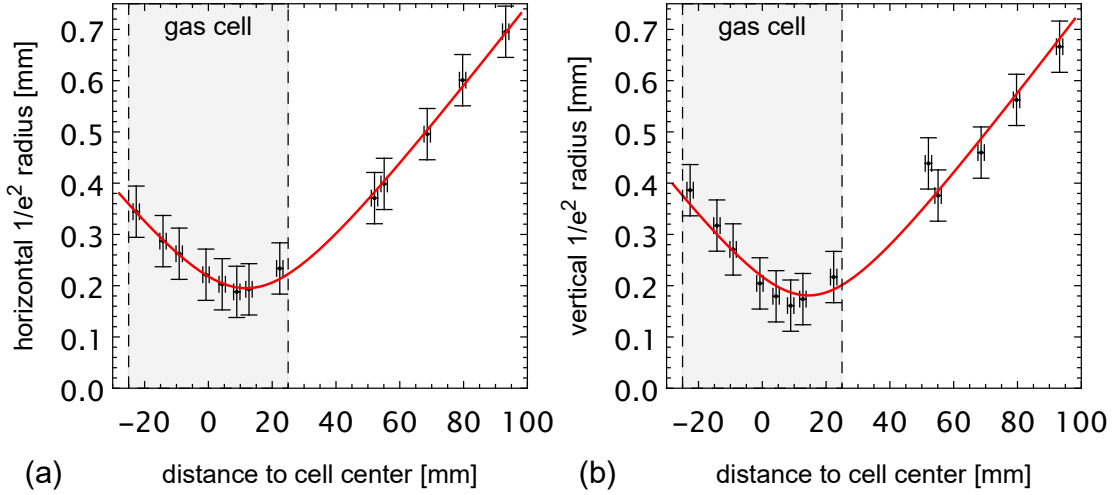


Figure 2.13: Schematic view of the gas setup.



**Figure 2.14:** Variation of the (a) horizontal and (b) vertical  $1/e^2$  radius in the interaction region vs. propagation distance, measured from the center of the gas cell. The central wavelength was 3534 nm. Solid lines depict fits of a Gaussian beam with the beam quality factor  $M^2$  as a fit parameter. The shaded area indicates the position of the gas cell. Error bars indicate standard deviations due to systematic errors of the measurement method.

**Table 2.2:** Fit parameters for the focus of the mid-infrared fundamental radiation.

fit parameter	unit	horizontal	vertical
focus position $z_0$	mm	12(1)	14(2)
$1/e^2$ radius $w_0$	$\mu\text{m}$	182(20)	184(20)
confocal parameter $b$	mm	58.8(4)	61(1)
beam quality factor $M^2$		1.42(3)	1.3(1)

## 2.4 Focusing conditions

We analyse the focus of the fundamental mid-infrared radiation in the position of the gas cell. A  $\text{CaF}_2$  lens with a focal length of 150 mm (LA5012-E, Thorlabs, L1 in Fig. 2.1) mildly focuses the fundamental radiation. We measure beam profiles with the home-built moving-aperture beam profiler (20  $\mu\text{m}$ -diameter aperture). Fig. 2.14 shows the beam radii in the gas cell.

We find good agreement of the data with a fit of a Gaussian beam, modified with the beam quality factor  $M^2$  as a fit parameter given by

$$w(z) = w_0 \sqrt{1 + \left( M^2 \frac{\lambda(z - z_0)}{\pi w_0^2} \right)^2}. \quad (2.5)$$

Tab. 2.2 gives the results of the nonlinear fits. The focus position deviates slightly from the center of the gas cell towards the back window. This does not significantly reduce the THG yield, due to the mild focusing. For positive wave vector mismatches  $\Delta k$  we might, according to Eqn. (1.7), even profit from this configuration with regard to focusing to the center of the gas cell. Hence, we do not change the focus

position in the following experiments. We include the offset in our calculations of the phase matching integral.

We determine the  $1/e^2$  radius of the Gaussian beam to  $\approx 180 \mu\text{m}$ . Hence, the beam diameter is a factor of 18 larger than the aperture and we can neglect the convolution with the aperture. The beam quality factors are in the range of 1.3 – 1.4. Hence, the beam profile of the fundamental radiation deviates from a perfect Gaussian profile. The beam quality influences the THG conversion efficiency. We do not account for these deviations from a Gaussian beam profile in our simulation (see 1.1).

Note, that the stated beam quality factors of the mid-infrared radiation represent just a rough estimation due to limitations of our beam profiling solution. The main problem is the long acquisition time for a single frame (typically in the range of 10 min). Unfortunately, commercially available mid-infrared beam profiling solutions are not applicable to our experimental conditions. For example, microbolometer cameras, which detect absorption of mid-infrared radiation, are not sensitive enough for nanosecond pulses at fairly low repetition rates (10 – 20 Hz). We also conducted, without success, a test in our lab of a mid-infrared camera based upon the pyroelectric effect, including an integrated chopper for (cw) detection (Pyrocam IV, Ophir). Low damage thresholds for the residual (cw) power present in our setup, low sensitivity for pulsed radiation and a limited pixel size of  $80 \mu\text{m}$  prohibit a proper application in our case.

## 2.5 Detection setup

In the experiments we require two types of detectors: For absorption measurements at macroscopic light levels of the mid-infrared fundamental (cw) or (ns) radiation we use Indium Arsenide Antimonide (InAsSb) photovoltaic detectors (P13243-011MA, Hamamatsu Photonics). These detectors have reasonable photo sensitivities in the range of  $4 \text{ mA/W}^{-1}$  and flat spectral response on the range of  $2.7 - 5 \mu\text{m}$ , as well as rise times in the nanosecond range.

In the experiments on resonantly enhanced frequency conversion, we generate THG signal pulses in the near-infrared, e.g., at  $1178 \text{ nm}$  for HCl. At a low HCl pressure of 1 mbar we expect a conversion efficiency of  $10^{-10}$ . For a fundamental pulse energy of 1 mJ this corresponds to roughly  $10^6$  photons per pulse. To detect such signals we use an Indium gallium arsenide (InGaAs) avalanche photodiode (APD, IAG200S6, Laser Components). At the THG signal wavelength of  $1178 \text{ nm}$  the typical photo sensitivity is  $7 \text{ A/W}$  and the quantum efficiency is larger than  $75\%$  <sup>2</sup>.

We convert the current signal from the APD and the mid-infrared photovoltaic detectors into a voltage signal with variable gain transimpedance amplifiers (DLCPA-200, Femto). A digital oscilloscope (Picoscope 4824, Pico Technology) integrates the voltage signal to yield a measure for the THG pulse energy.

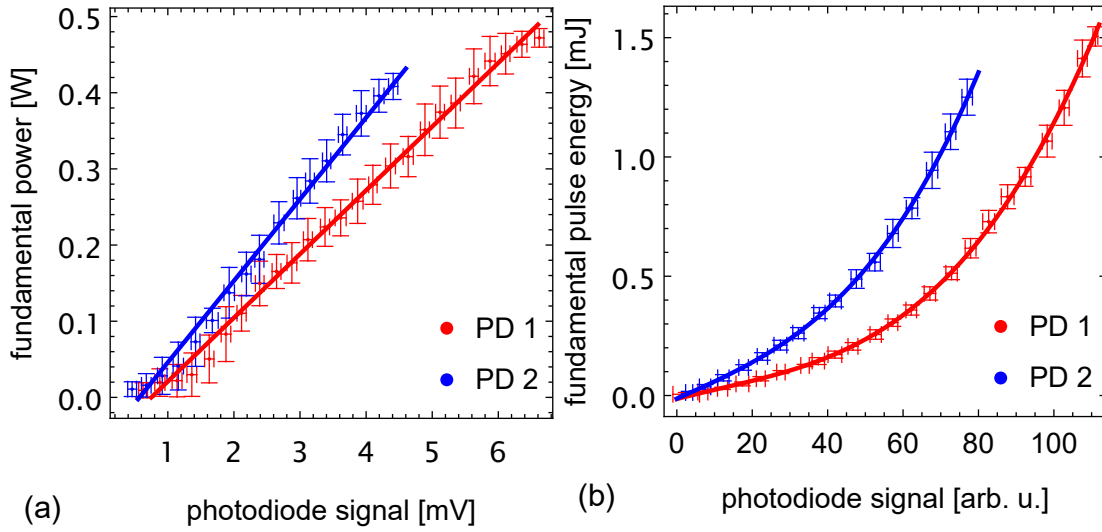


**Figure 2.15:** (a) Power of residual (cw) fundamental mid-infrared radiation vs. averaged signal of the InAsSb sensor. Lines indicate linear fits. (b) Fundamental (ns) pulse energy vs. integrated signal of the InAsSb sensor. Lines indicate polynomial fits of order 3. PD1 is placed in front of the gas cell and PD2 behind the cell. Error bars display standard deviations.

### 2.5.1 Calibration of the mid-infrared monitoring setup

The THG signal pulse energy depends in third power on the driving fundamental intensity. Thus, for shot-to-shot measurements we have to monitor the fundamental (ns) pulse energy. For the absorption measurements we observe the residual (cw) radiation before and behind the gas cell (compare Fig. 2.1). We detect the (cw) power and the (ns) pulse energy with the same InAsSb detector. Both beams propagate collinearly behind the OPA chain. We pickup a reflex from uncoated  $\text{CaF}_2$  windows and block the second reflection (from the backside of the window) with an aperture. We further attenuate the signal by reflection off an uncoated BK7 window and focus the radiation with uncoated  $\text{CaF}_2$  lenses ( $f = 40$  mm, LA5370, Thorlabs) onto the detectors.

For a characterisation of the monitoring setup for the fundamental (cw) power, we vary the power with the variable attenuator. An thermophile based sensor (3A, Ophir) measures the actual (cw) power in front of the gas cell (analogous for the second detector behind the evacuated gas cell). Fig. 2.15 (a) shows the expected linear dependency for both detectors. The constant offset of  $\approx 1$  mV is an artifact of the transimpedance amplifier. We determine a system transmission of  $\approx 86\%$  for the fundamental radiation (mainly because of Fresnel losses at the uncoated  $\text{CaF}_2$  windows of the gas cell and the collimation lens).

To monitor the fundamental (ns) pulse energy, we verify the linearity of the InAsSb detectors. Hence, we measure the fundamental pulse energy with a factory-calibrated pyroelectric sensor (PE10-C, Ophir) placed in front of the gas cell. We repeat this measurement for the second detector behind the gas cell. Fig. 2.15 (b) gives the result for both detectors. We observe saturation for fundamental pulse energies

<sup>1</sup>Datasheet from manufacturer Hamamatsu Photonics

<sup>2</sup>Datasheet from manufacturer Laser Components

beyond  $200 \mu\text{J}$ . Hence, we fit a polynomial function of order 3 to the data points to compensate for the deviations. The system transmission for the (ns) pulses is  $\approx 83\%$ , i.e., close to the value determined for (cw) radiation.

## 2.5.2 Calibration of the THG detection setup

In our experiments on resonantly enhanced THG we also tried to determine the absolute efficiency (and, hence, the nonlinear susceptibility), i.e., the ratio of output THG signal photons vs. input fundamental photons. To this end, we require the measurement of the absolute number of THG signal photons and, hence, calibration of the APD. Moreover, we require the total transmission of the detection beam line, i.e., the ratio of THG signal photons, which is left after propagation from the gas cell to the APD.

Fig. 2.16 shows the detection setup in detail. The uncoated  $\text{CaF}_2$  lens L2 ( $f = 250 \text{ mm}$ , LA5255, Thorlabs) collimates the THG, which originates in the gas cell. We spectrally separate the THG from the fundamental mid-infrared radiation with a  $\text{CaF}_2$  Pellin Broca prism (ADBV-10, Thorlabs, PBP in Fig. 2.16). Two mirrors with protected silver coatings (PF10-03-P01, Thorlabs) align the THG onto lens L3 with a focal length of  $75 \text{ mm}$  (LA1608-C, Thorlabs). Focusing is necessary, as the APD has a small active diameter of  $200 \mu\text{m}$ . Hence, we control the position of the APD with a translation stage. We reduce stray light with two apertures. Two edgepass filters suppress wavelengths above  $1250 \text{ nm}$  (#89-675, Edmund Optics, F1 in Fig. 2.16) and below  $1100 \text{ nm}$  (FELH1100, Thorlabs, F2 in Fig. 2.16). Neutral density filters reduce (if required) the THG signal fluence on the APD (F3 in Fig. 2.16).

For measurement of the transmission of the detection beam line we generate radiation at the THG wavelength on a macroscopic signal level, which we can measure with a power meter (3A, Ophir). In our experiment, we use a commercial optical parametric oscillator (OPO Fan, APE Angewandte Physik & Elektronik GmbH) for picosecond (ps) pulses, which is tunable in the visible ( $500 - 700 \text{ nm}$ ) and near-infrared regime ( $1000 - 1400 \text{ nm}$ ). The OPO is pumped by a Titan:sapphire oscillator (Mira 900P, Coherent). The Titan:sapphire oscillator is pumped by a frequency doubled diode-pumped solid-state laser (finesse 14W, Laser Quantum, DPSSL in Fig. 2.16). The resulting (ps) pulses have typical pulse durations of  $2 \text{ ps}$  and a repetition rate of  $76 \text{ MHz}$ . Due to the large repetition rate and the low bandwidth of the transimpedance amplifier and the digital oscilloscope, which integrates the signal, we can consider the (ps) pulse train as quasi-(cw) radiation. We measure a central wavelength of  $1180.5 \text{ nm}$  with a bandwidth of  $6 \text{ nm}$  (measured with a rotating grating spectrometer, APE Angewandte Physik & Elektronik GmbH).

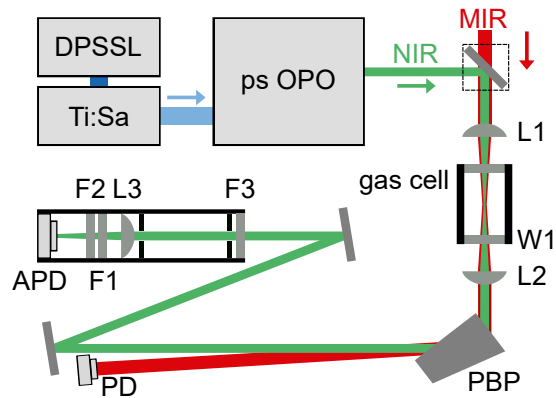


**Figure 2.16:** Detailed view of the THG detection and calibration setup.

**Table 2.3:** *Transmissions for relevant elements of the THG detection setup.*

element	abbreviation	transmission
cell window	W1	$\approx 94\%$ [54]
collimation lens	L2	$\approx 94\%$ [54]
THG lens	L3	96.3 %
Pellin Broca prism	PBP	77.6 %
shortpass 1250 nm	F1	99.4 %
longpass 1100 nm	F2	98.7 %

Tab. 2.3 summarizes the transmissions of the relevant optical elements of the THG beam path. The transmissions for the uncoated  $\text{CaF}_2$  optics derive from the known Fresnel equations for  $\text{CaF}_2$  [54]. The reflectivity of the silver mirrors is  $R_{\text{Ag}} \approx 0.976$  at an assumed angle of incidence of  $12^\circ$ <sup>3</sup>. Without inclusion of the optional neutral density filters F3 the system transmission for radiation at the THG wavelength is

$$T_{\text{total}} = T_{\text{W1}} T_{\text{L2}} T_{\text{PBP}} R_{\text{Ag}}^2 T_{\text{L3}} T_{\text{F1}} T_{\text{F2}} \approx 61.9\%. \quad (2.6)$$

The output photo current  $I$  of the APD depends as follows on the actual power of the THG signal radiation  $P_{\text{signal}}$ :

$$I = G_{\text{APD}} T_{\text{total}} P_{\text{signal}}, \quad (2.7)$$

with the responsivity of the APD  $G_{\text{APD}}$ . The responsivity is the product of the photo sensitivity of the APD and an internal amplification factor. The latter is achieved by a bias voltage, which allows photo electrons to produce secondary electrons, i.e., increasing the sensitivity of the detector far beyond conventional photo diodes. The transimpedance amplifier turns the current signal into a voltage signal with a gain of  $G_{\text{F}} = 10^6 \text{ V/A}$ .

To calibrate the APD, we propagate a well-known fraction (optical density  $\approx 5.7$ ) of the quasi-(cw) radiation at THG wavelength on the APD and measure the output current. Fig. 2.17 gives the resulting photo current. The data for both bias voltages shows a linear dependence on the incident power (compare the linear fits in Fig. 2.17). The offset of  $\approx 0.2 \mu\text{A}$  indicates the dark current, i.e., the current measured without radiation. The dark current depends exponentially on the bias voltage. The slope of the linear fits in Fig. 2.17 is the responsivity of the APD. We find  $G_{\text{APD}}(60\text{V}) = 4 \text{ A/W}$  and  $G_{\text{APD}}(66\text{V}) = 42 \text{ A/W}$ . We operate the APD with a bias voltage of 66 V for all measurements in this work.

Note, that we conducted these measurements with quasi-(cw) radiation at the THG signal wavelength. The actual THG signal radiation consists of weak laser pulses with a pulse duration of  $\approx 8 \text{ ns}$ . While the APD has a bandwidth of 1 GHz, the transimpedance amplifier has a bandwidth of only 200 kHz. Hence, we detect an impulse with a duration of  $\approx 2.5 \mu\text{s}$ . The signal pulse energy is then

<sup>3</sup>Datasheet from the manufacturer: Protected Silver Coating -P01 from Thorlabs.

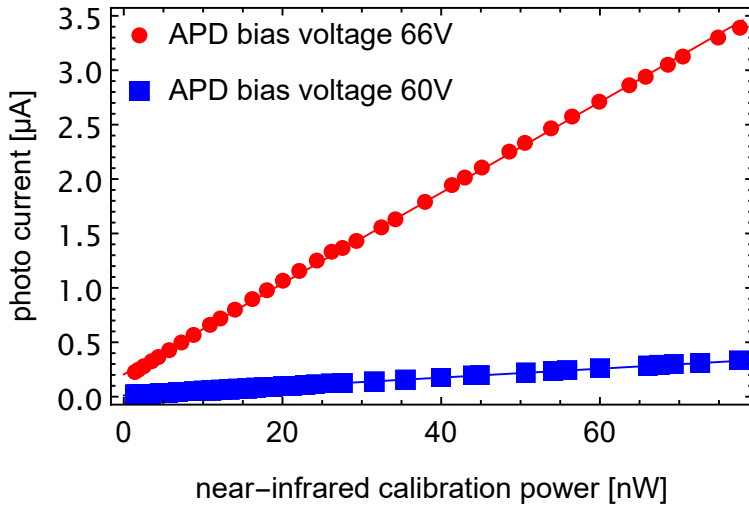


**Figure 2.17:** Output photo current of the APD vs. quasi-(cw) calibration power for two APD bias voltages. The transimpedance gain was  $G_F = 10^6$  V/A and the central wavelength 1180.5 nm. Lines indicate linear fits.

$$E_{\text{pulse}} = \int P_{\text{signal}} dt = \frac{1}{G_F G_{\text{APD}}} \int U dt \approx \frac{1}{G_F G_{\text{APD}}} \sum U \Delta t. \quad (2.8)$$

Note, that we replaced the integral with a discrete sum. This is necessary, as the digital oscilloscope samples with a temporal resolution of  $\Delta t = 25$  ns/sample. The actual THG signal pulse energy, which originates in the gas cell is  $E_{\text{pulse}}/T_{\text{total}}$  with the system transmission given by Eqn. (2.6). Assuming an integration window with a duration of  $2.5 \mu\text{s}$ , the peak quasi-(cw) power in Fig. 2.17 corresponds to  $\approx 10^6$  photons with a wavelength of 1180 nm, i.e., the expected number of photons per pulse in THG experiments. With this simplified calculation we assumed, that the APD converts the same number of photons equivalently, without difference for the pulse duration. Note, that this assumption is probably wrong due to the different response of the APD to (cw) and (ns) signals, even with similar peak powers. Therefore, all absolute values for the THG signal pulse energy in this work represent only an order of magnitude estimation.

Due to the small active diameter of the APD the detection setup is sensitive on misalignment. We verify that the APD captures the whole THG beam profile by translation along two perpendicular axes. Fig. 2.18 gives the result of the measurement. A convolution of the active area of the APD ( $200 \mu\text{m}$ ) and the  $1/e^2$  radius of the THG focus  $w_0$ , given by

$$f(z) \propto \text{erf} \left[ \frac{2(z + 100 \mu\text{m})}{\sqrt{2}w_0} \right] - \text{erf} \left[ \frac{2(z - 100 \mu\text{m})}{\sqrt{2}w_0} \right]. \quad (2.9)$$

describes the data well. In the horizontal axis  $w_0$  is  $70 \mu\text{m}$  and in the vertical axis  $63 \mu\text{m}$ . These values indicate a slight asymmetry of the focus and good accordance with the estimated  $1/e^2$  radius of  $\approx 60 \mu\text{m}$  for lens L3 ( $f = 75$  mm, LA1608-C, Thorlabs). We verified, that the dispersion of the Pellin Broca prism has a negligible influence on the position of the THG focus on the APD for THG wavelengths between 1170 and 1195 nm. This allows spectroscopic investigations without the necessity to align the angle of the Pellin Broca prism.

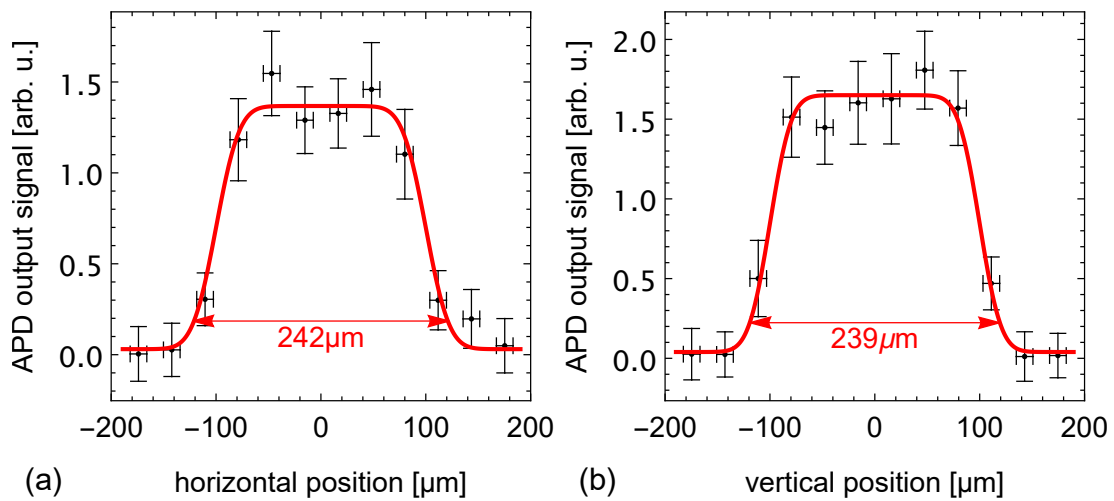


**Figure 2.18:** APD output signal vs. position of the APD in (a) horizontal and (b) vertical direction. The position is determined from incremental revolutions of a screw with a pitch of  $254\mu\text{m}/\text{rev}$  (CXY1, Thorlabs). The red line indicates a fitted convolution of the active area of the APD and the Gaussian focus of the THG ( $1/e^2$  width stated in the plot). Error bars give standard deviations.

## Chapter 3

# Experimental results of THG

In this chapter we present the results from a thorough experimental analysis of resonantly enhanced THG and indicate the potential for selective detection of molecular species. First, we compare the THG yield of two- and three-photon resonances and discuss a numerical simulation. Further we analyse dependencies of the THG signal pulse energy upon the intensity of the fundamental laser pulses and the HCl pressure. Finally, we discuss the detection limit of our approach. The main results presented in this chapter were published in "Physical Review A" [55].

### 3.1 Spectroscopic investigations

In a first spectroscopic investigation we demonstrate the selective detection of both common isotopes of HCl molecules. Fig. 3.1 (upper row) shows an overview THG spectrum, when we tune the driving fundamental pulses in the vicinity of one-, two-, and three-photon resonances between the vibrational ground state  $\nu = 0$  and excited states  $\nu = 1, 2, 3$ . Fig. 3.1 (middle row) shows a (cw) transmission spectrum with one-photon resonances for comparison and frequency calibration. Fig. 3.1 (lower row) shows the transmission of the driving (ns) fundamental pulses. In the THG spectrum we observe many strong, spectrally narrow multi-photon resonances with a large dynamic range (or signal-to-noise-ratio) of three orders of magnitude. The small background signal is mainly generated by off-resonant THG in the CaF<sub>2</sub> windows of the gas cell. As expected, on single-photon resonances we get only little (if any) resonance enhancement of THG emission. In this case the fundamental radiation is strongly absorbed - which significantly effects the THG yield due to its nonlinear dependence upon the third power of the fundamental intensity. However, we observe large THG resonance enhancements by many orders of magnitude on two-photon and three-photon resonances. Though the two-photon resonances (see spectral lines around 2830 cm<sup>-1</sup>) are the strongest, we observe almost comparable resonance enhancement on three-photon resonances (see spectral lines around 2810 cm<sup>-1</sup>). On the first glance the latter seems surprising, as one-photon reabsorption of the harmonic signal should reduce the THG yield on a three-photon resonance for the fundamental radiation. However, the transition moment for a one-photon overtone transition between the vibrational ground state  $\nu = 0$  and the excited state  $\nu = 3$  is very small, due to the small anharmonicity of the potential (compare Sec. 2.2). We calculated the reabsorption of the THG signal to be less than 1 % along the full path length of our gas cell ( $L = 5$  cm). Thus, reabsorption of the THG signal plays no role neither for two-photon nor three-photon resonances.

We compare our experimental results with our straightforward numerical simulation of the THG yield vs. driving laser frequency (compare Sec. 1.1). As the THG spectrum in Fig. 3.1 shows, the simulation fits well with the experimental data and

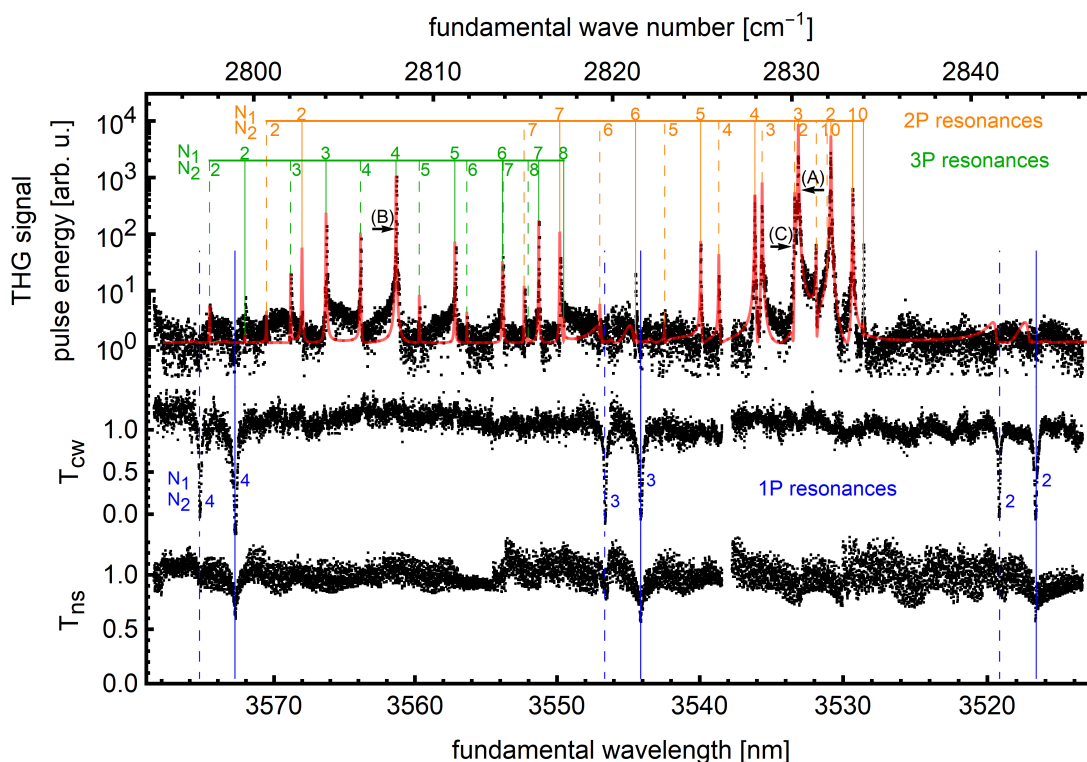


**Figure 3.1:** (upper row) THG signal pulse energy vs. fundamental laser wavelength (or wave number). The HCl pressure was 100 mbar and the mean fundamental laser pulse energy was 1.5 mJ. Black dots indicate experimental data, binned in frequency intervals of  $0.005 \text{ cm}^{-1}$ . We do not account for pulse energy fluctuations. The red line shows a numerical simulation (scaled to fit the experimental data, offset added to describe the background). Vertical orange and green lines (solid line for the isotope  $\text{H}^{35}\text{Cl}$ , dashed for the isotope  $\text{H}^{37}\text{Cl}$ ) indicate the frequency positions of multi-photon resonances, labelled with the corresponding rotational quantum numbers  $N_i$  of the ground state in the transition ( $N_1$ :  $\text{H}^{35}\text{Cl}$ ,  $N_2$ :  $\text{H}^{37}\text{Cl}$ ). Note the logarithmic scale of the THG signal pulse energy axis. (middle row) Transmission spectrum, driven by residual (cw) radiation from the OPO, with one-photon resonances indicated by blue lines. At the rather large HCl pressure used for this overview spectrum, the spectral lines are collisionally broadened to roughly 1.5 GHz. (lower row) Transmission spectrum of the driving fundamental (ns) pulses. We corrected the transmission spectra for oscillations due to the plane gas cell windows and drifts due to the dispersion of the Pellin Broca prism.

confirms all major spectral lines in the experimental data. We resolved resonances with the vibrational ground state of both abundant HCl isotopes up to a rotational quantum number of 7, i.e., a relative occupation of  $< 5\%$  (see Fig. 2.12). This demonstrates the capability of THG for molecule detection, even for mixtures of different isotopes. We note two smaller deviations of the simulation from the experimental data: The simulation predicted also a two-photon resonance of moderate line strength at  $2802.7 \text{ cm}^{-1}$  ( $\text{H}^{35}\text{Cl}$ ,  $N_1 = 2$ ) - though we did not observe it. On the other hand, we observed a two-photon resonance at  $2834.0 \text{ cm}^{-1}$  (contribution from  $\text{H}^{35}\text{Cl}$  with  $N_1 = 0$ ), which proved to be stronger than expected by the simulation. Apart from these findings, the simulation describes the vast majority of the data in Fig. 3.1 very well.

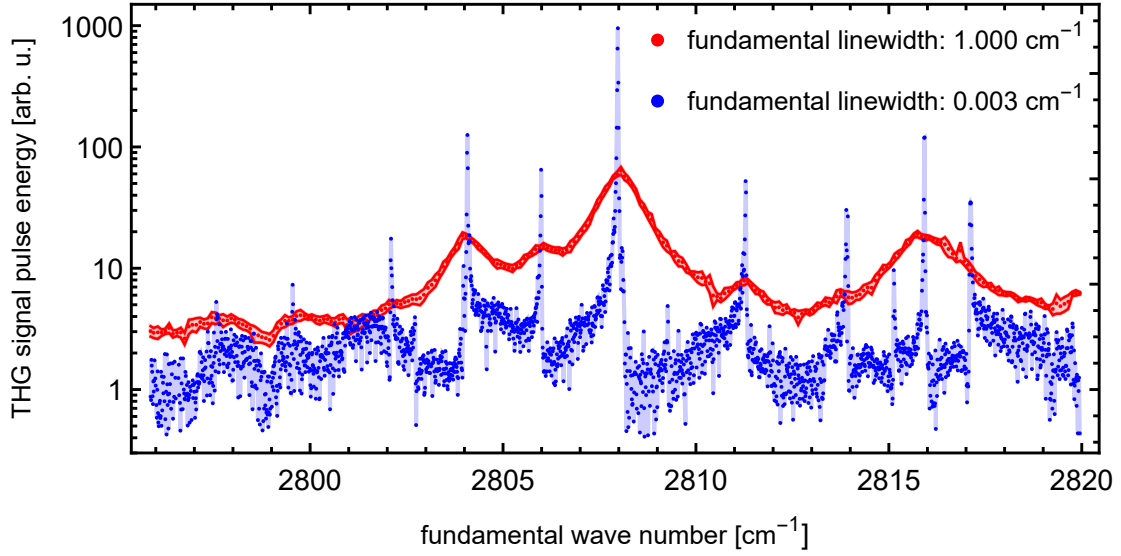


**Figure 3.2:** THG signal pulse energy vs. fundamental wave number for three-photon resonances at a HCl pressure of  $\approx 100$  mbar and a mean fundamental laser pulse energy of 1 mJ. Red dots indicate experimental data measured with broadband mid-infrared pulses (binned in frequency intervals of  $0.1 \text{ cm}^{-1}$ ). Blue points show data measured with narrowband mid-infrared pulses (binned in frequency intervals of  $0.01 \text{ cm}^{-1}$ ). The approximate spectral linewidths are given as FWHM. Note the logarithmic scale.

According to Eqn. (1.11) the resonant nonlinear susceptibility  $\chi^{(3)} \sim 1/\gamma$  depends on the dephasing rate  $\gamma$  of the resonant state, i.e., the linewidth of the single-photon transition. At a HCl pressure of  $\approx 100$  mbar collisional broadening dominates and the spectral linewidth of the resonance is  $\approx 1.5$  GHz (FWHM, corresponding to  $0.05 \text{ cm}^{-1}$ ). In the experiment we have to consider the linewidth of the fundamental pulses, as differences between the laser and the resonance linewidth might reduce the resonance enhancement.

To demonstrate this effect, Fig. 3.2 shows two THG spectra, measured with broadband ( $\Gamma_{\text{bb}} \approx 30$  GHz,  $\approx 1 \text{ cm}^{-1}$ , FWHM) and narrowband fundamental mid-infrared laser pulses ( $\Gamma_{\text{nb}} \approx 0.1$  GHz,  $\approx 0.003 \text{ cm}^{-1}$ , FWHM). With narrowband fundamental radiation we observe sharp spectral lines with a dynamic range of  $\approx 3$  orders of magnitude (as discussed above). In the other case the resonances are broadened to an extent where multiple lines overlap. Weaker resonances are not distinguishable from a constant background signal. The dynamic range is only  $\approx 1$  order of magnitude. The ratio of the approximate linewidths of the fundamental laser pulses is  $\Gamma_{\text{bb}}/\Gamma_{\text{nb}} = 300$ . However, we have to take into account the spectral linewidth of the resonance for determination of the resonance enhancement. With a linewidth of  $\Gamma_{20} = 1.5$  GHz (at a pressure of 100 mbar) we expect a gain of  $\sqrt{\Gamma_{\text{bb}}^2 + \Gamma_{20}^2}/\sqrt{\Gamma_{\text{nb}}^2 + \Gamma_{20}^2} \approx 20$  with the narrowband fundamental laser pulses. Indeed, the lower bandwidth increases the resonant THG signal pulse energy by a factor of  $\approx 15$ . In addition, the background signal reduces by a factor of  $\approx 3$ . Hence, as expected, the larger spectral resolution and larger spectral intensity obtained from the narrowband pulses significantly improves the signal yield and spectral selectivity.

### 3.1.1 Two-photon resonance

In the previous section we noticed two types of resonances, which contribute to the THG spectrum: Resonances, where either the second or the third mid-infrared photon is in resonance with a rovibrational state in HCl. In this section we analyse the resonance enhancement on two-photon resonances of both common HCl-isotopes in some more detail. Finally, we compare our simulation results with experimental data.

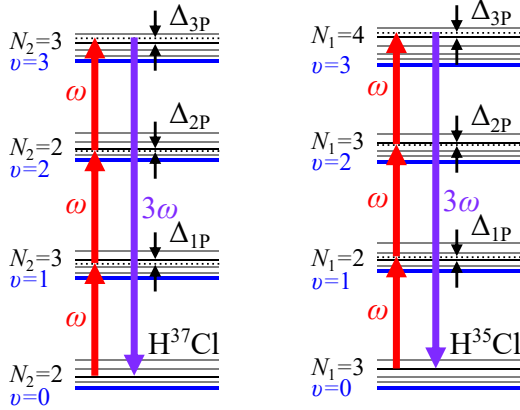


**Figure 3.3:** (left) Level scheme of the two-photon resonance (C) at fundamental wave number  $2830.15 \text{ cm}^{-1}$  and (right) of the two-photon resonance (A) at fundamental wave number  $2830.36 \text{ cm}^{-1}$ .

rule  $\Delta N = \pm 1$  for rovibrational transitions multiple four-level systems contribute to the nonlinear susceptibility. For simplicity, we restrict our discussion to the four-level system with minimal detunings to intermediate states, i.e., the biggest contribution to the nonlinear susceptibility. In this case the one-photon detuning from the ground state  $(\nu, N_1) = (0, 3)$  to the intermediate state  $(\nu, N_1) = (1, 2)$  is roughly  $-8.8 \text{ cm}^{-1}$ , the two-photon detuning to the intermediate state  $(\nu, N_1) = (2, 3)$  is zero, and the three-photon detuning to the target state  $(\nu, N_1) = (3, 4)$  is  $-79.0 \text{ cm}^{-1}$ . Thus, also on two-photon resonance, the one- and three-photon detunings are quite small (e.g., compared to typical detunings of some  $1000 - 10000 \text{ cm}^{-1}$  as in CARS). We note, that absorption losses are still negligible, as the one-photon detunings are still large compared to the linewidth, even at larger collisional broadening (at 100 mbar we get a broadened linewidth of 1.5 GHz, corresponding to  $0.05 \text{ cm}^{-1}$ , compare Sec. 3.4.1). As this value is much larger than the laser linewidth of  $\approx 0.1 \text{ GHz}$ , we omit the laser linewidth in our calculations. Tab. 3.1 summarizes these parameters and gives the transition dipole moments, which we take from the HITRAN database [32]. We calculate the third-order susceptibility to  $(-0.01 + i 20.56) \text{ pm}^2/\text{V}^2$ . Note, that this value includes the sum over all intermediate states according to Eqn. (1.10), as well as contributions from neighboring states in the molecular level scheme (compare the right side of Fig. 3.3). The real component of  $\chi^{(3)}$  is negligible in comparison to the imaginary component, hence, the THG signal pulse energy at resonance (A) features

The strongest two-photon resonance at  $2830.36 \text{ cm}^{-1}$ , labelled (A) in Fig. 3.1, benefits from the large thermal population of the ground state  $(\nu, N_1) = (0, 3)$  (at room temperature we have 18.9% of the  $\text{H}^{35}\text{Cl}$  population in this state). With the abundance of 75.8% of the isotope  $\text{H}^{35}\text{Cl}$  the number density is  $3.5 \times 10^{23} \text{ m}^{-3}$  at a HCl pressure of 100 mbar and a temperature of  $25 \text{ }^\circ\text{C}$ . The right side of Fig. 3.3 shows the level scheme of the four-level system, which contributes most to the nonlinear susceptibility for THG.

The resonant wave number corresponds to the energy difference of the states  $(\nu, N_1) = (0, 3)$  and  $(\nu, N_1) = (2, 3)$ . Due to the selection

**Table 3.1:** Calculated parameters of selected THG resonances (A,B,C) for pressure  $p_{\text{HCl}} = 100$  mbar, temperature  $T = 298.15$  K, fundamental pulse energy  $E_{\text{fund}} = 1.2$  mJ, fundamental pulse duration  $\tau = 8$  ns, gas cell length  $L = 5$  cm, confocal parameter  $b = 6$  cm, and focus position  $z_0 = 3.65$  cm.

resonance	unit	(A)	(B)	(C)
$\nu_{\text{res}}$	$\text{cm}^{-1}$	2830.36	2807.92	2830.15
isotope		$\text{H}^{35}\text{Cl}$	$\text{H}^{35}\text{Cl}$	$\text{H}^{37}\text{Cl}$
$\Delta_{1\text{P}}$	$\text{cm}^{-1}$	-8.8	-9.0	11.4
$\Delta_{2\text{P}}$	$\text{cm}^{-1}$	0	40.0	0
$\Delta_{3\text{P}}$	$\text{cm}^{-1}$	-79.0	0	-97.9
$\mu_{01}$	$10^{-30}$ Cm	0.196	0.194	0.204
$\mu_{12}$	$10^{-30}$ Cm	0.213	0.214	0.209
$\mu_{23}$	$10^{-30}$ Cm	0.256	0.255	0.255
$\mu_{03}$	$10^{-30}$ Cm	0.001	0.001	0.001
number density	$10^{23}$ m $^{-3}$	3.5	3.0	1.1
linewidth	GHz	1.49	1.36	1.47
$\chi^{(3)}$	$\text{pm}^2/\text{V}^2$	$-0.01 + i 20.56$	$0.04 - i 6.95$	$1.12 - i 4.95$
$ \chi^{(3)} $	$\text{pm}^2/\text{V}^2$	20.6	7.0	5.1
$\Delta k$	$\text{m}^{-1}$	$-0.71 - i 0.05$	$-6.20 + i 0.08$	$-0.34 - i 0.05$
$ J_3 ^2$		0.92	0.80	0.93
$\alpha_{\text{THG}}$	$\text{m}^{-1}$	$10^{-6}$	0.23	$10^{-6}$
$E_{\text{THG}}$	pJ	259.8	21.4	16.1
THG photons		$1.5 \times 10^9$	$1.3 \times 10^8$	$9.5 \times 10^7$

significant resonance enhancement.

Another important aspect of nonlinear frequency conversion is the conservation of momentum, i.e., phasematching (compare Sec. 1.3). For resonance (A) we calculate the wave vector mismatch to  $\Delta k = (-0.71 - i 0.05) \text{m}^{-1}$ . Note, the negative sign of the real part of  $\Delta k$ : According to Fig. 1.2, the process of THG benefits from negative phase mismatch in our focusing geometry, i.e., confocal focusing with  $b \approx L$ . The small imaginary part of  $\Delta k$  corresponds to attenuation coefficients of the third harmonic and fundamental fields. As we assume conversion of ideal Gaussian pulses the absolute square value of the phasematching integral is  $|J_3|^2 = 0.92$ , i.e., of order of magnitude of the peak value of 1.7 in our case (compare Fig. 1.2). Hence, the efficiency of the nonlinear conversion process is not significantly reduced by phase mismatch. For completeness we calculate the absorption coefficient for the third harmonic field, which emerges in the conversion process. As noted above, reabsorption of the THG field is negligible. Finally, we calculate the THG signal pulse energy to  $\approx 260$  pJ. With a fundamental pulse energy of 1.2 mJ this would account for a conversion efficiency of  $\approx 2 \times 10^{-7}$ .

Fig. 3.4 shows a THG spectrum of the two-photon resonance (A) at  $2830.36 \text{cm}^{-1}$  for the isotope  $\text{H}^{35}\text{Cl}$  and the two-photon resonance (C) at  $2830.15 \text{cm}^{-1}$  for the isotope  $\text{H}^{37}\text{Cl}$ . An (unwanted) etalon in the OPA chain induces fluctuations of the fundamental pulse energy. This effects the THG signal pulse energy. Hence, we compensate the THG signal pulse energy according to Eqn. (2.1) with an exponent

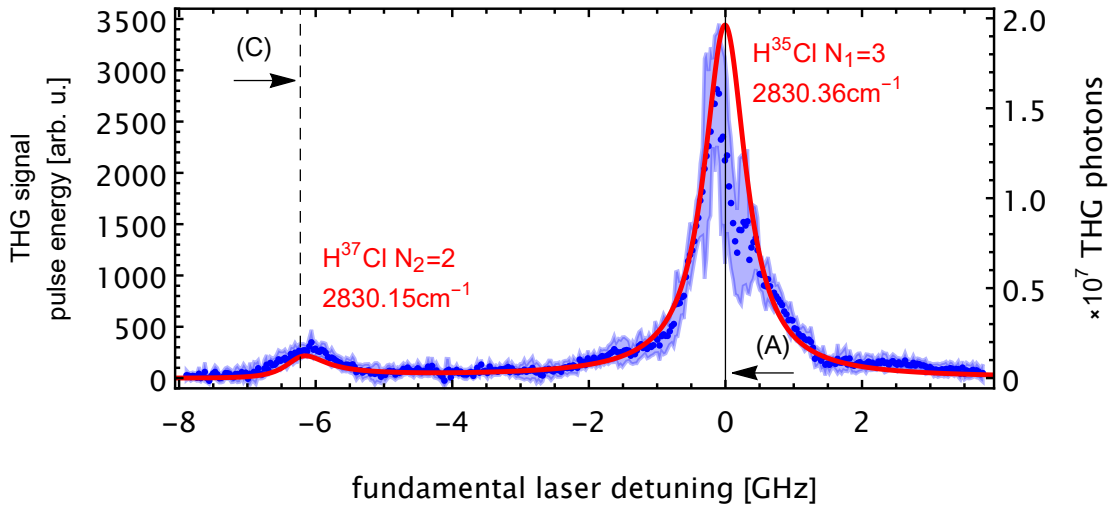


**Figure 3.4:** THG signal pulse energy vs. detuning of the fundamental radiation at the two-photon resonances (A) and (C) at 100 mbar HCl pressure and mean fundamental pulse energy of 1.2 mJ (binned in 30 MHz intervals, the shaded area indicates standard deviations). The right axis gives an estimation for the THG yield based upon the calibration in Sec. 2.5.2. We correct the THG signal pulse energy for fluctuations of the fundamental pulse energy. The red line indicates the scaled simulation result (parameters:  $E_{\text{fund}} = 1.2$  mJ,  $\tau = 8$  ns).

$\epsilon = 2.2$  and a fundamental pulse energy of 1.2 mJ (we discuss the deviation from the expected cubic dependence in Sec. 3.2). Both resonances are visible and distinguishable from the background signal. The fundamental laser detuning between both resonances is only  $\approx 6$  GHz.

Whereas resonance (C) is a Lorentzian shaped spectral line, resonance (A) deviates from the expected Lorentzian spectral line shape. The comparison with the THG simulation confirms this observation: The wings of the spectral line follow the simulation expectation, but for fundamental laser detunings between  $-0.25$  and  $+0.5$  GHz we notice lower THG signal pulse energies than expected. Probably, the THG signal pulse energy drops on two-photon resonance due to saturation of the two-photon transition, which is usually accompanied with changes in the line shape [56]. In addition, Stark shifts might push the resonance to positive detunings in Fig. 3.4 [57]. On the other hand, we performed this specific measurement with neutral density filters to ensure the linearity of the APD signal. It is possible, that the optical density of the filters was not sufficient and the response of the APD saturated slightly at the highest signal levels on the resonance.

For a quantitative discussion of our data we calculate the number of THG photons per pulse (second vertical axis in Fig. 3.4). On resonance (A) we measure  $\approx 10^7$  photons per pulse, i.e., already an considerable amount. Note, that these values are a rough estimation, based upon the calibration of the detector (compare Sec. 2.5.2). From the simulation we would expect 88 times the number of THG photons per pulse, i.e., two orders of magnitude. This is not a huge difference, considering the assumptions, which we had to make in our straightforward simulation. A possible reason is, that the simulation does not include saturation of the two-photon transition at high fundamental intensities (see Sec. 3.2). Furthermore, the intensity profile of

the mid-infrared fundamental radiation deviates from the perfect Gaussian profile, which we assume in the simulation. Due to problems in the calculation of the refractive indices of HCl at the fundamental and third harmonic wavelengths the values for the phase mismatch contain uncertainties. These uncertainties are due to the low resolution of previous studies of the available dispersion data in HCl (see appendix A). The simulation result does not include the fundamental laser linewidth as the collisionally broadened linewidth is larger than the laser linewidth. Finally, the unknown pulse duration and temporal structure of the fundamental pulses influences the THG yield. Nevertheless, our simulation result describes the line shape, linewidth and the relative line intensities well. The constant scale factor has no implication upon the application potential of the method for molecule detection.

### 3.1.2 Three-photon resonance

A few remarks to the two-photon resonance (C) in Fig. 3.4: This two-photon resonance corresponds to the ground state  $(\nu, N_2) = (0, 2)$  of the isotope  $\text{H}^{37}\text{Cl}$  (also compare the left side of Fig. 3.3). Tab. 3.1 summarizes the simulation parameters for this resonance. Detunings, transition dipole moments, linewidth, and the value for  $|J_3|^2$  are comparable to resonance (A). A lower number density and nonlinear susceptibility yields a lower THG signal pulse energy. Note, the large real part of the nonlinear susceptibility. This is due to an assumed nonresonant contribution of the close resonance (A). This appears to be an artefact of our numerical implementation, as the resonance (A) only addresses the ensemble of the isotope  $\text{H}^{35}\text{Cl}$ . The real component introduces an asymmetry of the line shape for resonance (C), which we do not observe in the experimental data. From the THG yields in Tab. 3.1 the THG yield at resonance (C) is  $\approx 6\%$  of the THG yield at resonance (A). From our measurement data we find a ratio of  $\approx 11\%$ , i.e., close to the theoretical expectation.

We now consider the strongest three-photon resonance at a fundamental wave number of  $2807.92\text{ cm}^{-1}$ , labelled (B) in Fig. 3.1. Fig. 3.5 gives the level scheme of the four-level system, which contributes most to the nonlinear susceptibility for THG. It is a resonance for the dominant  $\text{H}^{35}\text{Cl}$  isotope with the ground state  $(\nu, N_1) = (0, 4)$ , i.e., 16.3% of the  $\text{H}^{35}\text{Cl}$  population, and the resonant state  $(\nu, N_1) = (3, 5)$ . This results in a number density of  $3.0 \times 10^{23}\text{ m}^{-3}$  at a HCl pressure of 100 mbar. The detunings to the intermediate states are  $\Delta_{1p} = -9.0\text{ cm}^{-1}$ ,  $\Delta_{2p} = 40.0\text{ cm}^{-1}$  and  $\Delta_{3p} = 0\text{ cm}^{-1}$ . Note, that additional intermediate states in Fig. 3.5 contribute to the frequency conversion process. Like in the two-photon resonant case, collisional broadening dominates the linewidth of 1.36 GHz (FWHM). Tab. 3.1 gives further parameters for calculation of the THG signal pulse energy. In comparison to the two-photon resonance (A) some differences are evident: The nonlinear susceptibility is only  $\approx 33\%$  of the value at resonance (A). Hence, the THG signal intensity is an order of magnitude smaller. The absolute value of the

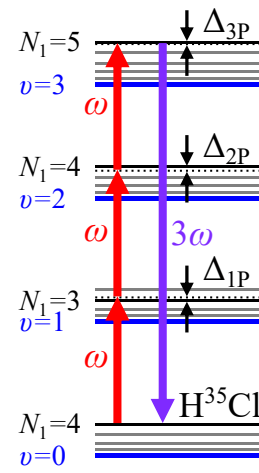


**Figure 3.5:** Level scheme of the three-photon resonance (B) at fundamental wave number  $2807.92\text{ cm}^{-1}$ .

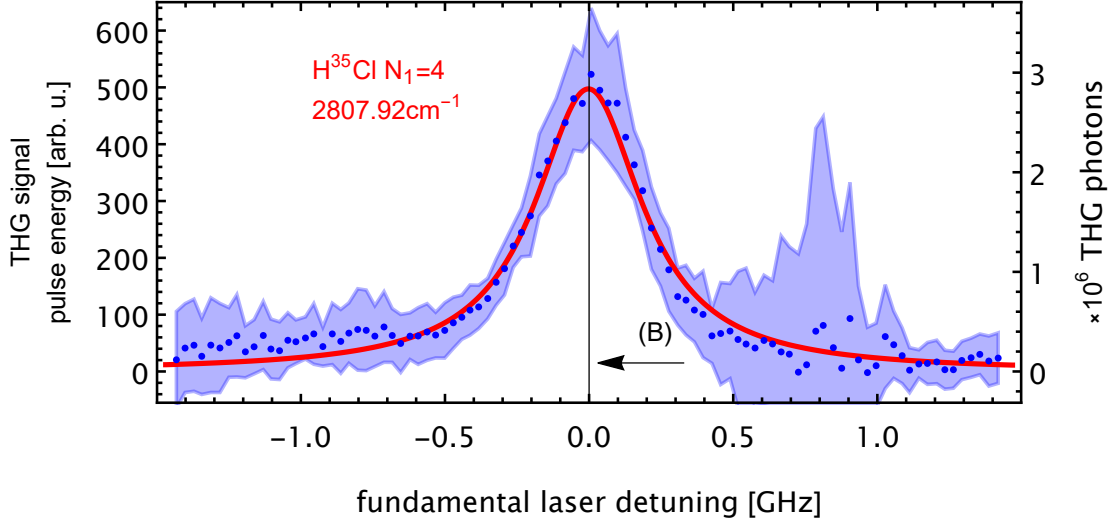


**Figure 3.6:** THG signal pulse energy vs. detuning of the fundamental radiation on the three-photon resonance (B) at 100 mbar HCl pressure and mean fundamental pulse energy of 1.2 mJ (binned in 30 MHz intervals, the shaded area indicates standard deviations). The right axis gives an estimation for the THG yield. We correct the THG signal pulse energy for fluctuations of the fundamental pulse energy. The red line indicates the scaled simulation result (parameters:  $E_{\text{fund}} = 1.2 \text{ mJ}$ ,  $\tau = 8 \text{ ns}$ ).

phase mismatch  $\Delta k$  is larger, but this results only in a slightly lower value for the phasematching integral  $|J_3|^2$ . Finally, the absorption coefficient for THG radiation is significantly larger than on the two-photon resonances, albeit small enough to be still negligible in our case. Assuming a Beer-Lambert law, only  $\approx 1\%$  of the THG wave are reabsorbed over the whole extent of the gas cell ( $L = 5 \text{ cm}$ ).

We measured the THG spectrum at the three-photon resonance (B) under identical experimental conditions (100 mbar, mean fundamental pulse energy 1.2 mJ), as discussed in the previous section for the two-photon resonances. Fig. 3.6 shows the result. On three-photon resonance we find a Lorentzian spectral line shape. Similar to the previous section, we would expect from the simulation 76 times the number of THG photons per pulse. Note, that the factor is  $\approx 16\%$  smaller than in the two-photon resonant case. The difference is probably due to the observed saturation of the two-photon transition on resonance (A). We do not observe this behaviour on resonance (B), due to the large two-photon detuning of  $\Delta_{2p} = 40 \text{ cm}^{-1}$  (compare Fig. 3.5).

## 3.2 Intensity dependence

To confirm the third order of the frequency conversion process, we monitored the variation of the THG signal pulse energy with the peak intensity of the driving fundamental pulses up to  $450 \text{ MW/cm}^2$ . Fig. 3.7 compares the experimental results for the strongest two-photon resonance (A) and the three-photon resonance (B) with the background signal, i.e., off-resonant signal measured with an evacuated gas cell.

From an exponential fit to the data, we find an exponential coefficient of 2.9 for the signal at three-photon resonance (B), which confirms the expected cubic dependence

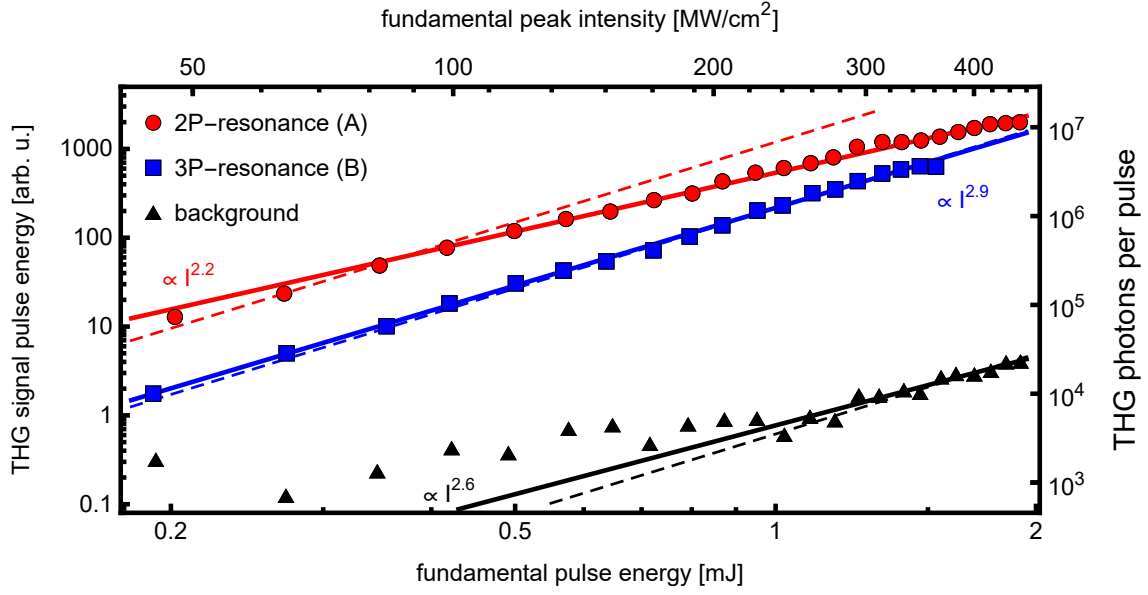


**Figure 3.7:** THG signal pulse energy vs. intensity of the fundamental radiation at two-photon resonance (A) and three-photon resonance (B). The HCl pressure was 100 mbar. In addition, we measured the THG background signal pulse energy in an evacuated gas cell at an off-resonant wave number of  $2829.98 \text{ cm}^{-1}$ . The right axis gives an estimation for the THG yield per pulse. Solid lines depict exponential fits to the experimental data points (for the background signal we considered data points with energies larger than 1 mJ). For comparison, dashed lines indicate fits, that assume a cubic intensity dependence. Note the double logarithmic scale.

of THG upon the driving laser intensity. However, for two-photon resonance (A) we find a significantly lower exponential coefficient of 2.2. This is due to saturation of the involved two-photon transition. From Fig. 3.7 we notice, that our data for the two-photon resonance deviates from the expected cubic law (as indicated by the red dashed line) for intensities beyond  $\approx 100 \text{ MW/cm}^2$  (or a fundamental pulse energy of 0.4 mJ).

To further analyse the impact of the saturation of the two-photon resonance we calculate the two-photon Rabi frequency  $\Omega_{2p}$ , which describes the dynamics of the populations of the states  $\nu = 0$  and  $2$  in the case of two-photon resonant excitation.

The two-photon Rabi frequency is [58]

$$\Omega_{2p} = \frac{\Omega_{01} \Omega_{12}}{2 \Delta_{1p}}, \text{ with } \Omega_{ij} = \frac{\mu_{ij} E_0}{\hbar}, \quad (3.1)$$

with the Rabi frequency for the single-photon transitions  $\Omega_{ij}$  between the states  $i$  and  $j$ , the amplitude of the electric field strength  $E_0$ , which relates to the intensity of the fundamental radiation by  $E_0 = \sqrt{2I/(c_0 \epsilon_0)}$ , and the detuning to the intermediate state  $\Delta_{1p}$ , expressed in units of angular frequency. With an intensity of  $100 \text{ MW/cm}^2$  we calculate a two-photon Rabi-frequency  $\Omega_{2p} \approx 2\pi \times 128 \text{ MHz}$  and a pulse area of  $\Omega_{2p} \times \tau \approx 6.4$ , with the laser pulse duration  $\tau$ . The condition  $\Omega_{2p} \times \tau \gg 1$  indicates the onset of saturation and, hence, explains the observed deviation of the intensity dependence for the THG yield at the two-photon resonance. With a fundamental pulse energy of 2 mJ we get a pulse area of  $\approx 32$ . Saturation of two-photon resonant

THG in an atomic vapor was observed with an almost quadratic dependence on the fundamental intensity [59]. Besides saturation of the two-photon transition, population in the excited state at  $\nu = 2$  might also influence the wave vector mismatch or lead to thermal defocusing of the fundamental radiation. These processes would limit the maximal pulse duration for the fundamental pulses for efficient frequency conversion [56].

Finally, we consider the background signal in Fig. 3.7. Below  $\approx 1$  mJ the data points scatter around a THG signal pulse energy of  $\approx 0.5$  arbitrary units. This signal level is close to the detection limit of our detection setup. For larger fundamental pulse energies the data follows a cubic dependence. Hence, we only consider data points  $> 1$  mJ for an exponential fit of the form  $a x^e$ . The exponent of the best fit is 2.6. A cubic fit also shows good agreement with experimental data at larger fundamental pulse energies. Hence, the background signal originates indeed from a third order nonlinear frequency conversion process. The background signal propagates collinearly with the resonant THG signal in HCl and has the same temporal characteristics. Due to a dispersive element in our detection setup, i.e., the Pellin Broca prism in Fig. 2.16, and high spatial selectivity with apertures in front of the detection setup, the wavelength of the background signal is similar or identical to the wavelength of the resonant THG signal in HCl. Finally, we can exclude nonresonant contributions of HCl, as the background signal persists in an evacuated cell. Hence, the background signal originates from off-resonant THG in the  $\text{CaF}_2$  windows of the gas cell.

In conclusion we observed some saturation of the two-photon resonant THG signal pulse energy at fundamental peak intensities beyond  $100 \text{ MW/cm}^2$ . As we did not notice this behaviour on the three-photon resonance, it might be beneficial to operate at the latter resonance, when applying significantly higher fundamental peak intensities. We further identified the background signal as off-resonant THG from the cell windows.

### 3.3 Pressure dependence of the THG signal

In this section we analyse the dependence of the THG signal on the HCl pressure. An important information with respect to applications is the detection limit of the method, i.e., the lowest pressure or particle density at which we can detect HCl molecules. Hence, we address the detection limit with two approaches: By comparison of THG spectra at low HCl pressures with a reference spectrum in an evacuated cell and via measurements of the peak THG signal pulse energy on a multi-photon resonance at different HCl pressures.

#### 3.3.1 THG spectra at low HCl pressures

Fig. 3.8 (a) shows three THG spectra measured at low HCl pressures of 0.6 and 1 mbar and, for reference, in an evacuated gas cell. Apart from the two-photon resonance (A) at  $2830.36 \text{ cm}^{-1}$  the measured THG signal pulse energy is similar to the reference measurement (compare the standard deviations). The THG background signal pulse energy shows an oscillation, which correlates with fluctuations of the fundamental pulse energy due to an (unwanted) etalon in the OPA chain (see Sec.

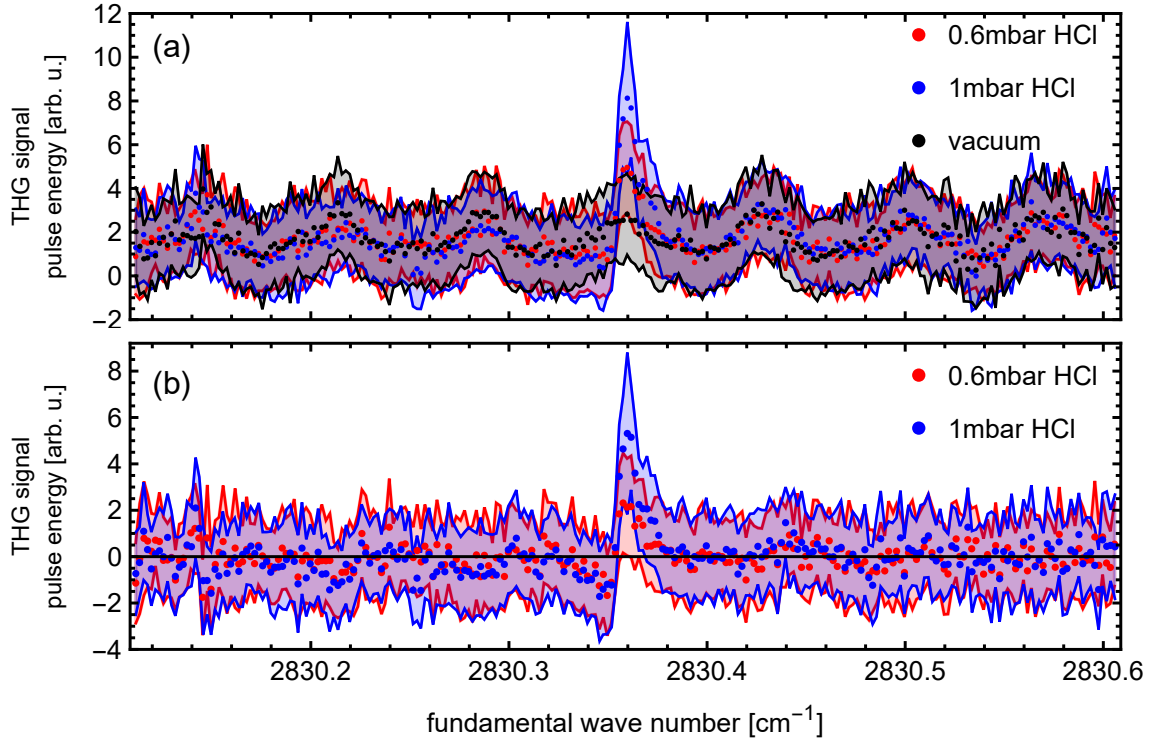


**Figure 3.8:** THG signal pulse energy vs. fundamental wave number at resonance (A) for (a) HCl pressures of 1, 0.6 and 0 mbar (evacuated cell). (b) Data points from THG spectra at 1 and 0.6 mbar with subtraction of the spectrum measured in the evacuated cell. The fundamental pulse energy was 1 mJ. The shaded area indicates standard deviations from binning the raw data in intervals of  $0.001 \text{ cm}^{-1}$ .

2.1.2). To remove this oscillation we subtract the reference measurement from THG data. The result in Fig. 3.8 (b) shows, that the off-resonant THG signal is effectively zero. We observe the two-photon resonance at  $2830.36 \text{ cm}^{-1}$  at both low HCl pressures. The amplitude of the THG signal pulse energy is  $\approx 5$  arbitrary units. We define the signal-to-noise ratio as the signal amplitude, divided by the standard deviation of the THG signal pulse energy. Therefore, we have a signal-to-noise ratio of  $\approx 1$ . The subtraction of the reference measurement does not significantly improve the signal-to-noise ratio. Hence, the detection limit is  $\leq 1 \text{ mbar}$ .

We now consider the spectral line profiles on the resonances (A) and (B) in more detail. Fig. 3.9 shows data measured at a HCl pressure of  $\approx 1 \text{ mbar}$ . We added the mean value of the THG-background signal to the data points with subtracted reference spectrum. Obviously, the spectral line shapes are asymmetric and quite different from a Gaussian profile expected for a nearly only Doppler-broadened spectral line (compare Sec. 3.4.1). Such asymmetric, Fano-type resonances are known from other types of nonlinear spectroscopy [60]. In our case they are due to interference between the resonant THG signal from HCl and the THG background signal from the cell windows.

As we have seen above we cannot increase the detection limit significantly by subtraction of the THG background. Murdoch *et al.* further argue, that the interference has to be considered in the analysis of asymmetrical line profiles [60]. Therefore, we

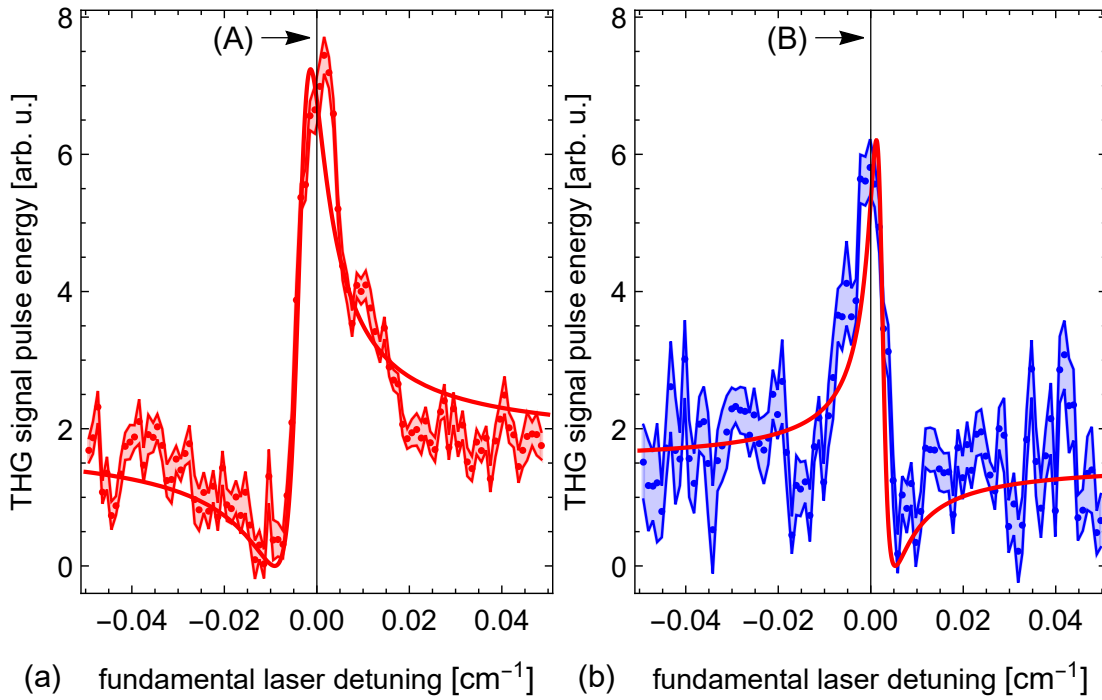


**Figure 3.9:** THG signal pulse energy vs. fundamental laser detuning at a low HCl pressure of 1 mbar and fundamental laser pulse energy of 1 mJ. Spectral line shapes of (a) two-photon resonance (A) and (b) three-photon resonance (B). Points indicate experimental data, solid lines show fits of a Fano line shape, shaded areas depict standard errors from binning the raw data in frequency intervals of  $0.001 \text{ cm}^{-1}$ .

perform Fano-type fits to the data using the model [61]

$$f(\Delta) \sim \frac{(q + 2\Delta/\Gamma)^2}{4\Delta^2/\Gamma^2 + 1}, \quad (3.2)$$

with the detuning  $\Delta$ , a linewidth factor  $\Gamma$ , and the Fano parameter  $q$ . We show the results of the fits in Fig. 3.9. For resonance (A) we get  $q = 1.7$  and for resonance (B)  $q = -1.8$ . The negative sign indicates the different relative phase between resonant and background THG signal. When compared with part (a) the line shape is flipped with regard to the line center. The absolute value of the Fano parameter indicates the asymmetry of the spectral line profile ( $q = 1$ : equal contributions from resonant and background THG signal). In a very rough estimation, the value  $|q|^2$  determines the ratio of the resonant and background THG signal. Hence, the fit values for the Fano parameter mirror the observed signal-to-background ratios of 3 – 4 for both spectral lines (A,B) at a HCl pressure of 1 mbar, i.e., close to the detection limit of our setup.

In the limit  $|q| \rightarrow \infty$ , the Fano line profile is well approximated by a Lorentzian. The Fano line profile has to be convoluted with the Gaussian of the Doppler broadened line profile. Hence, if the background THG signal is negligible compared to the resonant THG signal we would expect a near-Gaussian spectral line profile. We observe the asymmetric spectral line profile only at low HCl pressures below  $< 5$  mbar. With increasing pressure, it evolves into a symmetric line shape, as the resonant THG signal becomes much larger compared to the THG background signal.

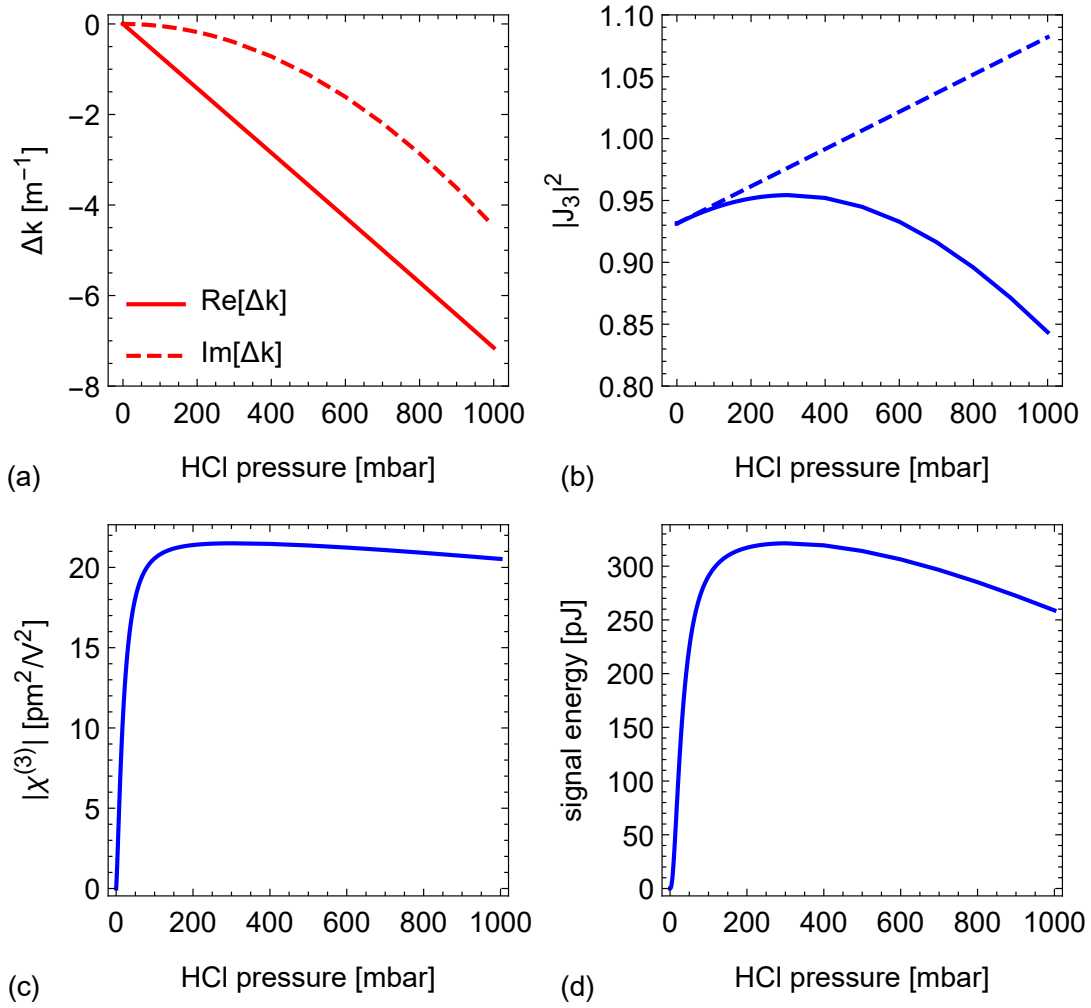


**Figure 3.10:** (a) Complex Wave vector mismatch vs. HCl pressure on the two-photon resonance (A) at fundamental wave number  $2830.36 \text{ cm}^{-1}$ . (b) Corresponding absolute square value of the phasematching integral  $J_3$  vs. HCl pressure. For comparison, the blue dashed line indicates the values for  $|J_3|^2$  without the imaginary part of  $\Delta k$ . (c) Absolute value of the nonlinear susceptibility  $\chi^{(3)}$  vs. HCl pressure. (d) THG pulse energy vs. HCl pressure. Simulation parameters: fundamental wave number  $2830.36 \text{ cm}^{-1}$ ,  $b = 6 \text{ cm}$ ,  $L = 5 \text{ cm}$  and  $z_0 = 3.65 \text{ cm}$ .

### 3.3.2 THG simulation

We consider the numerical simulation for THG in more detail. Fig. 3.10 (a) gives the real and imaginary part of the wave vector mismatch on the two-photon resonance (A) vs. HCl pressure. The real part of  $\Delta k$  is negative and increases linearly in absolute value with larger HCl pressures. The absolute value of the imaginary part of  $\Delta k$  also increases with HCl pressure. This is due to collisional broadening of spectrally close single-photon resonances, i.e., absorption lines (compare Sec. 3.4.1). Even at a HCl pressure of 1 bar, the value for the scalar phase mismatch is only  $b\Delta k \approx -0.4$ . Hence, if we want to detect HCl molecules at low absolute pressures, we have to optimize the THG process for  $b\Delta k \approx 0$ . In this case, confocal focusing is the optimal solution, according to Fig. 1.2.

Fig. 3.10 (b) shows the variation of the absolute square value of the phase matching

integral  $J_3$  vs. HCl pressure for our experimental situation, i.e., close to confocal focusing with  $b \approx L$  (compare Sec. 2.4). Up to a HCl pressure of 250 mbar the values for  $|J_3|^2$  increase, for higher HCl pressures we notice lower values. This is due to absorption of the fundamental wave. For comparison, the dashed line in Fig. 3.10 (b) indicates the result for  $|J_3|^2$  without the imaginary part of  $\Delta k$ . Note, that this variation is only  $\approx 10\%$  of the value for  $|J_3|^2$  at a HCl pressure of 0 mbar. Hence, we can assume, that phase matching should not limit the THG yield in our THG investigations.

According to Eqn. (1.11), the nonlinear susceptibility  $\chi^{(3)}$  has two individual dependencies on the HCl pressure  $p$ . Firstly, the number density  $\rho$  depends linearly on the pressure through the ideal gas equation  $\rho \sim p$ . Secondly, the dephasing rates  $\gamma_{ij} \sim p$  are subject to collisional broadening (see Sec. 3.12). Hence, the linear proportionalities cancel out at a specific pressure. The simulation result in Fig. 3.10 (c) confirms this behaviour. Beyond a HCl pressure of 200 mbar,  $\chi^{(3)}$  stays constant in good approximation. Fig. 3.10 (d) gives the result for the signal pulse energy. Hence, we expect peak THG signals at  $\approx 250$  mbar and lower signals for higher HCl pressures. The phasematching integral  $J_3$  only has a marginal influence upon the THG signal.

### 3.3.3 Pressure dependence

Fig. 3.11 shows the variation of the THG signal pulse energy at the resonances (A) and (B) with HCl pressure. We also add the peak THG signal pulse energies, derived from Lorentzian fits to THG spectra at resonances (A,B,C) with constant HCl pressures.

Under conditions of perfect phase matching, we would expect the signal intensity to grow quadratically with the number density or HCl pressure. The pressure dependence at resonance (B) confirms this expectation for HCl pressures below a few 10 mbar. Here, our simulation result (blue, dot-dashed line) describes the experimental data well. The two-photon resonance (A) shows some deviation from the quadratic dependence, an exponential fit to the measurement data (below 50 mbar) yields an exponent of  $\approx 1.4$  rather than 2. This deviation is also visible in comparison with the simulation result (red, solid line).

For larger pressures above 50–100 mbar the THG yield does not grow anymore with increasing pressure, but remains on an (almost) constant level for all multi-photon resonances (A,B,C). This is due to collisional self-broadening. The resonant THG yield is proportional to  $\sim \rho^2 |J_3(p)|^2 / \gamma^2$  (see Eqn. (1.8)). If collisional broadening is larger than the Doppler linewidth of the resonance, the resulting linewidth of the resonance linearly depends on the HCl pressure:  $\gamma \sim p$  (compare Sec. 3.4.1). Hence, assuming an ideal gas ( $\rho \propto p$ ) the pressure dependence of the THG signal cancels at pressures  $\gtrsim 100$  mbar. The phasematching integral  $J_3(p)$  does only have a weak pressure dependence and is constant in good approximation, due to the weak focusing conditions in our experimental setup. The simulation incorporates collisional self-broadening, hence, we find good agreement on resonance (A) for larger HCl pressures. In case of resonance (B) we observe an almost constant THG signal pulse energy at HCl pressures  $\geq 100$  mbar, whereas the simulation expects a slow growth. On resonance (C) we find a good agreement between data and the

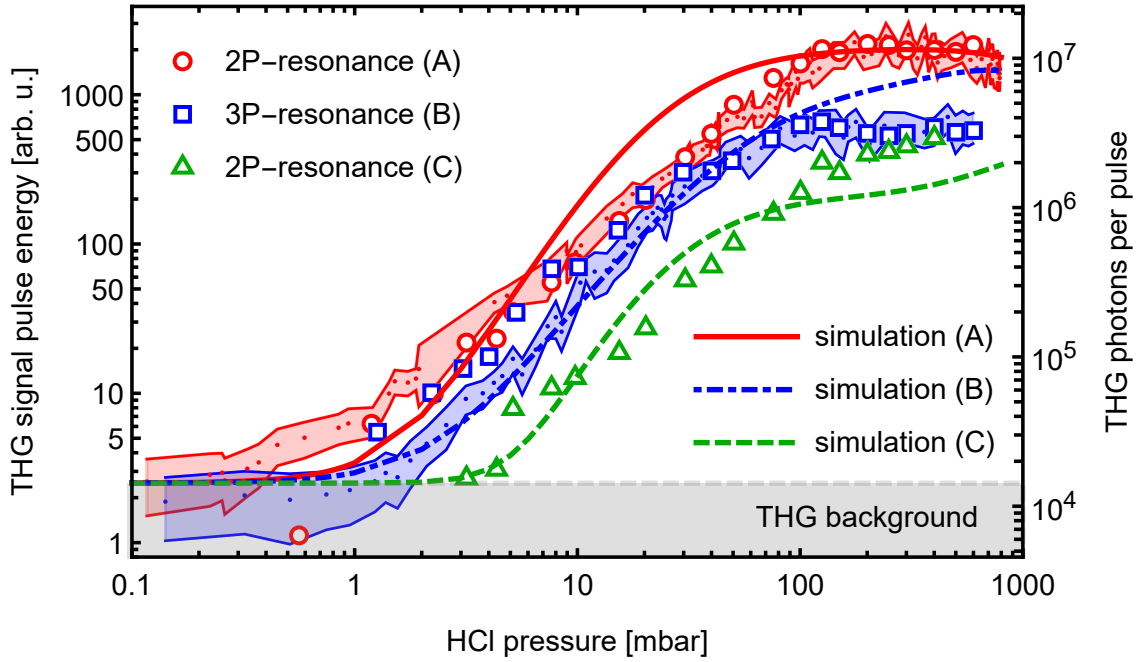


**Figure 3.11:** THG signal pulse energy vs. HCl pressure at the dominant two-photon resonance (A) or three-photon resonance (B). We also added a measurement series for larger pressures at a weaker two-photon resonance (C). The fundamental pulse energy was 1.2 mJ. We correct the THG signal pulse energy for fluctuations of the fundamental pulse energy. Symbols indicate experimental data. The experimental data consists of measurements at fixed resonance positions (indicated by shaded areas) and data points, which we determined from the peak value of a Lorentzian fit to the spectral line at fixed HCl pressures (indicated by hollow symbols). Lines depict simulation fits to the data of all resonances with an offset of 2.5 arbitrary units and linear normalization factors: (A)  $6 \times 10^{-3}$ , (B)  $1 \times 10^{-2}$  and (C)  $2 \times 10^{-2}$  (parameters:  $E_{\text{fund}} = 1.2$  mJ,  $b = 6$  cm,  $L = 5$  cm and  $z_0 = 3.65$  cm). The right axis gives an estimation on the measured number of THG photons per pulse. Note the double logarithmic scale.

simulation result.

Especially on the two-photon resonance (A) we detect THG signals above the THG background down to HCl pressures of  $\approx 0.1$  mbar. However, in this case we already operate at the detection limit of the APD to resolve the difference between resonant and background THG signal pulse energy. Furthermore, the pressure sensor, which we applied in this measurement series only gives reliable pressure readings for absolute pressures larger than  $\approx 1$  mbar (compare appendix B). We find a conservative detection limit for the THG approach in our setup in the range  $\leq 1$  mbar, where the THG signal pulse energy is clearly separable from the THG background signal. The value is the same region as the detection limit, which we derived from signal-to-background ratios of the THG spectrum at low HCl pressures.

### 3.3.4 Discussion of the detection limit

Both approaches yield a detection limit of a HCl pressure  $\leq 1$  mbar. In our current focusing setup (compare Sec. 2.4) a pressure of 1 mbar corresponds to roughly  $3 \times 10^{13}$  HCl molecules in the confocal volume of the fundamental radiation, constrained

by the cell windows. We take into account, that the fundamental radiation is in two-photon resonance only with a fraction of the HCl molecules, i.e., the isotope  $\text{H}^{35}\text{Cl}$  in the rotational ground state  $N_1 = 3$ . Hence, the molecule number corresponds to a particle density of  $\approx 10^{15}$  molecules/cm<sup>3</sup>.

A fair comparison of the obtained detection limit to other nonlinear spectroscopy methods is no simple task, as not only the nonlinear susceptibility of the sample, but also the specific conditions of the laser and detection setup are relevant. We restrict our analysis to CARS and degenerate four-wave mixing (DFWM). Typically, detection limits of 0.1 to 1 mbar are obtained for CARS detection of diatomic molecules in combustions, when suppressing the nonresonant CARS background [5, 62]. In an experiment on detection of HCl molecules by degenerate four-wave mixing (DFWM), driven by mid-infrared (ns) laser pulses with pulse energies up to 2 mJ, and a similar intensity of the fundamental radiation in the interaction region as in our setup, Sun *et al.* achieved a detection limit of  $6.8 \times 10^{14}$  molecules/cm<sup>3</sup> [63]. Note, that even lower detection limits were reported in the literature for the detection of HCl molecules with DFWM [1].

Hence, the detection limit, which we obtained for resonantly enhanced THG will already permit realistic applications for trace gas analytics. We must not fail to mention, that our measurements were performed in a gas cell with pure HCl, i.e., without any background gas - which would be present under typical conditions of trace gas analytics. Collisional broadening induced by the background gas would increase the dephasing rate in Eqn. (1.10) and reduce the obtained resonance enhancement for THG (we discuss this problem in more detail below). Moreover, phase matching in the background gas will vary (increase or decrease) the THG yield.

Note, that linear techniques, e.g., absorption spectroscopy, offer lower detection limits [64]. However, long interaction lengths are necessary in realistic implementations, e.g., in multi-pass setups [65]. Hence, absorption spectroscopy does not provide large spatial resolution in propagation direction, which is desirable, e.g., in combustion environments. Note, that in such environments background signals and absorption or scattering of fundamental radiation, due to soot particle make a quantitative analysis difficult [66]. Here, nonlinear spectroscopy methods offer higher spatial resolution, time resolution, thermometry [67] and higher robustness in "sooty environments" [68].

However, there are still means to further improve the detection limit in order to compensate for the effects of background gas: In our setup, a THG background signal from the windows of our gas cell, which we confirmed to remain also in an evacuated gas cell, limited the detection limit. The windows are not required in the confocal volume in setups, which implement laminar gas flows or flames. This would enable us to approach a detection limit, determined only by the quantum efficiency of the detection setup. Moreover, higher fundamental laser pulse energy and larger laser bandwidth (matched to the larger, collisionally broadened spectral linewidth) would further improve the detection limit.

## 3.4 Collisional broadening and shifts

We analyse the processes of self- and foreign-gas collisional broadening as well as self-induced shifts of the resonance position. First, we discuss the line broadening mechanisms in molecules, which we consider for the simulation, in more detail.

### 3.4.1 Line broadening mechanisms

The dephasing rates  $\gamma_{ij}$  in Eqn. (1.10) depend on molecular parameters and the environment. In general the dephasing rate  $\gamma_{ij}$  with  $j > i$  is [8]

$$\gamma_{ij} = \frac{1}{2} (\Gamma_i + \Gamma_j) + \gamma_{ij}^{(\text{col})}, \quad (3.3)$$

with the decay rates  $\Gamma_i$  of populations in the state  $i$  and the decay rate attributed to collisions  $\gamma_{ij}^{(\text{col})}$ . If the state  $i$  is the ground state, as it is the case in Eqn. (1.10), the corresponding decay rate is zero. When there only exists a single decay path from state  $j$ ,  $\Gamma_j$  is equal to the Einstein A coefficient of the transition path. Therefore, this contribution to the linewidth is of Lorentzian shape and defines the natural linewidth. Collisions decrease the mean life time of population in the excited state, i.e., increase the width of the Lorentzian line. Furthermore, during collisions neighboring particles stochastically vary the Coulomb potential of an emitting particle. The quantity  $\gamma_{ij}^{(\text{col})}$  depends on the specific transition between the states  $j$  and  $i$ , the pressure of the molecular species and a broadening coefficient, which also depends on the temperature. Foreign gas present in the sample volume will induce collisions with the sample molecules. A simple model for the collisional component of Eqn. (3.3) rate is

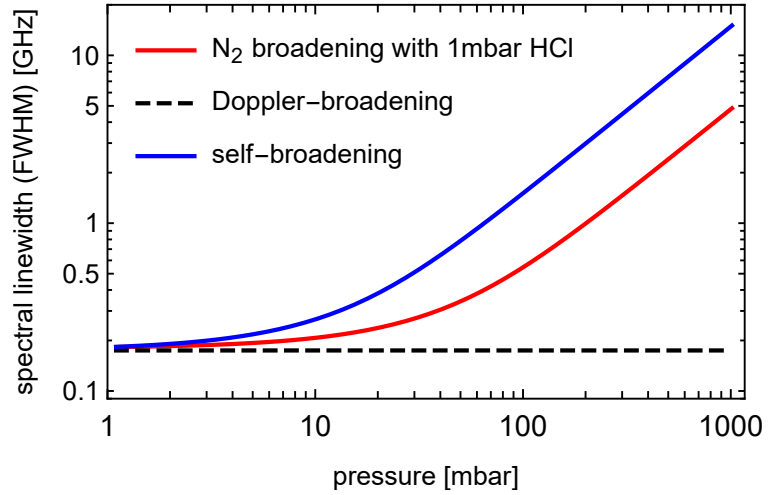
$$\gamma_{ij}^{(\text{col})}(p, T) = \left( \frac{T_{\text{ref}}}{T} \right)^{n_{\text{air}}} \left[ \gamma_{ij}^{(\text{self})} \frac{p_{\text{self}}}{p_{\text{ref}}} + \sum_k \gamma_{ij}^{(k)} \frac{p_k}{p_{\text{ref}}} \right], \quad (3.4)$$

with  $k$  indicating contributions from different foreign gases, total pressure  $p = p_{\text{self}} + \sum_k p_k$  and reference conditions  $T_{\text{ref}} = 295 \text{ K}$  and  $p_{\text{ref}} = 1013 \text{ mbar}$ . Note, that  $\gamma_{ij}^{(\text{col})}$  is the half-width at half-maximum (HWHM) of a Lorentzian profile. The coefficient  $n_{\text{air}}$  is the exponent of the temperature scaling of the dephasing rate, which depends on the molecule, which engages in collisions. As the HITRAN database does not list the parameters  $n_{\text{HCl}}$  and  $n_{\text{N}_2}$ , we approximate the exponent of temperature scaling with the values for air-induced broadening  $n_{\text{air}}$ . Note, that this value also depends on the rotational state of the molecular ground states. A typical value is  $n_{\text{air}} = 0.73$  for the fundamental absorption band in  $\text{H}^{35}\text{Cl}$  [69]. For a detailed assessment on the broadening parameters in HCl compare [70].

Besides these homogeneous broadening factors we also have to consider inhomogeneous line broadening processes, i.e., Doppler broadening. The Doppler-broadened line shape is a Gaussian. The FWHM of the Gaussian function is

$$\alpha_{\text{Doppler}} = \frac{\tilde{\nu}}{c_0} \sqrt{\frac{8 \ln(2) N_A k_B T}{M}}, \quad (3.5)$$

**Figure 3.12:** Spectral linewidth (given as FWHM of the Voigt line profile) vs. pressure for a HCl absorption line at  $2821.57 \text{ cm}^{-1}$ . The red line indicates the foreign-broadened linewidth vs. nitrogen pressure, added to 1 mbar of HCl. A blue line shows the self-broadened linewidth vs. HCl pressure. Broadening parameters from [70, 72, 75].



with the transition wave number  $\tilde{\nu}$ , Avogadro constant  $N_A$ , Boltzmann constant  $k_B$ , the molar mass of the molecule  $M$  and the temperature of the sample  $T$ .

From the Gaussian component of Doppler broadening  $\alpha_{\text{Doppler}}$  and the Lorentzian component of collisional broadening  $\alpha_{\text{coll}} = 2\gamma_{ij}^{(\text{col})}$  we calculate the FWHM of a Voigt distribution with the empirical expression [71]

$$\alpha_{\text{Voigt}} \approx 0.5346 \alpha_{\text{coll}} + \sqrt{0.2166 \alpha_{\text{coll}}^2 + \alpha_{\text{Doppler}}^2}. \quad (3.6)$$

Here, we neglect the natural linewidth, which is a good approximation, as even at vacuum conditions, the Doppler broadened linewidth is orders of magnitude larger than the natural linewidth in HCl. Note, that there are reports on deviations from Voigt line shapes [72]. This is due to collisional (Dicke) narrowing processes, that occur due to the impact of the velocity change of molecules during collisions upon the Doppler shift [72, 73]. This effect mainly occurs at low pressures and results in a narrowing of the Doppler broadening process, i.e., larger linewidths. Foreign gas could also induce this process. Therefore, explicit investigations of different gas mixtures are necessary. For an example of Dicke narrowing in HCl, perturbed by argon see [74].

Fig. 3.12 compares the pressure dependence of the different broadening mechanisms. Apart from the narrowing effects discussed above, Doppler-broadening is independent of the gas pressure. We notice, that self-broadening in the case of HCl is almost twice as strong as foreign-gas broadening of 1 mbar HCl and variable  $N_2$  pressure.

We include both relevant broadening mechanisms in our simulation to describe the transition between the low pressure region, where Doppler-broadening dominates and higher pressures, where collisional broadening is more present. We neglect effects of Dicke narrowing. We calculate the FWHM of the Voigt line from Eqn. (3.6), taking into account collisional broadening as the Lorentzian component and Doppler broadening as the Gaussian component. We assume this linewidth to be the dephasing rate in Eqn. (1.10). Note, that this approximation results in a Lorentzian line shape also when collisional broadening is negligible. But as we are mostly interested in simulation results at pressures, where collisional broadening dominates,

this deviation is negligible. A more rigorous approach to this situation would be the convolution of the Lorentzian of the collisionally broadened line with a Doppler broadened Gaussian line shape. Note, that we have to account for both abundant HCl isotopes. An additional influence which increases the linewidth of the measured THG resonance is the linewidth of the fundamental laser radiation. To include the laser linewidth in our simulation we would have to convolute the simulation result with the spectrum of the fundamental laser radiation.

### 3.4.2 Self-broadening of two- and three-photon resonances

We discuss now the impact of HCl pressure on the spectral linewidth of the THG signal pulse energy as well as on the frequency position of the resonance in more detail. Fig. 3.13 shows the variation of the THG signal pulse energy with both driving laser wave number and HCl pressure for the relevant multi-photon resonances. The data is a fraction of the two-dimensional data set, which we already discussed in Fig. 3.11. We apply a nonlinear color scale to highlight the difference between fluctuations in the THG background signal pulse energy and the weak resonant THG signal pulse energies at low HCl pressures. The three-photon resonance (B) broadens significantly in the displayed HCl pressure range. This is due to self-induced collisions. The experimental data is in good agreement with our simulation result, compare Fig. 3.13 (b). We notice some deviations on the right wing of resonance (B) at higher HCl pressures. This appears to be an artifact of the compensation of the THG signal pulse energy for fluctuations of the fundamental pulse energy (more than  $\pm 50\%$  of the mean fundamental pulse energy of 1.2 mJ, compare Sec. 2.1.2). The two-photon resonances (C) and (A), shown in Fig. 3.13 (c), are also clearly distinguishable from fluctuations of the background signal. Note, that the contribution of both common isotopes of HCl are separately observable in the shown HCl pressure range between 0 – 100 mbar. For higher HCl pressures (not shown in the figure) the resonances (A) and (C) overlap, due to collisional broadening. Again, we find a good agreement with the simulation result in Fig. 3.13 (d).

To verify our model for the line broadening mechanisms, we discuss the dependence of the spectral linewidth of the multi-photon resonances in some more detail. Fig. 3.14 gives the spectral linewidths derived from Lorentzian fits, which we applied to the resonances (A) and (B). The experimental data shows the expected linear dependence on the HCl pressure. Especially, the three-photon resonance is well-described by the linear fit and our theory prediction. We notice some variations at the two-photon resonance (A) for HCl pressures below 20 mbar, when we compare the data with linear fits (solid lines in Fig. 3.14). In this case the offset of the fit is larger, than the expected Doppler-broadened linewidth, which we convoluted with the laser linewidth according to  $\sqrt{3\Delta f_{\text{fund}}^2 + \Delta f_{\text{Doppler}}^2}$ . There are two possible explanations for this deviation: As we have seen in Sec. 3.2, we observe significant saturation of the two-photon transition on resonance (A). This might lead to power broadening, as the two-photon Rabi frequency, according to Eqn. (3.1), is  $\approx 2\pi \times 384$  MHz at a fundamental pulse energy of 1.2 mJ. The spectral linewidth (given as FWHM) broadens linearly with the Rabi frequency [76]. Hence, power broadening could explain the offset of  $\approx 450$  MHz between the fit and the Doppler linewidth for resonance (A) in Fig. 3.14. Another possibility is Dicke narrowing, which we do not

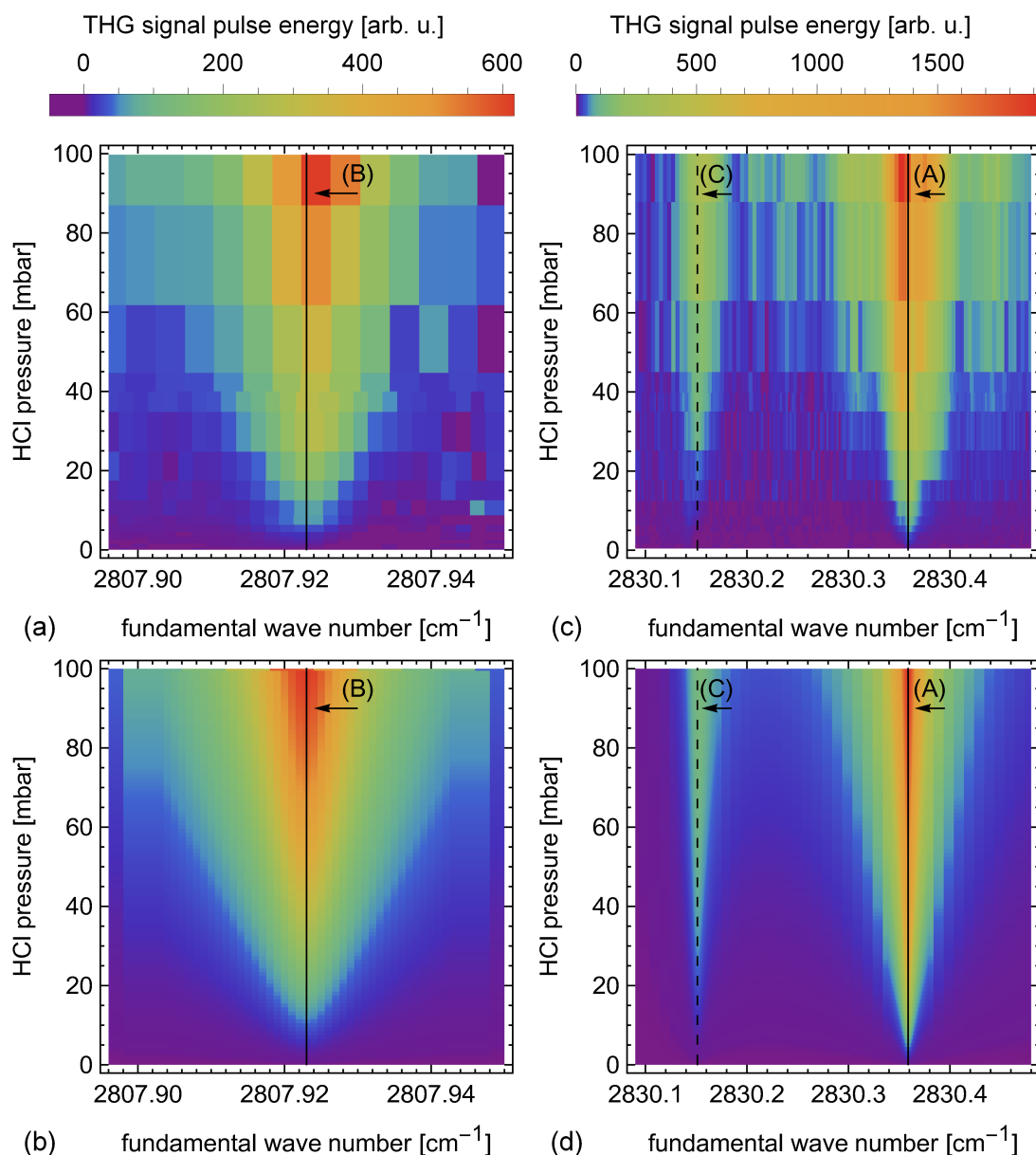


**Figure 3.13:** THG signal pulse energy vs. HCl pressure and fundamental wave number at selected multi-photon resonances. (a) Three-photon resonance (B). (b) Numerical simulation for resonance (B). We normalized the simulation result to the experimental data. (c) Two-photon resonances (C) and (A). (d) Numerical simulation for the resonances (C) and (A). Black vertical lines indicate the expected spectral positions of the multi-photon resonances (solid line for  $H^{35}Cl$ , dashed line for  $H^{37}Cl$ ). The fundamental pulse energy was 1.2 mJ. We correct the THG signal pulse energy for fluctuations of the fundamental pulse energy. Note the different color scales. For better comparison, we normalized the simulation result to the peak THG signal pulse energy in the experimental data.

account for in our simulation. Dicke narrowing leads to larger spectral linewidths, especially at low pressures (compare Sec. 3.12). Values at HCl pressures below 5 mbar are also subject to asymmetric line shapes due to the interference with the background signal. This leads to increased errors for the determination of the spectral linewidth from Lorentzian fits.

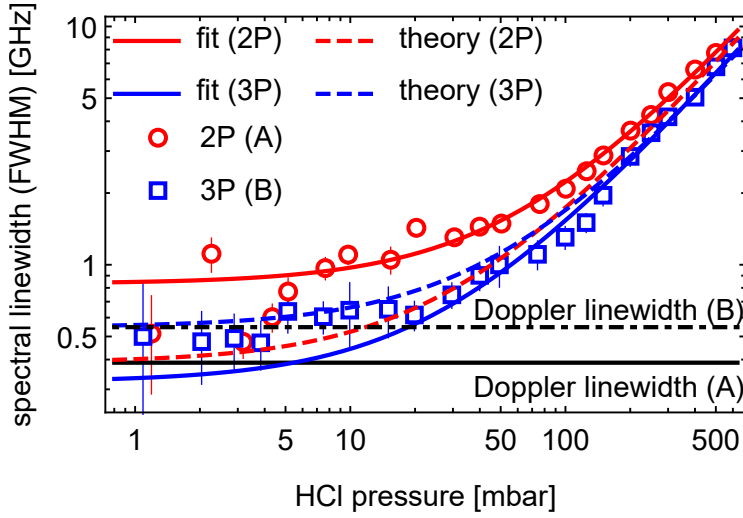


**Figure 3.14:** Spectral linewidths (given as FWHM) of the two-photon resonance (A) at  $2830.36\text{ cm}^{-1}$  and the three-photon resonance (B) at  $2807.92\text{ cm}^{-1}$  vs. HCl pressure. The fundamental pulse energy was 1.2 mJ. The horizontal lines indicate the Doppler-broadened linewidths, convoluted with the laser linewidth. Solid lines give linear fits, dashed lines the theory expectation. Note the double logarithmic scale.

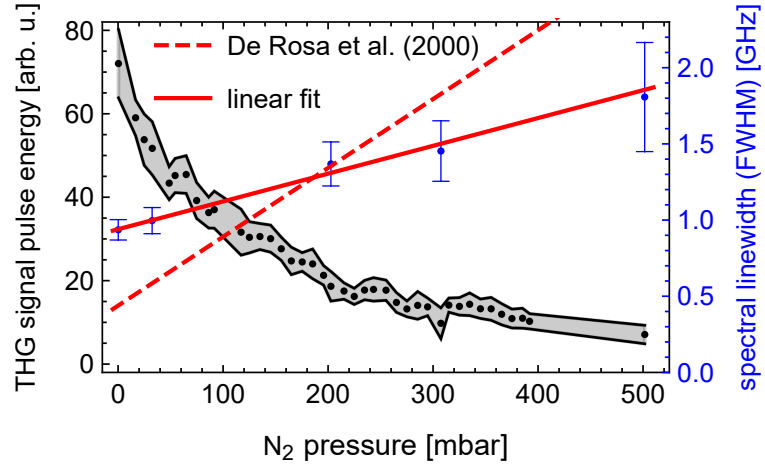
Apart from the differences in the offset of the linewidth on resonance (A), we find good agreement of the experimental data with linear fits and our simulation results for larger HCl pressures. From the fit result for resonance (A) we calculate a self-broadening coefficient of  $\gamma_{\text{self}}^{(2\text{P})} = 0.233\text{ cm}^{-1}/\text{bar}$ . Note, that the self-broadening coefficient is usually defined as half of the linewidth at half maximum (HWHM). The result for resonance (B) is  $\gamma_{\text{self}}^{(3\text{P})} = 0.202\text{ cm}^{-1}/\text{bar}$ . These values are very close to the simulation expectation of  $\gamma_{\text{self}}^{(2\text{P})}(\text{simulation}) = 0.225\text{ cm}^{-1}/\text{bar}$  and  $\gamma_{\text{self}}^{(3\text{P})}(\text{simulation}) = 0.192\text{ cm}^{-1}/\text{bar}$ . We conclude, that our simple model for the line broadening is sufficient to describe THG at larger HCl pressures. Note, that we will discuss the spectral linewidth of the two-photon resonance (A) in more detail in Sec. 4.6.

### 3.4.3 Foreign-gas broadening

Finally, we address foreign-gas broadening. In our setup, we can analyse foreign-gas induced collisional broadening of the molecular resonances of HCl by addition of nitrogen to a fixed HCl pressure in the gas cell. Fig. 3.15 gives the result of a test measurement with  $\approx 7\text{ mbar}$  HCl and up to 500 mbar  $\text{N}_2$  at the two-photon resonance (A). Obviously, the THG signal pulse energy drops immediately, as collisions with nitrogen molecules broaden the two-photon resonance with respect to the narrow laser linewidth. In contrast to the case of a pure HCl environment, here, the number density of HCl stays constant. Therefore, the THG signal pulse energy follows a  $\propto 1/p^2$  dependence, as the linewidth is linearly proportional to the  $\text{N}_2$  pressure. We plot the spectral linewidths, which we determined from Lorentzian fits to THG spectra of resonance (A) at fixed  $\text{N}_2$  pressures.

We find a linear dependence of the spectral linewidth upon the  $\text{N}_2$  pressure and calculate a foreign-gas induced broadening coefficient of  $\gamma_{\text{N}_2} = 0.06\text{ cm}^{-1}/\text{bar}$ . We compare this result with literature values, as the HITRAN database currently does not list broadening parameters for  $\text{N}_2$ . De Rosa *et al.* measured self- and foreign-gas induced broadening parameters for the first overtone transitions in HCl [77]. As

**Figure 3.15:** THG signal pulse energy (black points) and spectral linewidth (blue points, right axis) vs.  $N_2$  pressure. The HCl pressure was  $\approx 7$  mbar and the fundamental pulse energy was 1.4 mJ. The red line gives a linear fit and the dashed red line shows the literature expectation [77]. The shaded area and error bars indicate standard deviations.



the single-photon transition corresponding to resonance (A) is dipole forbidden we calculate the mean of the coefficients for the transitions  $(2, 4) \rightarrow (0, 3)$  and  $(2, 3) \rightarrow (0, 4)$ . The resulting broadening coefficients are  $\gamma_{\text{self}} = 0.225 \text{ cm}^{-1}/\text{bar}$  and  $\gamma_{N_2} = 0.075 \text{ cm}^{-1}/\text{bar}$ . The self-induced broadening coefficient is in equal to the simulation result for resonance (A) and fits with our measurement in Sec. 3.4.2. Our result for  $\gamma_{N_2}$  is significantly smaller than the literature value. To demonstrate this, we added a theory curve, according to Eqn. (3.4), to Fig. 3.15. The slope of the theory curve does not describe the experimental data and the linewidth offset is almost half of the measured value. Note, that we observe the largest observations from the simulation results in Fig. 3.14 for resonance (A) at pressures around 7 mbar. Further systematic studies on  $N_2$  induced collisional broadening are necessary to resolve the large deviation of the broadening coefficient  $\gamma_{N_2}$  from the literature value.

The influence of collisional broadening due to foreign gas is relevant for the application of our method in trace gas analysis, i.e., the detection of small partial HCl pressures at ambient pressures (e.g., for leakage detection in an industrial environment). The  $\propto 1/p^2$  dependence observed in Fig. 3.15 could limit the applicability of resonantly enhanced THG in such an environment. On the other hand, the larger spectral linewidth might allow larger bandwidths for the fundamental radiation. Hence, we could gain from the cubic dependence of the THG yield upon the peak intensity of the fundamental field through temporally shorter laser pulses as  $P_{\text{fund}} \propto \tau^{-1} \propto \Delta f_{\text{fund}}$ .

### 3.4.4 Pressure-induced shifts

Besides broadening of the linewidth of the multi-photon resonance we also observe self-induced shifts of the resonance position. Fig. 3.16 gives an overview on the three multi-photon resonances (A,B,C). We observe different behaviours for the peak position upon HCl pressure. The three-photon resonance (B) shifts to positive detunings up to 200 mbar, before the fit results for the peak position scatter around a detuning of 0.1 GHz. Note, that the standard errors of the linear fit increase significantly for HCl pressures  $> 100$  mbar. This is due to fluctuations of the fundamental pulse energy, which disturbs the Lorentzian spectral line profile, which leads to higher fit residuals. Therefore, the result of a self-shift parameter of  $\delta_{\text{self}}(B) = -1.2 \text{ GHz}/\text{bar}$

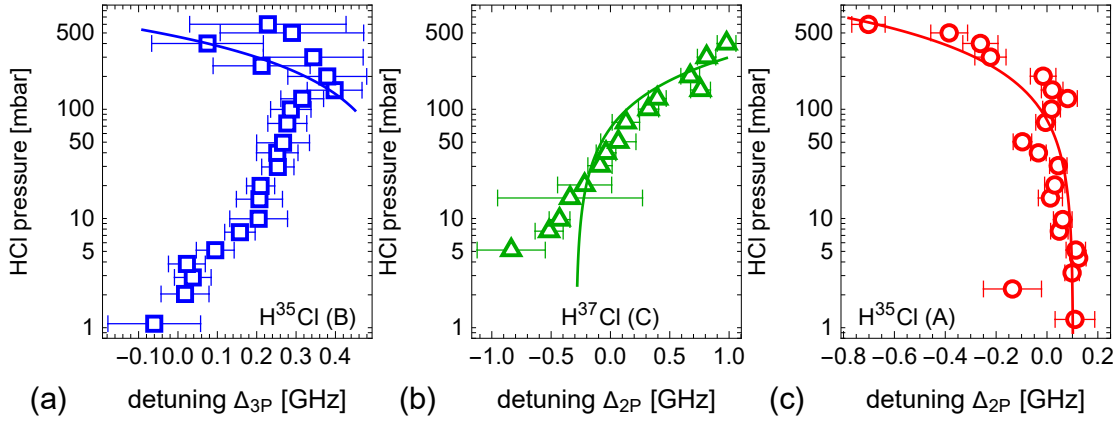


**Figure 3.16:** *HCl* pressure vs. multi-photon detuning of the resonance position, relative to the simulation value for (a) three-photon resonance (B) at fundamental wave number  $2807.92\text{ cm}^{-1}$  (b) two-photon resonance (C) at fundamental wave number  $2830.15\text{ cm}^{-1}$  and (c) two-photon resonance (A) at fundamental wave number  $2830.36\text{ cm}^{-1}$ . Points indicate the peak positions of the Lorentzian line shape, which we fitted to the THG spectra. The fundamental pulse energy was  $1.2\text{ mJ}$ . Solid lines give linear fits for higher *HCl* pressures. Error bars indicate standard errors. Note the logarithmic scale.

(or  $-0.04\text{ cm}^{-1}/\text{bar}$ ) is not representative of the experimental data. We did not find literature values for the self-shift parameter of the overtone transition. The two-photon resonance (C), shown in Fig. 3.16 (b), shifts strongly to positive detunings. The fit value of the self-shift coefficient is  $\delta_{\text{self}}(C) = 4.3\text{ GHz}/\text{bar}$  (or  $0.14\text{ cm}^{-1}/\text{bar}$ ). In contrast, the two-photon resonance (A) shifts to negative detunings. We determine the self-shift coefficient to  $\delta_{\text{self}}(A) = -1.3\text{ GHz}/\text{bar}$  (or  $-0.04\text{ cm}^{-1}/\text{bar}$ ). We compare these findings with literature data in Sec. 4.6.

### 3.5 Conclusion

In conclusion, we demonstrated detection of *HCl* molecules based on resonantly enhanced THG. We resolved both common isotopes of *HCl* and identified two- and three-photon resonances. With a numerical simulation we describe the THG spectrum and found quantitative agreement on two- and three-photon resonances, albeit an overestimation of the THG yield by approximately two orders of magnitude. From systematic investigations on the pressure dependence of the THG signal we found a detection limit of  $\approx 1\text{ mbar}$ , which we compared with literature values of alternative techniques. We found, that the detection limit already permits applications under realistic conditions. Further, we analysed self-induced collisional broadening and self-shifts of the resonance positions, as well as foreign-gas induced collisional broadening and found good agreement with the literature and our simulation. Shifts play a minor role but self-broadening and foreign-gas induced broadening significantly reduces the THG yield.

## Chapter 4

### Experimental results of SFM

In this chapter we discuss an alternative approach to molecule detection with two-photon resonant sum frequency mixing (SFM). Note, that the experimental data shown below is the result of a first test of an SFM implementation and is the subject of ongoing optimizations.

Consider the coupling schemes for resonantly enhanced THG and CARS in molecules. Our implementation of THG in Fig. 4.1 (a) benefits from low detunings to vibrational states, i.e., large nonlinear susceptibilities even though the vibrational transition moments are low. This is especially the case for the overtone transition at  $\nu = 3 \rightarrow 0$  with  $\omega_{\text{THG}}$ . Also, the THG signal wavelength is in the near-infrared spectral regime, i.e., larger than  $1 \mu\text{m}$ . Therefore, we have to apply an InGaAs avalanche photodiode, which possesses a low gain, when compared with photomultiplier tubes, which are sensitive in the visible regime. In contrast, CARS typically uses shorter wavelength pump and Stokes fields, where the frequency difference  $\omega_{\text{pump}} - \omega_{\text{S}}$  is equal to a vibrational transition with  $\nu = 0 \rightarrow 1$ . Hence, CARS benefits from electronic transition dipole moments on all optical transitions. Still, the detunings to the excited electronic state enter  $\chi^{(3)}$  inversely squared and can be large, i.e., in the range of a few  $10000 \text{ cm}^{-1}$ . The visible Anti-Stokes field with  $\omega_{\text{AS}} = 2\omega_{\text{pump}} - \omega_{\text{S}}$  is detectable with photomultiplier tubes.

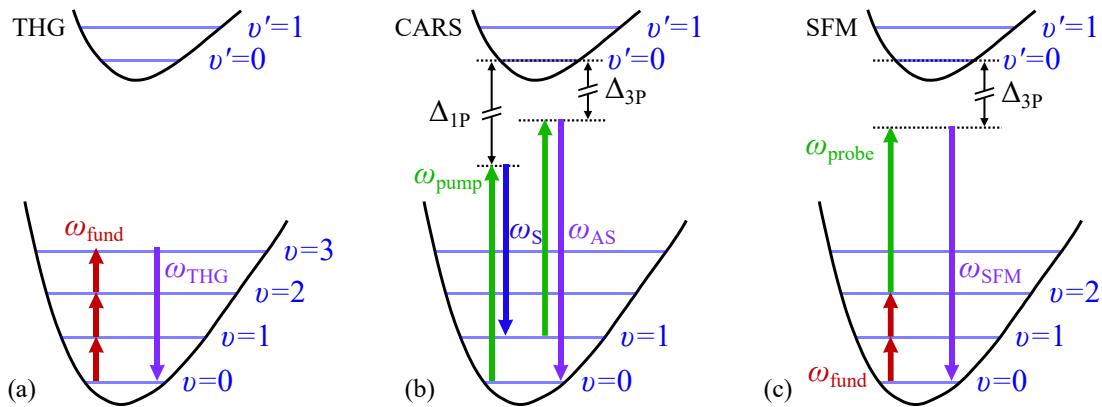


**Figure 4.1:** Coupling schemes for resonantly enhanced THG, CARS, and SFM (schematic).

We now combine both approaches in the SFM process, where we drive a vibrational two-photon resonance with mid-infrared fundamental radiation  $\omega_{\text{fund}}$  and probe with a near-infrared or visible field with  $\omega_{\text{probe}}$ , which yields a SFM signal at  $\omega_{\text{SFM}} = 2\omega_{\text{fund}} + \omega_{\text{probe}}$ . Compare Fig. 4.1 (c). Like for CARS, we benefit from the electronic transition dipole moments, albeit with a linear contribution of the detuning to the electronic state. Similar to THG, we have a low single-photon detuning and two-photon resonance to vibrational states. Additionally, the SFM signal wavelength is in the visible regime, i.e., detectable with photomultiplier tubes.

**Table 4.1:** Calculation of the nonlinear susceptibility for resonantly enhanced THG, CARS and SFM for  $H^{35}Cl$ . Parameters: HCl pressure  $p = 100$  mbar, number density  $\rho = 3.5 \times 10^{23} m^{-3}$ , resonant linewidth  $\Gamma_{20} = 1.5$  GHz.

method	unit	THG	CARS	SFM
$\lambda_1$	nm	3533 (fund)	1064 (pump)	3533 (fund)
$\lambda_2$	nm	-	1530 (S)	1064 (probe)
$\lambda_{\text{signal}}$	nm	1178	816	664
$\Delta_{1P}$	$cm^{-1}$	-8.8	68302	-8.8
$\Delta_{2P}$	$cm^{-1}$	0	0	0
$\Delta_{3P}$	$cm^{-1}$	-79.0	65439	62516
$\mu_{01}$	$10^{-30}$ Cm	0.20	3.7	0.20
$\mu_{12}$	$10^{-30}$ Cm	0.21	3.7	0.21
$\mu_{23}$	$10^{-30}$ Cm	0.26	3.7	3.7
$\mu_{03}$	$10^{-30}$ Cm	0.0013	3.7	3.7
$ \chi^{(3)} $	$pm^2/V^2$	4	0.3	209

We reinforce these arguments with a simple calculation of the nonlinear susceptibility in HCl molecules for all three approaches. For two-photon resonant excitation, the nonlinear susceptibility is  $\chi^{(3)}(\omega) \approx 2\rho\mu_{10}\mu_{21}\mu_{32}\mu_{30}/(\epsilon_0\hbar^3\Delta_{1P}\Delta_{3P}\Gamma_{20})$  with the number density  $\rho$ , transition dipole moments  $\mu_{ij}$ , the linewidth of the two-photon resonance  $\Gamma_{20}$  (FWHM) and single- and three-photon detunings  $\Delta_{2P}$  and  $\Delta_{3P}$  (compared to Eqn. (1.11) we do not sum over intermediate rotational states). Hence,  $\chi^{(3)}$  profits from large transition dipole moments and small detunings and linewidths. As we utilise (ns) mid-infrared laser pulses for THG and SFM, we compare the results with (ns) CARS with near-infrared pump and Stokes fields.

Tab. 4.1 gives detunings, transition dipole moments and nonlinear susceptibilities in HCl. We find, that  $\chi^{(3)}$  for THG is an order of magnitude larger than CARS, i.e., two orders of magnitude in signal power. The nonlinear susceptibility for SFM exceeds the THG value by more than an order of magnitude. These promising features of SFM, combined with the availability of the necessary wavelengths in our experimental setup enables us to perform first test experiments on SFM.

## 4.1 SFM Simulation

We further motivate the benefits of SFM by comparison of simulation results for THG and SFM. Some modifications to the THG model (shown in chapter 1) are necessary for a realistic description of the SFM process. In a simple approach we assume, that the confocal parameter of the mid-infrared fundamental field and the near-infrared probe field are the same. With this assumption the generated SFM field has the same confocal parameter and the model for the phase matching integral, given in Eqn. (1.7), holds true with a phase mismatch of

$$\Delta k_{\text{SFM}} = k_{\text{SFM}} - 2k_{\text{fund}} - k_{\text{probe}} = 2\pi \left[ \frac{n(\lambda_{\text{SFM}})}{\lambda_{\text{SFM}}} - \frac{2n(\lambda_{\text{fund}})}{\lambda_{\text{fund}}} - \frac{n(\lambda_{\text{probe}})}{\lambda_{\text{probe}}} \right]. \quad (4.1)$$

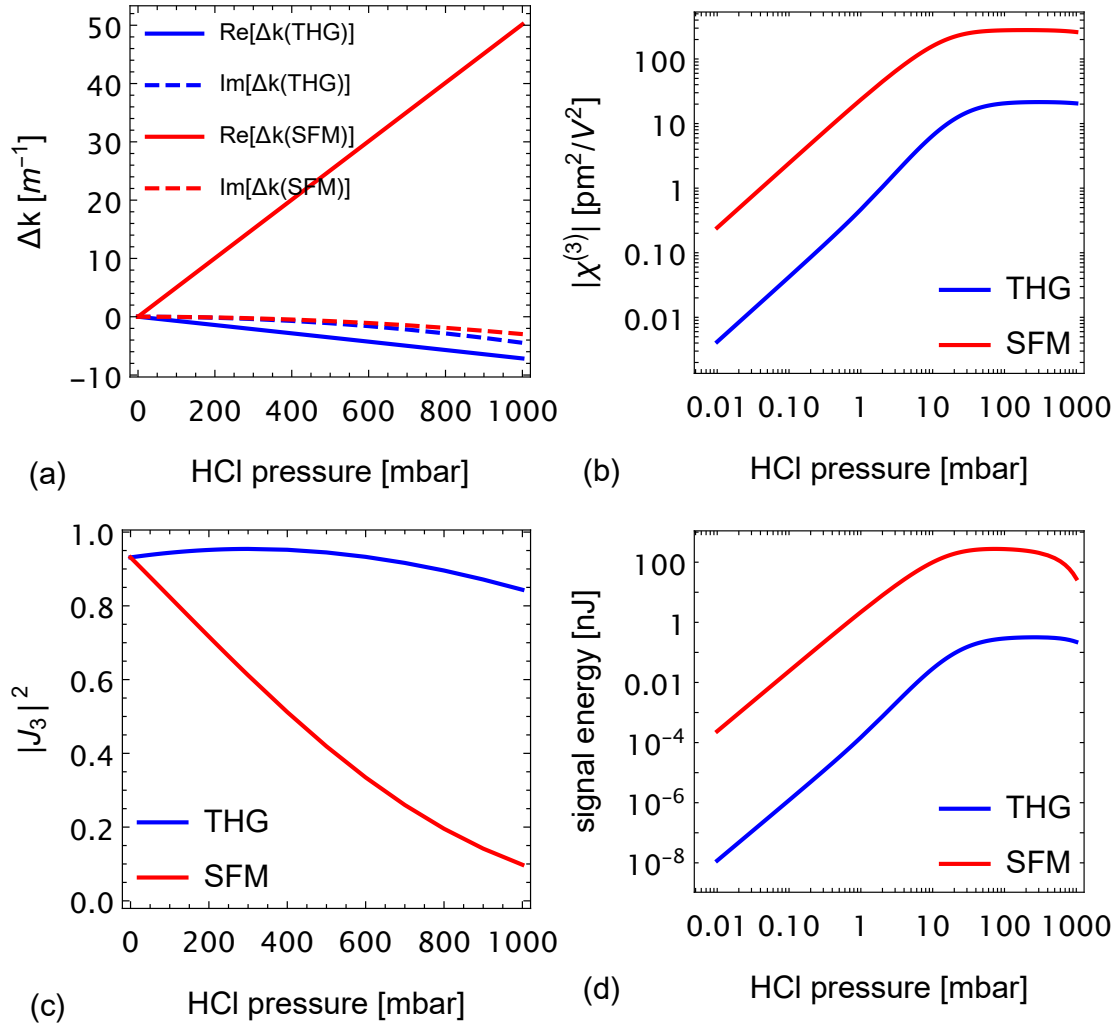


**Figure 4.2:** Comparison of the simulation results for SFM and THG vs. HCl pressure at the resonance (A) at  $\tilde{\nu}_{\text{fund}} = 2830.36 \text{ cm}^{-1}$  and  $\tilde{\nu}_{\text{probe}} = 9398.5 \text{ cm}^{-1}$ . (a) Wavevector mismatch vs. HCl pressure; (b) Absolute value of the nonlinear susceptibility  $\chi^{(3)}$  vs. HCl pressure in a double logarithmic scale; (c) Absolute square value of the phasematching integral  $J_3$  vs. HCl pressure (parameters:  $b = 6 \text{ cm}$ ,  $L = 5 \text{ cm}$  and  $z_0 = 3.65 \text{ cm}$ ); (d) Signal pulse energy for SFM and THG vs. HCl pressure in a double logarithmic scale (parameters:  $E_{\text{fund}} = E_{\text{probe}} = 1.2 \text{ mJ}$  and  $\tau = 8 \text{ ns}$ ).

Note, that we have to include the pressure and temperature dependent offsets of the refractive indices in this calculation. As we discuss in appendix A for HCl this is an approximation, which we have to validate in comparison with experimental data. Additionally, we consider a single rovibrational state in the electronic state  $C(1\Pi)$  and calculate the dipole moment for the Q branch ( $\Delta N = 0$ ) transition with  $\Delta \nu = 0$  to  $7.3 \times 10^{-30} \text{ Cm}$  [41]. We neglect, that the transition dipole moment for the vibronic  $\Delta \nu = 2$  transition might be lower by a factor of 2 [41]. Hence, our results for the SFM pulse energy might overestimate by one order of magnitude. We further assume that vibrational states of the electronic ground state have negligible contribution to the nonlinear susceptibility. This approximation is valid, as the dipole transition moments of rovibrational overtone transitions scale with  $\mu(\Delta \nu = \pm q) \sim x_e^{(q-1)}$  (see

Sec. 2.2). Following an analogous calculation as in Sec. 1 we find the SFM power [28]

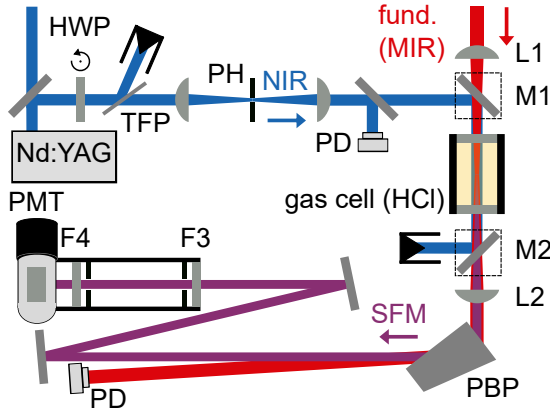
$$P_{\text{SFM}} = \frac{\mu_0^2 \omega_{\text{probe}} \omega_{\text{SFM}}}{4\lambda_{\text{fund}}^2} |\chi^{(3)}|^2 |J_3|^2 P_{\text{fund}}^2 P_{\text{probe}} \exp[-\alpha_{\text{SFM}} L]. \quad (4.2)$$

Fig. 4.2 illustrates the dependence of the components of the SFM power in Eqn. (4.2) upon the HCl pressure on two-photon resonance (A). Through addition of results for the THG simulation we directly compare the expectations for the application of molecule detection at low HCl pressures. A difference between both methods is the sign of the wave vector mismatch, see Fig. 4.2 (a). The imaginary parts, i.e., the absorption coefficients, follow similar pressure dependencies. Whereas the real part of  $\Delta k_{\text{THG}}$  is smaller than zero, the real part of  $\Delta k_{\text{SFM}}$  is larger than zero and has, in general, a larger pressure dependence. Hence, the absolute square value of the phasematching integral  $J_3$  shows different behaviours in Fig. 4.2 (c). The THG values rise slightly up to  $\approx 400$  mbar and fall for higher pressures due to absorption. For SFM we notice a significant drop of  $|J_3|^2$ , the signal halves at  $\approx 400$  mbar. However, at low HCl pressures  $|J_3|^2$  is comparable for both methods. Hence, both methods are suitable for molecule detection at low HCl pressures. The nonlinear susceptibility  $\chi^{(3)}$  depends on the HCl pressure through the number density and the collisionally broadened linewidth of the two-photon resonance. As we calculate the nonlinear susceptibility for both methods at the same resonance both values deviate from the linear rise at the same HCl pressure of  $\approx 100$  mbar and stay constant for larger HCl pressures (see Fig. 4.2 (b)). Note, that the values for  $\chi_{\text{SFM}}^{(3)}$  are one order of magnitude larger than for  $\chi_{\text{THG}}^{(3)}$ . Hence, due to the quadratic dependence of  $P_{\text{SFM}}$  upon  $\chi_{\text{SFM}}^{(3)}$  we expect the signal pulse energy for SFM to be two orders of magnitude larger than for THG (see Fig. 4.2 (d)). In the previous chapter we demonstrated a detection limit of  $\approx 1$  mbar, albeit this result takes experimental influences, i.e., off-resonant background signal and low detection sensitivity, into account. Hence, we expect an improvement of the detection limit by  $\approx 2$  orders of magnitude. The situation might be even more favorable for SFM, as we can measure the visible SFM signal wavelength with a photomultiplier tube, i.e., presumably at higher detection sensitivities.

## 4.2 Experimental setup

We discuss the changes to our experimental setup for implementation of SFM. Fig. 4.3 gives an schematic overview (see also [78]). We supply probe radiation at a wavelength of 1064 nm from the fixed-frequency Nd:YAG laser, which operates as pump laser for the OPA chain (compare Sec. 2.1). A spatial filter shapes the probe beam into a Gaussian beam profile. We use a high-power aperture with a diameter of 500  $\mu\text{m}$  (Lenox-Laser). The peak pulse energy for the probe pulses is 3.5 mJ and a variable attenuator (half-wave plate and thin film polarizer, TFP) controls the probe pulse energy for experiments. We monitor the probe pulse energy with a silicon photodiode (SM05PD1A, Thorlabs), which we calibrate with a pyroelectric sensor (PE50, Ophir). We collinearly combine the probe and fundamental fields with a dichroic mirror (L-06774, Laseroptik). Behind the gas cell, a dichroic mirror of the

same type (M2 in Fig. 4.3) separates the probe radiation from the SFM signal and the fundamental mid-infrared radiation. We determined the transmission of the mirror for the SFM signal radiation at  $\approx 664$  nm as 93 %, using a diode laser at 637 nm and a power meter (3A, Ophir) for calibration. Note, that the coating is highly reflective at wavelengths around 1064 nm. Hence, only  $\approx 10$  % of the THG passes the mirror. Therefore, in this first test experiment on SFM we could not simultaneously measure THG and SFM signals. The mirrors M1 and M2 in Fig. 4.3 are detachable to enable THG and SFM measurements in quick succession.



**Figure 4.3:** Schematic view of the experimental setup for SFM.

A Pellin Broca prism separates the visible SFM radiation from the fundamental mid-infrared radiation. We successfully suppress stray light with two apertures. A bandpass filter with a center wavelength of 650 nm and a spectral width (FWHM) of 40 nm removes a large part of the ambient visible light (F4 in Fig. 4.3, FB650-40, Thorlabs).

A photomultiplier tube (PMT, R4220 with socket E717-63, Hamamatsu), operated with a high-voltage supply (HNC 6000-10ump, Heinzinger), detects the SFM signal. While the PMT allows bias voltages up to 1000 V, we used a bias voltage of 400 V to reduce the anode

dark current. We confirmed the linearity of the PMT vs. SFM signal. Neutral density filters (F3) attenuate the SFM signal, if necessary. A transimpedance amplifier (LCPA-200, Femto) converts the current signal of the PMT into a voltage signal with a gain of  $10^5$  V/A.

As we already mentioned above, the probe radiation is collimated, whereas the fundamental mid-infrared radiation is focused into the gas cell. Fig. 4.4 (a) and (b) shows the horizontal and vertical beam radii vs. distance to the center of the gas cell. The probe radiation is well collimated and has a  $1/e^2$  radius  $\approx 2 - 3$  times larger than the fundamental radiation. Note, that this difference in radius and divergence limits the maximum conversion efficiency, but it enables simple alignment of the overlap. We ensure in this geometry, that the probe laser generates SFM signal all across the fundamental mid-infrared profile.

Fig. 4.4 (c) and (d) shows horizontal and vertical slices of the beam profiles close to the focus of the fundamental radiation. We find, that fits of Gaussian functions describe both beams well. For the probe radiation we find for the  $1/e^2$  radii: horizontal 0.94 mm, vertical 0.98 mm and for the fundamental radiation: horizontal 0.22 mm, vertical 0.18 mm. As a consequence of the collimated probe radiation, the peak probe intensity is only  $\approx 30$  MW/cm<sup>2</sup> (at  $E_{\text{probe}} = 3.5$  mJ), i.e., an order of magnitude lower, than the peak intensity of the fundamental radiation with  $\approx 300$  MW/cm<sup>2</sup> (with  $E_{\text{fund}} = 1.5$  mJ). This complicates a comparison between SFM and THG, as the intensity of the probe field should be comparable to the intensity of the fundamental field. We will correct this in future investigations by implementation of confocal focusing for the probe radiation.

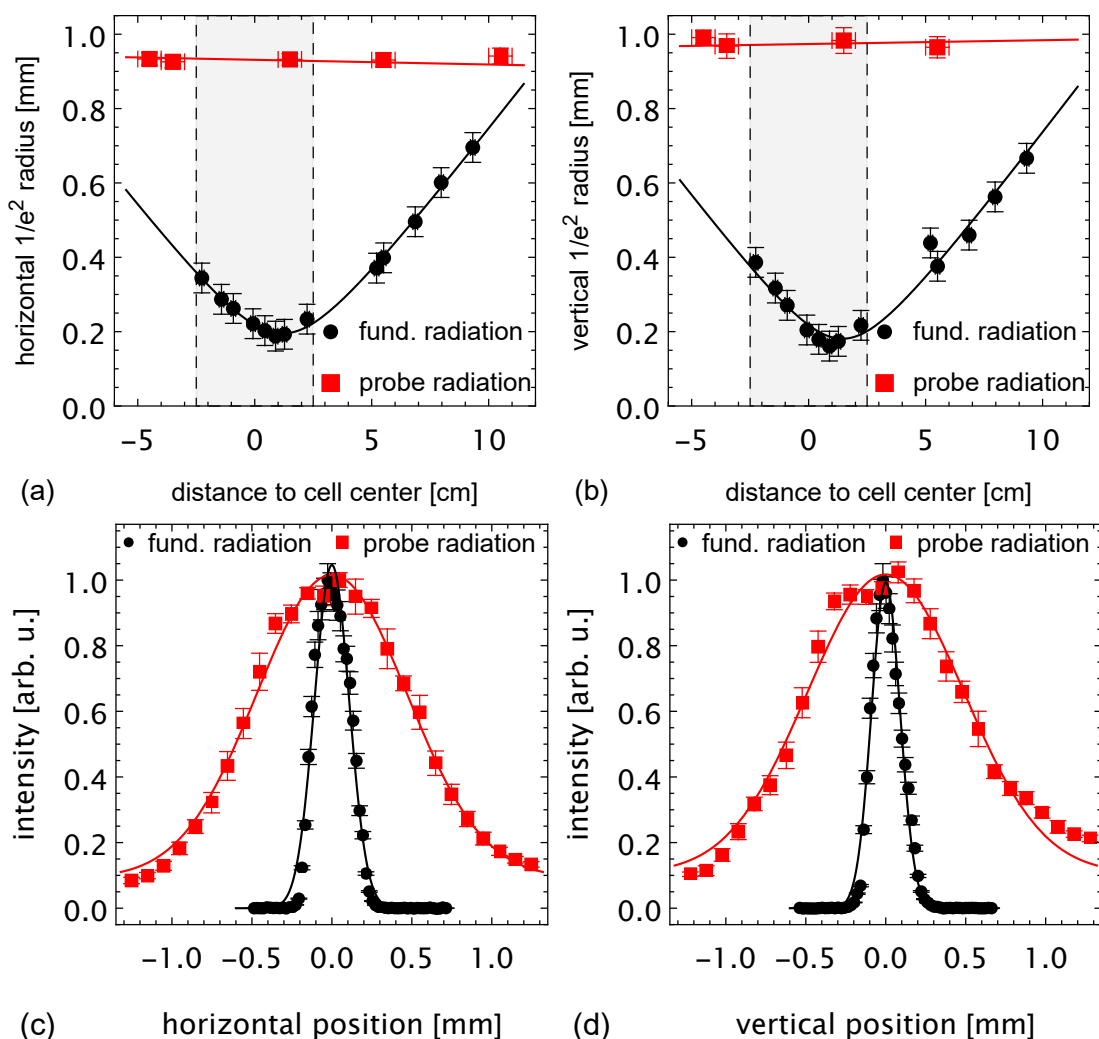


**Figure 4.4:** Beam radii ( $1/e^2$ ) vs. distance to the center of the gas cell. Comparison of the focus of the fundamental radiation (black) and the collimated probe radiation in the (a) horizontal and (b) vertical axis. The shaded area indicates the 5 cm long gas cell. Intensity beam profiles of the fundamental and probe radiation at the focus position of the fundamental beam vs. (c) horizontal (position: 1.3 cm) and (d) vertical axis (position: 1.5 cm).

### 4.3 SFM spectroscopy

We present preliminary results from our first test of SFM in HCl. In the SFM spectrum we may, in principle, find only single- and two-photon resonances, no three-photon resonances as in THG. Like in THG, the single-photon resonances do not provide resonance enhancement, as the fundamental radiation is absorbed.

Fig. 4.5 shows the SFM spectrum over a spectral range of  $\approx 220$  GHz, which contains several two-photon resonances of both common HCl isotopes. Evidently, the first test of SFM is successful and SFM provides spectral information on two-photon resonances of HCl. We added a THG spectrum to Fig. 4.5. For comparison we normalize the maximal signal at the two-photon resonance (A) at  $2830.36 \text{ cm}^{-1}$  for the SFM and THG spectra. We identify all spectral lines in the SFM data with

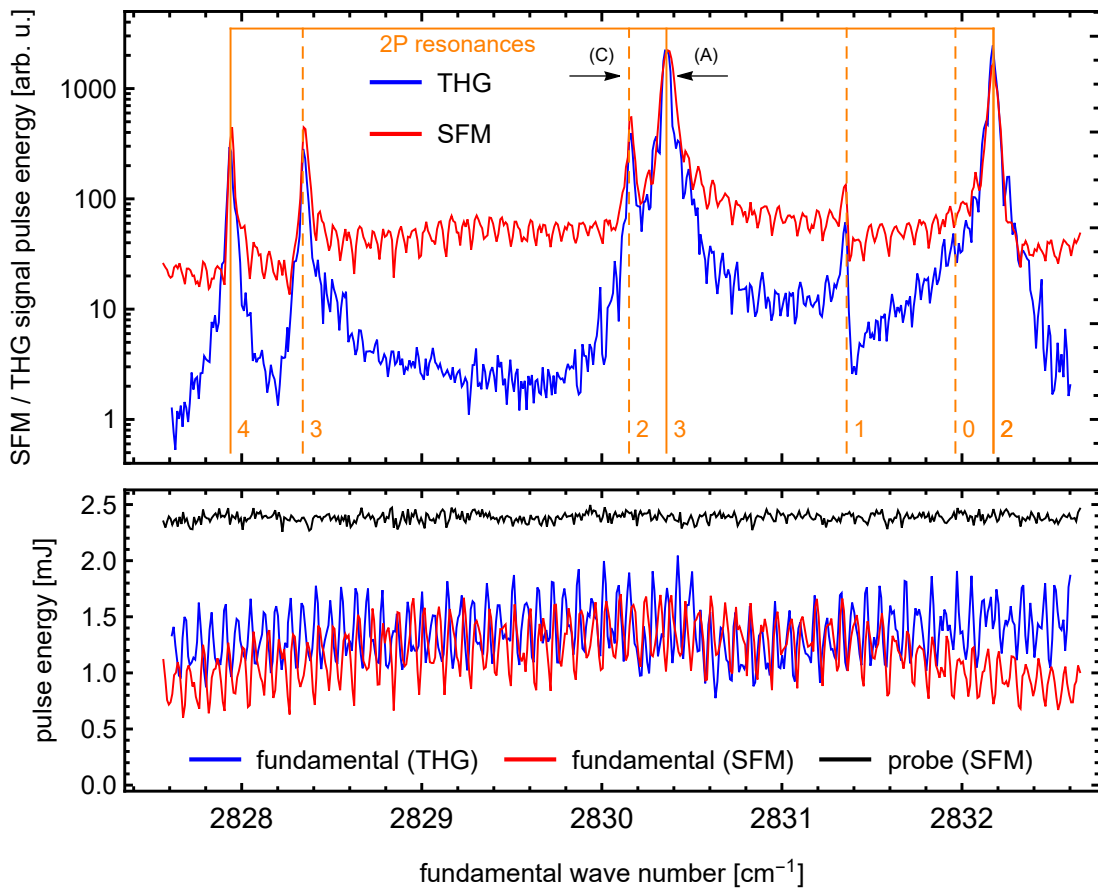


**Figure 4.5:** (top) SFM and THG signal pulse energy vs. fundamental wave number at a HCl pressure of 100 mbar. The data is binned in  $0.01 \text{ cm}^{-1}$  intervals. Note the logarithmic scale. We normalized the SFM data to the THG results. Orange vertical lines indicate the frequency positions of two-photon resonances (solid line:  $\text{H}^{35}\text{Cl}$ , dashed line:  $\text{H}^{37}\text{Cl}$ ). Labels give the rotational quantum numbers of the corresponding ground states. (bottom) Corresponding fundamental and probe pulse energies vs. fundamental wave number.

relative line intensities, comparable to the THG results. Only for the dispersive line at  $2831.3 \text{ cm}^{-1}$  we find a small difference of the relative line intensities between THG and SFM data. Note, that we measured the THG and SFM spectra with different detection setups and, hence, cannot yet quantify the SFM signal pulse energy. Also, the intensity of the probe radiation is lower than for the fundamental field due to the collimated probe beam.

As a major difference between the THG and the SFM spectra we find, that the dynamic range is worse for SFM ( $\approx 1 - 2$  orders of magnitude), when compared with the dynamic range for THG ( $\approx 3$  orders of magnitude). This is due to a rather large background signal in the case of SFM. We found, that the source of this signal is off-resonant SFM in the  $\text{CaF}_2$  windows, which increases with measurement time and coincides with permanent damage on the entry and exit facets of the  $\text{CaF}_2$  windows. We will further analyse the SFM background signal in Sec. 4.5. Due to the lower background signal we were able to increase the dynamic range of the THG data by removing all neutral density filters from the APD for detection of the off-resonant

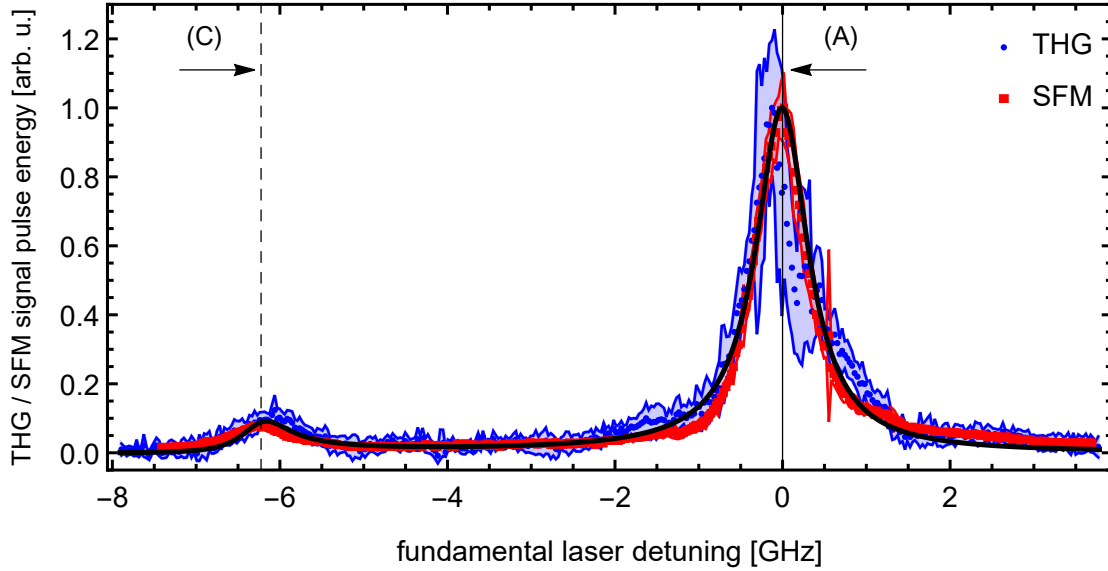


**Figure 4.6:** Normalized SFM and THG signal pulse energy vs. detuning of the fundamental radiation at the two-photon resonances (A) and (C) with a HCl pressure of 100 mbar. The mean fundamental pulse energy was 1.2 mJ and the probe pulse energy was 2.4 mJ for the SFM measurement. We correct the SFM and THG signal pulse energy for fluctuations of the fundamental pulse energy. The shaded areas indicate standard deviations for 30 MHz bins. The black line indicates the SFM simulation result.

THG signal. This was not possible in the case of SFM, hence, we measured with a neutral density filter (optical density: 1, NE10A-B, Thorlabs).

Furthermore, we notice a periodic structure on the background signal, in particular, as the signal axis is on a logarithmic scale. This is due to modulation of the fundamental pulse energy by an (unwanted) etalon in the OPA chain, as described in Sec. 2.1.2. The lower row of Fig. 4.5 shows the fundamental pulse energy for the THG and SFM measurements, as well as the probe pulse energy (note, that the probe beam profile does not match the beam profile of the fundamental radiation). We find a correlation between the fundamental pulse energy and the background signal for both processes. The effect is more pronounced in the SFM data because the background signal is significantly larger than during the THG measurements.

We compare the SFM data measured at the resonances (C) at  $2830.15 \text{ cm}^{-1}$  and (A) at  $2830.35 \text{ cm}^{-1}$  with the THG data shown in Sec. 3.1.1. Fig. 4.6 shows normalized SFM and THG spectra in more detail. For comparison, we added the result of the SFM simulation to the plot. The SFM data shows considerably lower shot-to-shot fluctuation than in the THG case. On resonance (A) we do not observe the significant deviations from the expected Lorentzian line shape as in the THG spectrum. We find a good agreement between the SFM data and the SFM simulation. Note, that the resonance (C) is a symmetrical Lorentzian-shaped line, whereas the simulation expects an asymmetrical, slightly dispersive line shape. We also observed this deviation in the THG case (see Fig. 3.4). The linewidth of the resonance, when measured with SFM, appears to be slightly narrower than the simulation predicts. We will discuss this observation in Sec. 4.6. Note, that these test experiments are an extension to our investigations of THG.

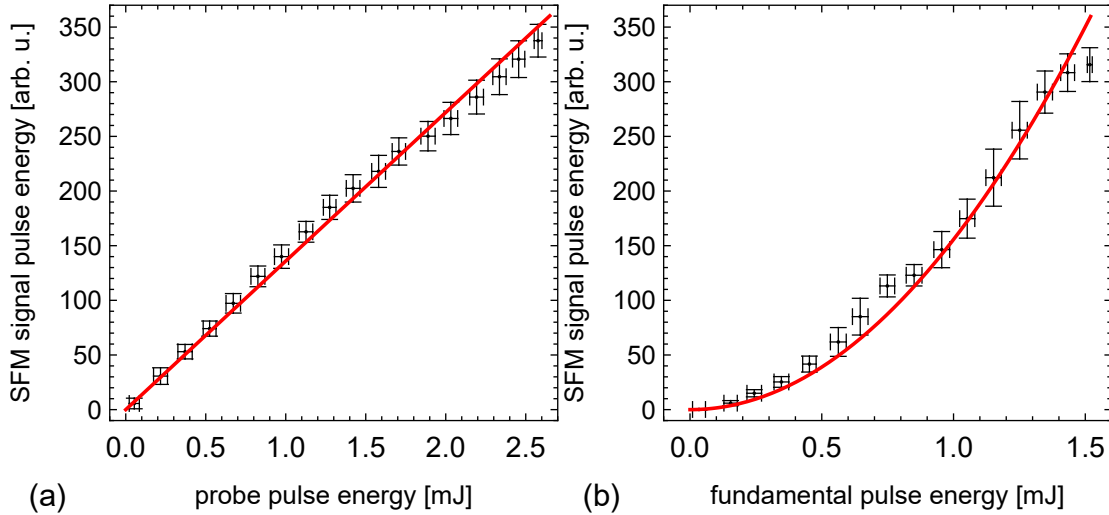


**Figure 4.7:** SFM signal pulse energy at the two-photon resonance (A) vs. (a) probe and (b) fundamental pulse energy. The HCl pressure was 100 mbar. For the variation of the probe pulse energy the fundamental pulse energy was 1.5 mJ. For the variation of the fundamental pulse energy the probe pulse energy was 2.4 mJ. The red lines depict (a) a linear fit and (b) a quadratic fit. Error bars indicate standard deviations.

## 4.4 Intensity dependence

To verify, that we indeed detected a SFM signal we check the dependence of the SFM signal on the fundamental and probe intensity. Fig. 4.7 (a) gives the dependence of the SFM signal upon change of the near-infrared probe pulse energy. We observe the expected linear dependence with a slight deviation at pulse energies larger than 2 mJ. The dependence on the mid-infrared fundamental pulse energy, given in Fig. 4.7 (b), is well-described by a quadratic fit with minor deviations at 0.8 mJ and at the last binned data point at 1.5 mJ, these deviations might also originate in the nonlinear calibration of the saturating photo detectors (see Sec. 2.5.1). Beside these minor discrepancies we note a good description of the intensity dependencies. Hence, we can confirm, that we did indeed detect two-photon resonant SFM in HCl.

In our experiments with two-photon resonant THG in HCl (see Sec. 3.2) we noticed considerable saturation of the two-photon transition even at moderate peak intensities in the gas cell. Even though the fundamental intensity is comparable to the THG experiments, we do not observe signs of saturation in the SFM data. The reason for this behaviour is still unclear and subject of an ongoing investigation.

## 4.5 Analysis of the SFM background signal

Whereas the constant background signal in the THG measurements effected our measurements only slightly, we notice a different dynamic within SFM measurements. We saw in Fig. 4.5 that the background signal in the SFM spectrum is an order of magnitude larger than in the THG spectrum. Also note the larger influence of fluctuations of the fundamental pulse energy, due to the etalon in the OPA chain (see

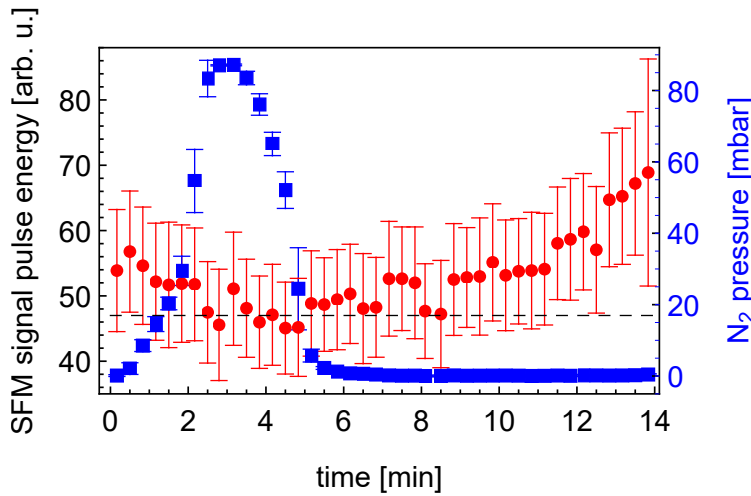


**Figure 4.8:** SFM background signal pulse energy vs. time, the cell was filled with  $N_2$  and evacuated afterwards (blue data points, right axis).  $\tilde{\nu}_{\text{fund}}$  was  $2830.41 \text{ cm}^{-1}$ ,  $E_{\text{fund}} = 1 \text{ mJ}$ , and  $E_{\text{probe}} = 2.4 \text{ mJ}$ . The fundamental intensity varied by 15% during the measurement time. We corrected for this variation, assuming a quadratic dependence of the fundamental intensity. Dashed black line to guide the eye.

Sec. 2.1.2).

We analyse the SFM background signal in more detail. Possible reasons for a background signal could be stray light (either from ambient light or from the probe laser), electronic noise, dark current of the detector, nonresonant SFM in HCl, or off-resonant SFM in the cell windows. The background signal propagates collinearly with the SFM signal beam. Hence, the central wavelength of the background signal is similar or identical to the wavelength of the SFM signal, due to the dispersion of the Pellin Broca prism (compare Fig. 4.3). With apertures and measures to darken the detection setup we completely remove stray light (ambient light and probe pulses) from reaching the detector. The background signal only appears, if both fundamental and probe radiation are present and overlap in the gas cell. Furthermore, the temporal trace on the oscilloscope is identical with the result of a resonant SFM signal. The signal persists in an evacuated cell. We notice damage on the entry and exit facets of the  $\text{CaF}_2$  of the gas cell. We suspect, that the background signal emerges from off-resonant SFM in the  $\text{CaF}_2$  windows. To systematically analyse this hypothesis we measure the dependence of the background signal on the incident pulse energies and check, if there is a dependence on nitrogen pressure in the cell.

First, we monitor the background signal in an evacuated gas cell vs. time. In Fig. 4.8 we see, that the background signal does not fall when we fill the gas cell with  $\approx 80 \text{ mbar}$  nitrogen ( $N_2$ ). The signal persists, even after evacuation of the gas cell. In fact, we notice a rising background signal with measurement time. After 10 min the signal increases by almost 50%. Note, that the fundamental pulse energy increases linearly from 1 to 1.15 mJ during this time. We compensate for this deviation, according to Eqn. (2.1), assuming an quadratic dependence of the SFM signal upon the fundamental pulse energy. Nevertheless, the rise of the background signal is significant (compare the dashed line in Fig. 4.8).

To find the impact of the damage on the cell windows we measure the dependencies of the background signal on the probe and fundamental pulse energy in two configurations in quick succession: First, in a configuration, where the beams overlap in a damaged position of the windows and secondly, after moving the gas cell hori-

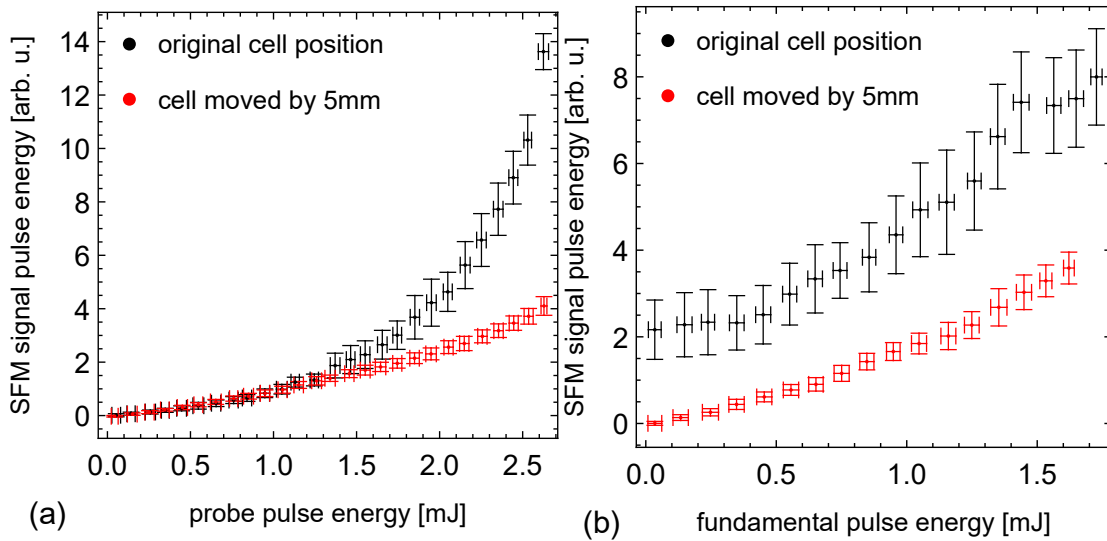


**Figure 4.9:** Background signal pulse energy in the evacuated cell vs. (a) probe pulse energy and (b) fundamental pulse energy. The fundamental frequency was  $2829.89\text{ cm}^{-1}$ , the fundamental pulse energy was 1.5 mJ in (a) and the probe pulse energy was 2.4 mJ in (b). Black data points show a measurement with damaged  $\text{CaF}_2$  windows, red data points show a measurement with the gas cell moved by 5 mm, i.e., without damaged windows. Error bars indicate standard deviations.

zontally by 5 mm, i.e., a position without damaged windows. Fig. 4.9 (a) gives the dependence of the background signal on the probe pulse energy. Whereas the signal follows a linear function after changing the position, the black data points deviate at a probe pulse energy of 1.3 mJ and show a nonlinear dependence afterwards. Neither a low order polynomial, nor an exponential law describe the experimental data. This leads to the assumption, that the background signal increased during the with measurement time, as observed before.

In Fig. 4.9 (b), the background signal pulse energy in the original position shows an offset of 2 arbitrary units, even at very low fundamental pulse energies of  $\approx 30\ \mu\text{J}$ . Unfortunately, we did not block the fundamental radiation in this configuration. Typically, we observed no background signal, while blocking either the probe or the fundamental radiation. Except for the offset signal, the signal shows roughly the same dependence on the fundamental pulse energy, i.e., a quadratic function, as expected for the SFM process.

The photo damage on the entry and exit facets of the  $\text{CaF}_2$  windows appears to be the product of melting, i.e., a thermal effect. It has roughly the size of the (collimated) probe radiation. The photo damage threshold for  $\text{CaF}_2$  is larger than  $20\text{ J/cm}^2$  (1053 nm, 1 ns) [79]. This corresponds to an estimated damage threshold of  $57\text{ J/cm}^2$  for the probe radiation (1064 nm, 8 ns). Inhomogeneities, surface defects and dust deposition will significantly reduce the damage threshold. This might explain the occurrence of the photo damage at low fluences of  $< 0.2\text{ J/cm}^2$  for the probe radiation and  $< 2.4\text{ J/cm}^2$  for the fundamental radiation.

The background signal significantly disturbed our first test of SFM. Hence, we will reduce the background signal in future investigations, for example, with a longer gas cell (in relation to the confocal parameter of the fundamental radiation). This

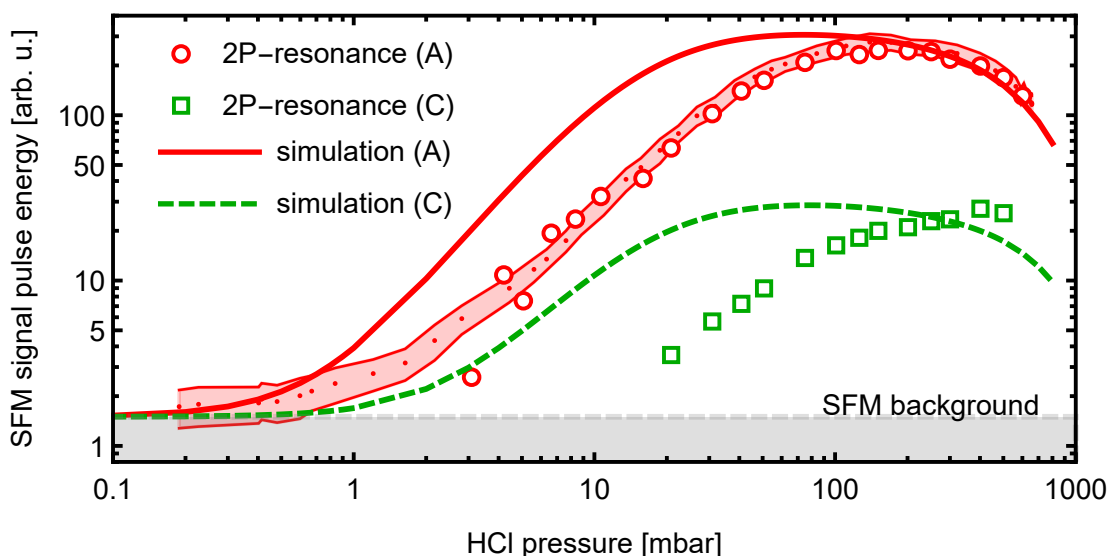


**Figure 4.10:** SFM signal pulse energy vs. HCl pressure at the two-photon resonance (A) at  $2830.36\text{ cm}^{-1}$  and the weaker two-photon resonance (C) at  $2830.15\text{ cm}^{-1}$ . The fundamental pulse energy was 1.4 mJ and the probe pulse energy 2.4 mJ. The shaded area indicates standard deviations. Symbols indicate the peak signal yields from fits to the spectral lines. Lines depict the normalized SFM simulation for both resonances with an offset of 1.5 arbitrary units. Note the double logarithmic scale.

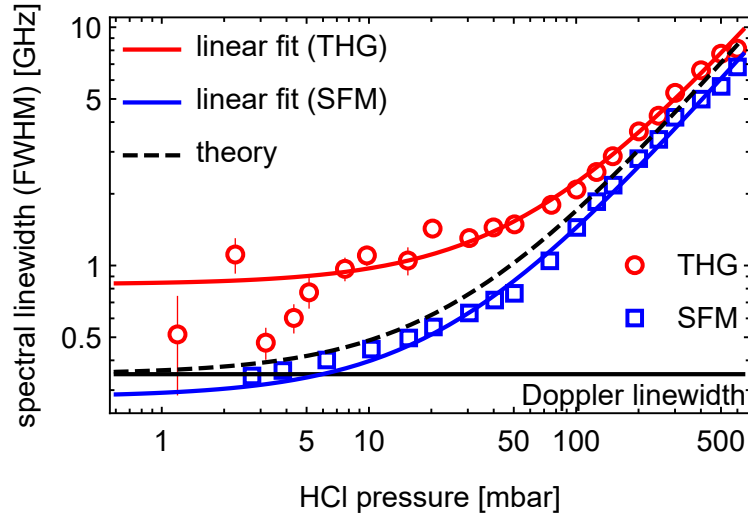
configuration reduces the intensity on the cell windows, albeit providing lower values for the phase matching integral  $J_3$  due to  $b < L$ . Other possibilities to reduce the background may be a noncollinear setup, even though SFM cannot be phasematched in such a configuration. Also setups without windows, e.g., with a gas jet or a laminar flow will reduce the background signal.

## 4.6 Pressure dependence of the SFM signal

We analyse the pressure dependence of the SFM signal pulse energy to determine the detection limit of HCl molecule with SFM, even though our experimental setup is not optimal with the background signal discussed above. Fig. 4.10 gives the variation of the SFM signal pulse energy upon the HCl pressure in the cell. The behaviour of the two-photon resonance (A) of the isotope  $\text{H}^{35}\text{Cl}$  is comparable to the observations made with THG (see Sec. 3.3) with the notable difference, that the signal does not merely saturate beyond 200 mbar but drops significantly. This is due to phasematching issues with a positive wave vector mismatch and well-described by the SFM simulation result (compare Sec. 4.1).

The data points measured on resonance (A) match well to the normalized simulation results for HCl pressures  $> 100$  mbar. At lower HCl pressures we observe a deviation from the simulation. This might be due to the spectral linewidth of the fundamental and probe pulses, which we did not consider in the simulation. The pressure dependence of resonance (C) for the isotope  $\text{H}^{37}\text{Cl}$  is comparable to the observations from the THG measurements shown in Fig. 3.11 with the difference, that we were not able to conduct nonlinear fits to the data below HCl pressures of

**Figure 4.11:** Spectral linewidth (given as FWHM) of the two-photon resonance (A) vs. HCl pressure. Points indicate the result of Lorentzian fits (or Fano fits for SFM spectra, measured at HCl pressures 4 – 20 mbar). The horizontal line indicates the Doppler-broadened linewidth of resonance (A). Lines give linear fits to the data. The dashed black line gives the simulation expectation.  $E_{\text{fund}} = 1.4$  mJ and  $E_{\text{probe}} = 2.4$  mJ. Note the double logarithmic scale.



10 mbar. We observe saturation of the peak values for the SFM signal pulse energy but no drop at larger HCl pressures like in the case of resonance (A) or the simulation result.

This kind of measurement is difficult to conduct with the current state of the experimental setup, as we have to deal with a background signal, which increases with measurement time. Therefore the chronological time order of the measurements in Fig. 4.6 is important. First, we conducted the variation of the HCl pressure on resonance (A). We did not remove a background signal but conducted only one measurement with the neutral density filter with optical density 1. Afterwards, we measured reference spectra at the beginning and end of the 7 h measurement campaign of SFM spectra at 26 different HCl pressures. Unfortunately, measurements below 2 mbar were not successful due to strong fluctuations of the background signal with the fundamental pulse energy. The last measurement with a signal-to-background ratio  $> 1$  was conducted at 2.2 mbar. Here we observed a large background signal, which was almost 5 times as big as at the beginning of the measurement campaign. With these experimental struggles we cannot determine a detection limit lower than  $\approx 2$  mbar. Nevertheless, already in our first test setup with the severe background problems, we reach a particle detection limit in a range, relevant for applications. Also, we notice lower standard deviations in the SFM signal and lower electronic noise due to the detector, when compared with the THG measurements. Finally, due to the strong background signal, we could not operate the PMT at maximal bias voltage and gain. Improvements of the experimental setup, as discussed in the previous section, may reduce the background signal significantly, and, hence, improve the detection sensitivity for SFM with regard to the THG results.

$E_{\text{fund}}$  was = 1.4 mJ, and  $E_{\text{probe}} = 2.4$  mJ Fig. 4.11 compares the result for the linewidth of the strongest two-photon resonance at  $2830.36 \text{ cm}^{-1}$ , labelled (A), for THG and SFM. The linewidths (FWHM) derived from SFM spectra seem to be lower than the values from THG spectra. We also observe less fluctuations at lower pressures

in SFM data, as indicated by low standard deviations. The systematic difference could be due to the smaller linewidth of the Fourier-limited probe pulse at 1064 nm, compared to the mid-infrared fundamental pulses. We get a linewidth of  $\approx 55$  MHz for a pulse with duration of 8 ns, instead of  $\approx 97$  MHz for the mid-infrared pulse (compare Sec. 2.1.3). We noticed, that fluctuations of the fundamental pulse energy, both stochastically and systematic, due to the interference effects, have a large impact on the line shape. These influences cannot be completely compensated from the data (see Sec. 2.1.2).

The linear fits given in Fig. 4.11 describe the data points well beyond HCl pressures 50 mbar, with an exception for SFM measurements at pressures larger than 400 mbar. Without these three data points the self-broadening coefficient is  $0.207 \text{ cm}^{-1}/\text{bar}$ , i.e., close to the simulation value of  $0.225 \text{ cm}^{-1}/\text{bar}$ . The self-broadening coefficient from the THG data was  $0.233 \text{ cm}^{-1}/\text{bar}$ , i.e., also close to the expectation. Below  $\approx 50$  mbar the uncertainties of the nonlinear fits gets high due to the asymmetrical line shape, higher influence of the background signal, and fluctuations therein. Li *et al.* measured self-broadening coefficients for the first overtone band ( $\nu = 0 - 2$ ) [80]. Note, that the authors state their results for HCl pressures between 0.3 and 1.1 bar, as the instrument line shape limited the pressure range. Also note, that the specific overtone transition in our case is forbidden due to the selection rules for the rotational quantum number. Hence, we compare our measurement with the allowed overtone transition originating in the same rotational ground state  $N_1 = 3$ :  $0.225 \text{ cm}^{-1}/\text{bar}$  [80]. Hence, we find good agreement between measurement data, our simulation and the literature.

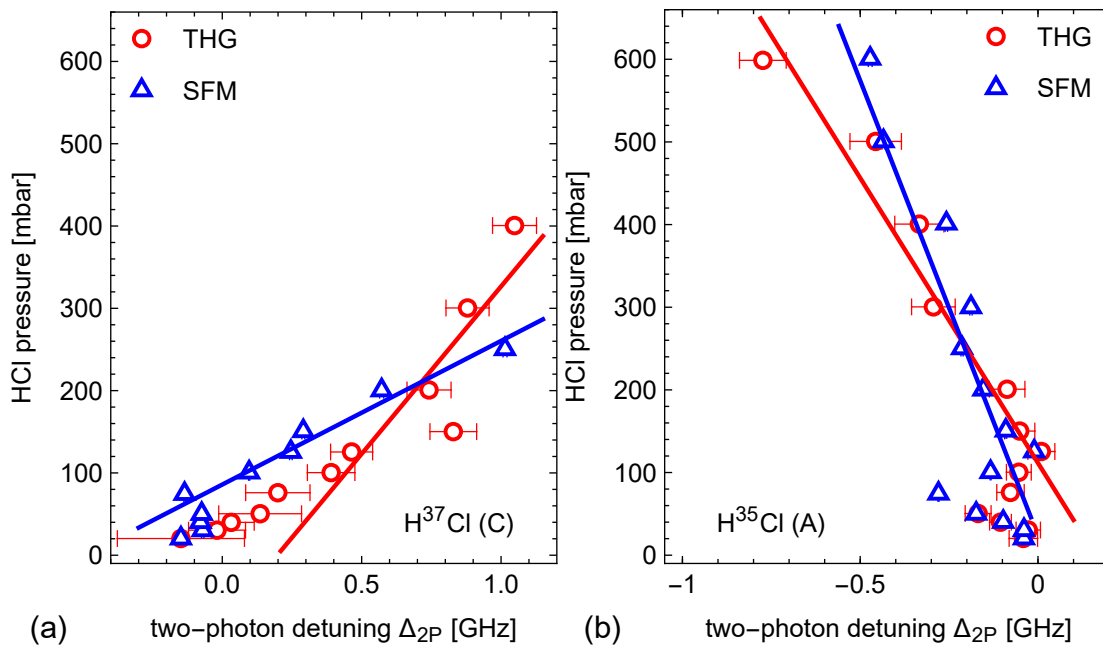


**Figure 4.12:** HCl pressure vs. two-photon detuning of the resonance position, relative to the simulation value for (a) two-photon resonance (C) and (b) two-photon resonance (A). Points indicate the peak positions of the Lorentzian line shape, which we fitted to the THG and SFM spectra (fundamental pulse energy 1.4 mJ, probe pulse energy 2.4 mJ). Solid lines give linear fits for HCl pressures > 100 mbar. Error bars indicate standard errors.

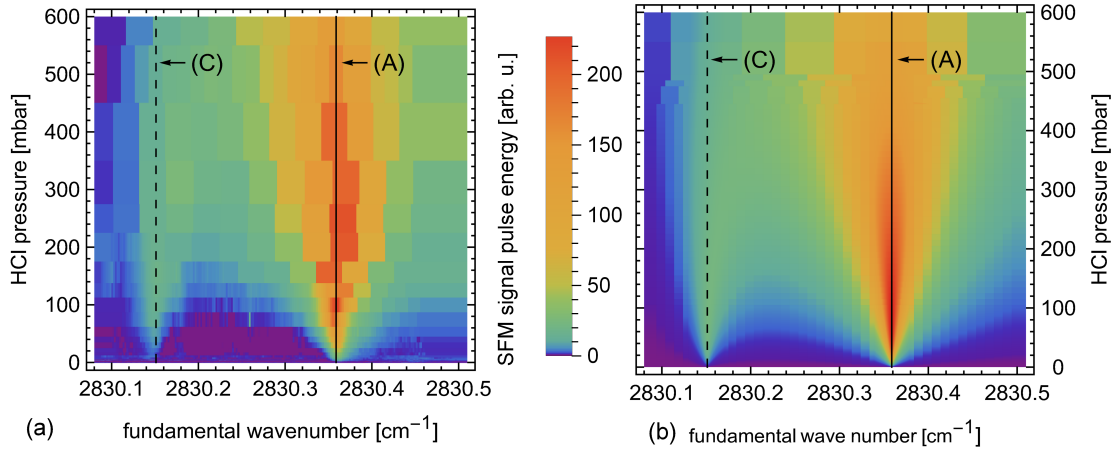


**Figure 4.13:** SFM signal pulse energy vs. HCl pressure and fundamental wave number at the two-photon resonances (C) and (A). (a) Experimental data, (b) numerical simulation for the resonances (C) and (A). Black vertical lines indicate the expected spectral positions of the multi-photon resonances (solid line for  $H^{35}Cl$ , dashed line for  $H^{37}Cl$ ). The fundamental pulse energy was 1.4 mJ and the probe pulse energy 2.4 mJ. We correct the SFM signal pulse energy for fluctuations of the fundamental pulse energy. Note the different color scales. For better comparison, we normalized the simulation result to the peak SFM signal pulse energy in the experimental data.

Beside self-broadening we also observed self-induced variations of the resonance positions (see Sec. 3.3). With the SFM measurements we get additional information to analyse the self-shift in the case of two-photon resonances. Fig. 4.12 compares the SFM results with the corresponding THG measurements. Note, that compared with Fig. 3.16 we present the data in a linear scale. The data on resonance (C) for the isotope  $H^{37}Cl$  in Fig. 4.12 (a) shows a strong, positive shift in both channels. From the linear fits we derive pressure shift parameters  $\delta_{\text{self}}^{(\text{THG})}(C) = 2.46 \text{ GHz/bar}$  (or  $0.082 \text{ cm}^{-1}/\text{bar}$ ) and  $\delta_{\text{self}}^{(\text{SFM})}(C) = 5.73 \text{ GHz/bar}$  (or  $0.191 \text{ cm}^{-1}/\text{bar}$ ), i.e., a value more than twice of  $\delta_{\text{self}}^{(\text{THG})}(C)$ . For the other resonance, shown in Fig. 4.12 (b), we get the coefficients  $\delta_{\text{self}}^{(\text{THG})}(A) = -1.45 \text{ GHz/bar}$  (or  $-0.048 \text{ cm}^{-1}/\text{bar}$ ) and  $\delta_{\text{self}}^{(\text{SFM})}(A) = -0.91 \text{ GHz/bar}$  (or  $-0.030 \text{ cm}^{-1}/\text{bar}$ ). While the qualitative behaviour is identical, the values determined with THG data are higher and the data spreads further. This effect is less pronounced in the case of resonance (A) for the  $H^{35}Cl$  isotope.

Li *et al.* derived a self-shift coefficient of  $\delta_{\text{self}} = -0.187 \text{ GHz/bar}$  (or, when expressed in wave numbers  $-0.062 \text{ cm}^{-1}/\text{bar}$ ) from two-photon absorption spectra with  $N_1 = 3$  of  $H^{35}Cl$  [80]. Our results are a factor of 2–3 smaller than reported. A possible explanation may be, that the cited value is no good approximation for the two-photon resonance discussed here, as the one-photon transition at  $2830.36 \text{ cm}^{-1}$  is forbidden due to the selection rule for the rotational quantum number. Li *et al.* further discuss a strong dependence of the self-shift coefficient on the rotational quantum number. The Lorentzian fits applied to the data of both methods might also be disturbed by residual asymmetry introduced by the interference with the background signal of the  $CaF_2$  windows.

Fig. 4.13 (a) shows the measurement data on SFM spectra vs. HCl pressure in a two-dimensional representation. Both two-photon resonances in the covered spectral range are clearly identifiable, note the nonlinear color scale. We compare the data with the SFM simulation, normalized to the data, in Fig. 4.13 (b). The drop of the SFM yield for pressures larger than 400 mbar and the linewidth of resonance (A) is well-described by the simulation. We notice, that the asymmetry of the resonance (A) at  $2830.35\text{ cm}^{-1}$  is more pronounced and the transition from the Fano line shape to a Lorentzian line shape at higher pressures is observable in Fig. 4.13 (a). Compare the flanks of resonance (A): on the left side the signal drops to zero sharply, whereas on the right side the decrease of the SFM signal is more smoothly. Also note, that the SFM signal between the two resonances is consistently zero. We did not observe this in the THG measurement (see Fig. 3.13).

## 4.7 Conclusion

In conclusion, we demonstrated a first test of two-photon resonant SFM for the detection of HCl molecules. We replicated the results of the THG investigations and found good accordance with a numerical simulation. However, we noticed a significant background SFM signal, which constrained the detection limit for SFM. Hence, improvements of the experimental setup and further investigations are necessary for a fair comparison of both methods.

## Conclusion and outlook

In this work we presented thorough experimental studies on resonantly enhanced third harmonic generation (THG) driven by mid-infrared, spectrally narrowband, nanosecond laser pulses tuned in the vicinity of rovibrational molecular resonances with hydrogen chloride (HCl) molecules as a test gas. In contrast to other approaches for nonlinear spectroscopy, the technique requires only a single driving laser beam, which facilitates applications.

As a major advantage of the THG approach among rovibrational states in the electronic ground state of the molecules, we drive the frequency conversion process simultaneously close to single-, two-, and three-photon resonances, with typical detunings in the range of  $10 - 100 \text{ cm}^{-1}$  only. Tuning exactly to a single-photon resonance is, due to absorption of the fundamental radiation, no good choice. Tuning to two- and three-photon resonances permits large resonance enhancements of the THG yield by up to four orders of magnitude with regard to the background signal.

The main technological challenge of this project was the setup of a laser system, which supplies continuously tunable mid-infrared laser pulses with pulse energies up to 2 mJ. Based upon a commercial optical parametric oscillator (OPO), we set up a three stage optical parametric amplifier chain. This allows stable operation and significantly reduces maintenance, when compared with typical pulsed mid-infrared laser sources, which usually include dye lasers. From transmission spectra in HCl we estimate a small spectral bandwidth  $\leq 100 \text{ MHz}$  (FWHM), i.e., only a factor of 2 above the Fourier transform limit. We reach peak intensities of up to  $450 \text{ MW/cm}^2$  at a pulse energy of 1.9 mJ and a pulse duration of 8 ns.

We compare the experimental results on the THG spectrum in HCl to a numerical simulation, which agrees well with the data. We systematically study and compare THG via two- and three-photon resonances in HCl. Two-photon resonances yield enhancement factors of more than three orders of magnitude with regard to off-resonant THG. We find, that saturation of the two-photon transition and resonance enhancements occur for laser intensities beyond  $100 \text{ MW/cm}^2$ , while we do not yet observe such saturation at our available laser intensities for the higher-order three-photon transition. Measurements of the THG signal vs. sample pressure confirm the quadratic dependence expected for a nonlinear optical process. At large pressures beyond a few 10 mbar collisional broadening leads to saturation of the signal vs. sample pressure. A detailed analysis of the spectral line shape shows an asymmetric, Fano-type line profile at lower gas pressures, which is due to interference between the resonant signal from the test gas and nonresonant background. The asymmetry vanishes at higher pressures due to collisional broadening, giving rise to a symmetric line profile. From the pressure dependence, we determine a detection limit for the THG approach in the HCl sample in the range of  $\leq 1 \text{ mbar}$ , corresponding to roughly  $3 \times 10^{13}$  molecules in the confocal volume of the driving laser field. This paves the way towards applications of the approach under realistic conditions of trace gas detection.

As an extension of our investigations in resonantly enhanced THG in HCl, we conducted first tests of resonantly enhanced sum frequency mixing (SFM) in HCl.

Here, we probe the vibrational two-photon resonance with near-infrared nanosecond radiation. With this approach we both benefit from resonance enhancement and from a lower detuning to the first excited electronic state of HCl. Also, the visible SFM signal is detectable with photomultiplier tubes. We conducted measurements with collimated probe radiation at 1064 nm wavelength. We identified the same two-photon resonances as with THG, albeit with large background signals, approximately one order of magnitude larger, than for THG. Due to this background we did not improve the detection limit for HCl molecules. The intensity dependence of the SFM signal shows the expected dependencies for SFM. The spectral linewidth of the two-photon resonance appears to be narrower, when measured with SFM. An analysis of the background signal indicates, that it is off-resonant SFM signal, which emerges from the CaF<sub>2</sub> windows of the gas cell, i.e., a technical artefact of our experimental setup.

Nevertheless, we conducted first of its kind comparisons of vibrational two-photon resonances with different two-photon resonant frequency conversion processes. We found in particular, that THG has the potential for realistic applications of molecule detection.

## Outlook

Future investigations will focus on two approaches: First, we will further investigate the optical background signal and improve the experimental setup for SFM to reduce the background. A possibility is a noncollinear focusing geometry, where the participating fields do not overlap on the gas cell windows. Another option is the replacement of the cell with a gas flow. With a laminar flow of sample molecules, diluted in nitrogen, measurements at atmospheric pressures are possible without windows close to the laser focus. With this technical precondition settled, we will systematically compare resonantly enhanced THG and SFM with coherent anti-Stokes Raman spectroscopy (CARS). The technical implementation for CARS is straightforward. We will utilise the continuously tunable near-infrared "signal" output of our optical parametric amplifiers as the Stokes field and the pump laser at 1064 nm to probe vibrational resonances with  $\Delta\nu = 1$ . The aim is to confirm, that THG and SFM perform significantly better than CARS for molecule detection at low absolute pressures.

Secondly, to prove the broader applicability of resonantly enhanced THG and SFM, we will also investigate other molecules. An estimation of the nonlinear susceptibility shows, that THG and SFM have resonant nonlinear susceptibilities in CO<sub>2</sub>, which are two orders of magnitude larger than for HCl (compare appendix C). As CO<sub>2</sub> has a lower rotational constant than HCl, we also expect larger variations of the ground state population with temperature. This enables temperature sensing, based on resonantly enhanced THG. For these measurements we need mid-infrared laser pulses with wavelengths up to 4.6  $\mu\text{m}$ . Hence, we will extend the capabilities of our laser system by integration of an existing home-made OPO, which provides (cw) seed radiation for idler wavelengths up to 4.6  $\mu\text{m}$ , into the optical parametric amplifier chain.

## Zusammenfassung

In dieser Arbeit wurden systematische experimentelle Studien zur resonant überhöhten Frequenzverdreifachung (THG) von schmalbandigen Laserpulsen im mittleren Infrarotbereich vorgestellt, welche geringe Verstimmungen zu Molekülresonanzen mit Chlorwasserstoffmolekülen (HCl) als Testgas aufweisen. Im Gegensatz zu etablierten Ansätzen der nichtlinearen Spektroskopie benötigt das Verfahren nur einen einzigen Laserstrahl, was die Anwendung erleichtert. Ein großer Vorteil des THG-Ansatzes ist, dass der Frequenzkonversionsprozess gleichzeitig in der Nähe von Ein-, Zwei- und Dreiphotonenresonanzen mit typischen Verstimmungen im Bereich von nur  $10 - 100 \text{ cm}^{-1}$  durchgeführt werden kann. Eine kleine Verstimmung zu einer Einphotonenresonanz ist aufgrund von Absorption der Fundamentalstrahlung keine gute Wahl. Zwei- und Dreiphotonenresonanzen ermöglichen die resonante Überhöhung der THG-Ausbeute um bis zu vier Größenordnungen im Vergleich zum Hintergrundsignal.

Die größte technologische Herausforderung dieses Projekts war der Aufbau eines Lasersystems, welches kontinuierlich durchstimmbare Laserpulse im mittleren Infrarot mit Pulsenergien bis zu 2 mJ liefert. Basierend auf einem kommerziellen optisch-parametrischen Oszillator (OPO) wurde ein dreistufiger optisch-parametrische Verstärker aufgebaut. Dieser ermöglicht einen stabilen Betrieb und reduziert den Wartungsaufwand erheblich im Vergleich zu typischen gepulsten Mittelinfrarot-Laserquellen, welche in der Regel Farbstofflaser inkludieren. Aus Transmissionsspektren in HCl konnte eine kleine spektrale Bandbreite  $\leq 100 \text{ MHz}$  (Halbwertsbreite) ermittelt werden. Dieser Wert ist nur um einen Faktor 2 größer als die Fourier-Transformationsgrenze. Es konnten Spitzenintensitäten von bis zu  $450 \text{ MW/cm}^2$  bei einer Pulsenergie von 1,9 mJ und einer Pulsdauer von 8 ns erreicht werden.

In einem Vergleich von experimentellen Ergebnisse des THG Spektrums in HCl mit einer numerischen Simulation konnte eine gute Übereinstimmung festgestellt werden. Es konnten Zwei- und Dreiphotonenresonanzen von HCl identifiziert werden. Insbesondere Zweiphotonenresonanzen ermöglichen Überhöhungsfaktoren von mehr als drei Größenordnungen im Vergleich zu nichtresonanter THG. Dabei tritt jedoch eine Sättigung des Zweiphotonenübergangs bei Laserintensitäten jenseits von  $100 \text{ MW/cm}^2$  auf. Eine solche Sättigung wird für einen Dreiphotonenübergang nicht beobachtet. Messungen des THG-Signals in Abhängigkeit vom Probedruck bestätigen die für einen nichtlinearen optischen Prozess erwartete quadratische Abhängigkeit für Drücke kleiner 10 mbar. Bei höheren Drücken führt die Druckverbreiterung zu einem stagnierenden THG-Signal. Eine detaillierte Analyse der spektralen Linienbreite zeigt ein asymmetrisches, Fano-artiges Linienprofil bei niedrigeren Gasdrücken. Dies ist auf Interferenz zwischen dem resonanten Signal des Testgases und dem nichtresonanten Hintergrundsignal zurückzuführen. Die Asymmetrie verschwindet bei höheren Drücken aufgrund von Druckverbreiterung und führt zu einem symmetrischen Linienprofil. Aus der Druckabhängigkeit lässt sich eine Nachweisgrenze für den THG-Ansatz in der HCl-Probe im Bereich von  $\leq 1 \text{ mbar}$  bestimmen. Dies entspricht etwa  $3 \times 10^{13}$  Molekülen im konfokalen Volumen des treibenden Laserfeldes. Diese

Resultate ebnen den Weg zu Anwendungen von resonant überhöhter THG, z.B. unter realistischen Bedingungen in der Spurengasdetektion.

Als Erweiterung der Untersuchungen zur resonant überhöhten THG in HCl wurden erste Tests zur resonant überhöhten Summenfrequenzmischung (SFM) in HCl durchgeführt. Hier wird eine Zweiphotonenresonanz in HCl mit Nanosekunden-Strahlung im nahen Infrarot nachgewiesen. Dieser Ansatz profitiert sowohl von der resonanten Überhöhung als auch von einer geringeren Verstimmung zum ersten angeregten elektronischen Zustand von HCl. Außerdem ist das sichtbare SFM-Signal mit Photomultipliern nachweisbar. Die Messungen wurden mit kollimierter Nachweis-Strahlung bei 1064 nm Wellenlänge durchgeführt. Es können die gleichen Zweiphotonenresonanzen wie bei THG identifiziert werden. Allerdings trat ein großes Hintergrundsignal auf, welches etwa eine Größenordnung größer war als bei den THG-Untersuchungen. Aufgrund dieses Hintergrundsignals konnte die Nachweisgrenze für HCl-Moleküle nicht verbessert werden. Die Intensitätsabhängigkeit des SFM-Signals zeigt die erwarteten Abhängigkeiten für SFM. Die spektrale Linienbreite der Zweiphotonenresonanz scheint schmaler zu sein, wenn sie mit SFM gemessen wird. Eine Analyse des Hintergrundsignals deutet darauf hin, dass es sich um ein nicht resonantes SFM-Signal handelt, welches aus den CaF<sub>2</sub>-Fenstern der Gaszelle stammt. Damit handelt es sich um ein technisches Artefakt des Versuchsaufbaus.

Nichtsdestotrotz konnte der erste Vergleich von Molekülresonanzen mit verschiedenen zweiphotonenresonanten Frequenzkonversionsprozessen erfolgreich durchgeführt werden. Insbesondere THG hat das Potenzial für realistische Anwendungen in der Moleküldetektion.

# Appendix

## A Refractive index of HCl

In our simulation, we explicitly calculate  $\chi^{(1)}$  according to Eqn. (1.12) with transmission moments, resonance frequencies and dephasing rates for HCl from the HITRAN database [32]. Note, that this calculation omits the contribution of the far-detuned electronic transitions in the UV range. To account for the latter, we analysed previous studies on the dispersion of HCl and determined the offset of refractive index to our simulation result. Fig. A.1 (a) shows the dispersion of HCl in the near-infrared spectral region, i.e., the relevant region for the harmonic wave. Part (b) of the figure gives the dispersion in the mid-infrared region, i.e., the relevant range for the fundamental radiation. Fig. A.1 (b) further shows the simulation result in the vibrational band  $\nu = 0 - 1$  (compare Sec. 2.2). As the simulation does not include the refractive index offset due to the UV transitions we added the low resolution values from Chamberlain *et al.* to the simulation values [82].

The linewidth of the one-photon resonances, which form the vibrational band, depends on the HCl pressure and temperature (compare also Sec. 3.4.1). While we include these parameters in our simulation of Eqn. (1.12), we also have to scale the refractive index offsets given in Fig. A.1. For this task we use a simple scaling law for HCl [82]

$$n(p, T) = 1 + \frac{p(n_0 - 1)}{1013 \text{ mbar} (1 + T 3.66 \times 10^{-3} \text{ }^\circ\text{C}^{-1})}, \quad (1)$$

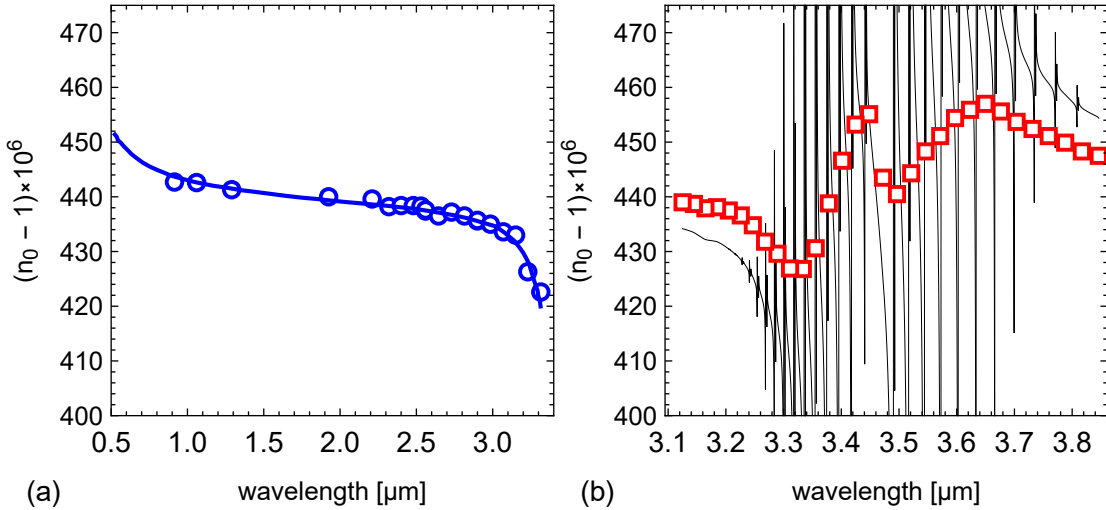


**Figure A.1:** Refractive index of HCl vs. wavelength. (a) Measurement data of Rollefson and Rollefson in the near-infrared spectral range, the blue line gives a fit of Kramers dispersion formula [81]. (b) Measurement data of Chamberlain *et al.* (red) in the mid-infrared spectral range [82]. The black line indicates our simulation result with offset correction. The HCl pressure is  $p = 1013.25$  mbar and temperature is  $T = 0$  °C.

with the refractive index at normal conditions  $n_0$  (1013 mbar, 0 °C) and the pressure  $p$  given in mbar and the temperature  $T$  in °C.

HCl has usually positive dispersion, i.e., the refractive index  $n(\lambda_{\text{THG}})$  at the THG wavelength  $\lambda_{\text{THG}} = \lambda_{\text{fund}}/3$  is should be larger than refractive index  $n(\lambda_{\text{fund}})$  for the fundamental wavelength  $\lambda_{\text{fund}}$ . However, in the mid-infrared spectral range rovibrational resonances define the dispersion of HCl. Hence, as Fig. A.1 suggests, we identify fundamental wavelengths, where HCl shows negative dispersion for the THG process. Therefore, multi-photon resonances in HCl might or might not contribute to the THG yield, based on the phase matching conditions, shown in Fig. A.1. For example, the fundamental wavelength in our experiments is around  $\lambda_1 = 3.5 \mu\text{m}$ . Hence, the THG wavelength is  $\lambda_3 = \lambda_1/3 = 1.17 \mu\text{m}$  and we find  $n(\lambda_3) - n(\lambda_1) \approx -3.9 \times 10^{-6}$  ( $p = 1013 \text{ mbar}$ ,  $T = 0 \text{ °C}$ ).

## B Pressure sensor

After the conduction of our measurements, which we presented in this work, we acquired a new pressure sensor (VSR, Thyracont). This sensor combines a piezo and a pirani sensor, and, hence, allows pressure measurements also for HCl pressures below 0.1 mbar. The sensor used in this work (P200, Siemens) only includes of a piezo element. Therefore, it provides reliable pressure readings only in a rough vacuum ( $> 1 \text{ mbar}$ ), as the manufacturer states a measurement uncertainty of 0.25 % of the measurement range, i.e., 1 bar. Hence, the sensor typically only has a resolution of 2.5 mbar. This value incorporates different zero offsets and repeatability.

To reevaluate our measurement results, we tested both sensors at vacuum conditions and filled the gas cell with nitrogen afterwards. According to the new Pirani sensor reading, we reach minimal pressures of 0.08 mbar, whereas the Siemens sensor gives a value of  $-1.2 \text{ mbar}$ . The negative value is an artefact of the linear characteristic of the sensor and our calibration. Depending on the initial ambient conditions we notice different offsets day-to-day. Hence, we add the absolute value of this offset to the pressure readings, as it is save to assume, that the absolute pressure is below the discretization limit of the sensor.

Fig. A.2 shows the comparison of both sensors for different nitrogen pressures.

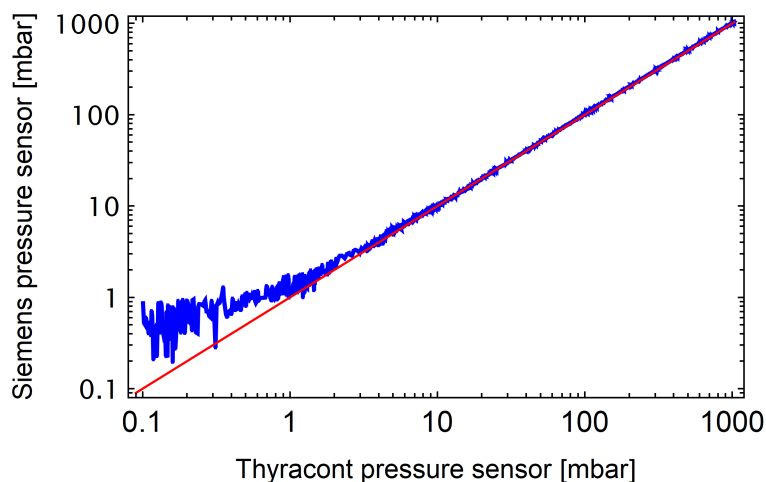


**Figure A.2:**  $N_2$  pressure, measured with the Siemens P200 sensor (as used in this work) vs.  $N_2$  pressure, measured with the Thyracont VSR sensor. The red line indicates unity. A deviation from this line indicates different readings from the pressure sensors. Note the double logarithmic scale.

Down to pressures in the range of few mbar we find a good agreement of both readings, as indicated by the red line. At a  $N_2$  pressure of 1 mbar, the reading of the Siemens sensor is already  $\approx 30\%$  larger than the value determined with the Thyracont sensor. This deviation increases significantly for lower pressures. Also, we observe larger fluctuations of the reading with the Siemens sensor. In conclusion, the pressure sensor, which we used throughout this work is adequate down to HCl pressures of 1 mbar. The new sensor will improve the accuracy of the determination of the detection limit for THG and SFM.

## C Simulation results for $CO_2$

Carbon dioxide ( $CO_2$ ) is a molecule with high relevance for combustion processes, environmental sensing, and atmospheric science. Hence, we estimate the nonlinear susceptibility for two-photon resonant THG and SFM, and compare our results with an implementation of (ns) CARS. We restrict our analysis to the vibrational asymmetric stretch mode  $\nu_3$ , which corresponds to absorption lines with fundamental wavelengths in the range of  $4.3\ \mu\text{m}$ . Tab. A.1 summarizes the parameters necessary to calculate the nonlinear susceptibility  $\chi^{(3)}$  for the three processes. We find, that  $\chi^{(3)}(\text{THG})$  is two orders of magnitude larger than in HCl, whereas  $\chi^{(3)}(\text{SFM})$  and  $\chi^{(3)}(\text{CARS})$  are only  $\approx 1$  order of magnitude larger than in HCl (see Tab. 4.1). Hence, we expect, that THG and SFM are sensitive tools for trace gas analysis of  $CO_2$  molecules.

**Table A.1:** Calculation of the nonlinear susceptibility for resonantly enhanced THG, CARS and SFM for  $CO_2$ . Parameters:  $CO_2$  pressure  $p = 100\ \text{mbar}$ , number density  $\rho = 1.8 \times 10^{23}\ \text{m}^{-3}$ , resonant linewidth  $\Gamma_{20} = 0.72\ \text{GHz}$  [32, 49, 83].

method	unit	THG	CARS	SFM
$\lambda_1$	nm	4300 (fund)	1064 (pump)	4300 (fund)
$\lambda_2$	nm	-	1418 (S)	1064 (probe)
$\lambda_{\text{signal}}$	nm	1433	851	712
$\Delta_{1P}$	$\text{cm}^{-1}$	12	63495	12
$\Delta_{2P}$	$\text{cm}^{-1}$	0	0	0
$\Delta_{3P}$	$\text{cm}^{-1}$	-17	61255	58950
$\mu_{01}$	$10^{-30}\ \text{Cm}$	0.8	3.5	0.8
$\mu_{12}$	$10^{-30}\ \text{Cm}$	1.1	3.5	1.1
$\mu_{23}$	$10^{-30}\ \text{Cm}$	1.3	3.5	3.5
$\mu_{03}$	$10^{-30}\ \text{Cm}$	0.0018	3.5	3.5
$ \chi^{(3)} $	$\text{pm}^2/\text{V}^2$	2091	8	3129

---

## Bibliography

- [1] R. L. Farrow and D. J. Rakestraw. *Detection of trace molecular species using degenerate four-wave mixing*. *Science* **257**, 1894–1900 (1992).
- [2] V. Ebert, C. Schulz, H.-R. Volpp, J. Wolfrum, and P. Monkhouse. *Laser diagnostics of combustion processes: From chemical dynamics to technical devices*. *Isr. J. Chem.* **39**, 1–24 (1999).
- [3] M. R. Leahy-Hoppa, J. Miragliotta, R. Osiander, J. Burnett, Y. Dikmelik, C. McEnnis, and J. B. Spicer. *Ultrafast laser-based spectroscopy and sensing: Applications in LIBS, CARS, and THz spectroscopy*. *Sensors* **10**, 4342–4372 (2010).
- [4] J.-X. Cheng and X. S. Xie. *Coherent anti-Stokes Raman scattering microscopy: Instrumentation, theory, and applications*. *J. Phys. Chem. B* **108**, 827–840 (2004).
- [5] S. A. Druet and J. P. E. Taran. *Cars spectroscopy*. *Prog. Quantum Electron.* **7**, 1–72 (1981).
- [6] J. Wolfrum. *Lasers in combustion: From basic theory to practical devices*. *Symp. Combust.* **27**, 1–41 (1998).
- [7] M. Müller and A. Zumbusch. *Coherent anti-Stokes Raman scattering microscopy*. *ChemPhysChem* **8**, 2156–2170 (2007).
- [8] R. W. Boyd. *Nonlinear optics* 3rd ed. (Academic Press, New York, 2008).
- [9] P. D. Maker and R. W. Terhune. *Study of optical effects due to an induced polarization third order in the electric field strength*. *Phys. Rev.* **137**, A801–A818 (1965).
- [10] D. M. Bloom, J. T. Yardley, J. F. Young, and S. E. Harris. *Infrared up-conversion with resonantly two-photon pumped metal vapors*. *Appl. Phys. Lett.* **24**, 427–428 (1974).
- [11] G. O. Clay, A. C. Millard, C. B. Schaffer, J. Aus-der Au, P. S. Tsai, J. A. Squier, and D. Kleinfeld. *Spectroscopy of third-harmonic generation: evidence for resonances in model compounds and ligated hemoglobin*. *J. Opt. Soc. Am. B* **23**, 932 (2006).
- [12] R. Carriles, D. N. Schafer, K. E. Sheetz, J. J. Field, R. Cisek, V. Barzda, A. W. Sylvester, and J. A. Squier. *Invited review article: Imaging techniques for harmonic and multiphoton absorption fluorescence microscopy*. *Rev. Sci. Instrum.* **80**, 081101 (2009).
- [13] C. Y. She and K. W. Billman. *Infrared-pumped third-harmonic and sum-frequency generation in diatomic molecules*. *Appl. Phys. Lett.* **27**, 76–79 (1975).
- [14] M. J. Pellin and J. T. Yardley. *Resonanceenhanced infrared fourwave mixing by infraredactive molecules*. *Appl. Phys. Lett.* **29**, 304–307 (1976).
- [15] H. Kildal and T. F. Deutsch. *Infrared third-harmonic generation in molecular gases*. *IEEE J. Quantum Electron.* **12**, 429–435 (1976).

- [16] T. A. Reichardt and R. P. Lucht. *Interaction of closely spaced resonances in degenerate four-wave-mixing spectroscopy*. J. Opt. Soc. Am. B **14**, 2449 (1997).
- [17] V. Petrov. *Frequency down-conversion of solid-state laser sources to the mid-infrared spectral range using non-oxide nonlinear crystals*. Prog. Quantum Electron. **42**, 1–106 (2015).
- [18] Y. Miyamoto, H. Hara, T. Hiraki, T. Masuda, N. Sasao, S. Uetake, A. Yoshimi, K. Yoshimura, and M. Yoshimura. *Vibrational excitation of hydrogen molecules by two-photon absorption and third-harmonic generation*. J. Phys. B At. Mol. Opt. Phys. **51**, 015401 (2018).
- [19] V. S. Dolzhikov, Y. S. Dolzhikov, A. A. Makarov, V. G. Movshev, and E. A. Ryabov. *Two-photon resonance spectroscopy of vibrational transitions in molecules under four-wave frequency mixing conditions*. Sov. J. Quantum Electron. **16**, 580–588 (1986).
- [20] A. A. Makarov and E. A. Ryabov. *On a half-forgotten but very powerful method for coherent spectroscopy of molecules*. Uspekhi Fiz. Nauk **189**, 271–280 (2019).
- [21] A. J. Traverso, B. Hokr, Z. Yi, L. Yuan, S. Yamaguchi, M. O. Scully, and V. V. Yakovlev. *Two-photon infrared resonance can enhance coherent Raman scattering*. Phys. Rev. Lett. **120**, 63602 (2018).
- [22] G. S. He. *Nonlinear optics and photonics* (Oxford University Press, Oxford, 2014).
- [23] J. Reintjes. *Nonlinear optical parametric processes in liquids and gases*, 466 (Academic Press, Orlando, 1984).
- [24] J. A. Armstrong, N. Bloembergen, J. Ducuing, and P. S. Pershan. *Interactions between light waves in a nonlinear dielectric*. Phys. Rev. **127**, 1918–1939 (1962).
- [25] G. Bjorklund. *Effects of focusing on third-order nonlinear processes in isotropic media*. IEEE J. Quantum Electron. **11**, 287–296 (1975).
- [26] H. Kogelnik and T. Li. *Laser beams and resonators*. Appl. Opt. **5**, 1550–1567 (1966).
- [27] R. B. Miles and S. E. Harris. *Optical third-harmonic generation in alkali metal vapors*. IEEE J. Quantum Electron. **9**, 470–484 (1973).
- [28] N. Stewen. *Simulation von resonant überhöhter Erzeugung der dritten Harmonischen in HCl*. BSc thesis (TU Darmstadt, 2020).
- [29] A. Spott, A. Becker, and A. Jaroń-Becker. *Transition from perturbative to nonperturbative interaction in low-order-harmonic generation*. Phys. Rev. A - At. Mol. Opt. Phys. **91**, 1–4 (2015).
- [30] A. M. Morrison, T. Liang, and G. E. Douberly. *Automation of an Aculight continuous-wave optical parametric oscillator*. Rev. Sci. Instrum. **84**, 013102 (2013).
- [31] N. Nguyen. *Automatisierung eines optisch parametrischen Oszillators für mittel-infrarote Strahlung*. BSc thesis (TU Darmstadt, 2020).
- [32] I. E. Gordon et al. *The HITRAN2016 molecular spectroscopic database*. J. Quant. Spectrosc. Radiat. Transf. **203**, 3–69 (2017).

- 
- [33] J. Eichler, L. Dünkel, and B. Eppich. *Die Strahlqualität von Lasern*. Laser Tech. J. **1**, 63–66 (2004).
- [34] S. Otto. *Aufbau und Charakterisierung eines optisch parametrischen Verstärkers für mittel-infrarote ns-Pulse*. MSc thesis (TU Darmstadt, 2018).
- [35] G. Arisholm, R. Paschotta, and T. Sudmeyer. *Limits to the power scalability of high-gain optical parametric oscillators and amplifiers*. Conf. Lasers Electro-Optics Eur. - Tech. Dig. **21**, 262 (2003).
- [36] Q. W. Song, C.-p. Zhang, and P. J. Talbot. *Self-defocusing, self-focusing, and speckle in LiNbO<sub>3</sub> and LiNbO<sub>3</sub>:Fe crystals*. Appl. Opt. **32**, 7266 (1993).
- [37] J. Rams, A. Alcázar-De-Velasco, M. Carrascosa, J. M. Cabrera, and F. Agulló-López. *Optical damage inhibition and thresholding effects in lithium niobate above room temperature*. Opt. Commun. **178**, 211–216 (2000).
- [38] Y. Furukawa, K. Kitamura, S. Takekawa, K. Niwa, and H. Hatano. *Stoichiometric Mg:LiNbO<sub>3</sub> as an effective material for nonlinear optics*. Opt. Lett. **23**, 1892 (1998).
- [39] A. Smith. *SNLO nonlinear optics code available from AS-Photonics, Albuquerque, NM, Software*. 2015.
- [40] Y. Miyamoto, H. Hara, T. Masuda, T. Hiraki, N. Sasao, and S. Uetake. *Injection-seeded tunable mid-infrared pulses generated by difference frequency mixing*. Jpn. J. Appl. Phys. **56**, 032101 (2017).
- [41] G. F. Adams and C. F. Chabalowski. *Quantum chemical study of the potential energy curves and electronic transition strengths in HCl, XeCl, and HCl + Xe*. J. Phys. Chem. **98**, 5878–5890 (1994).
- [42] H. Akagi, T. Otobe, A. Staudte, A. Shiner, F. Turner, R. Dörner, D. M. Villeneuve, and P. B. Corkum. *Laser tunnel ionization from multiple orbitals in HCl*. Science **325**, 1364–1367 (2009).
- [43] S. Tilford, M. Ginter, and J. T. Vanderslice. *Electronic spectra and structure of the hydrogen halides*. J. Mol. Spectrosc. **33**, 505–519 (1970).
- [44] A. A. Stec, T. R. Hull, K. Lebek, J. A. Purser, and D. A. Purser. *The effect of temperature and ventilation condition on the toxic product yields from burning polymers*. Fire Mater. **32**, 49–60 (2008).
- [45] X. Ren, R. Sun, H. H. Chi, X. Meng, Y. Li, and Y. A. Levendis. *Hydrogen chloride emissions from combustion of raw and torrefied biomass*. Fuel **200**, 37–46 (2017).
- [46] G. E. Hartzell. *Overview of combustion toxicology*. Toxicology **115**, 7–23 (1996).
- [47] Y. L. Yung and W. B. Demore. *Photochemistry of the stratosphere of Venus: Implications for atmospheric evolution*, 199–247 (1982).
- [48] J. L. Dunham. *The energy levels of a rotating vibrator*. Phys. Rev. **41**, 721–731 (1932).
- [49] K. P. Huber and G. Herzberg. *Molecular spectra and molecular structure: IV Constants of diatomic molecules* (Van Nostrand Reinhold, New York, 1979).
- [50] T. Parekunnel, T. Hirao, R. J. Le Roy, and P. F. Bernath. *FTIR emission spectra and molecular constants for DCl*. J. Mol. Spectrosc. **195**, 185–191 (1999).
-

- [51] A. Pine, A. Fried, and J. Elkins. *Spectral intensities in the fundamental bands of HF and HCl*. J. Mol. Spectrosc. **109**, 30–45 (1985).
- [52] H. Haken and H. C. Wolf. *Molekülphysik und Quantenchemie* (Springer-Verlag, Berlin/Heidelberg, 2006).
- [53] A L’Huillier, L. A. Lompré, M. Ferray, X. F. Li, G. Mainfray, and C. Manus. *Third-harmonic generation in Xenon in a pulsed jet and a gas cell*. Europhys. Lett. **5**, 601–605 (1988).
- [54] I. H. Malitson. *A redetermination of some optical properties of calcium fluoride*. Appl. Opt. **2**, 1103 (1963).
- [55] J. F. Kinder, F. Cipura, and T. Halfmann. *Detection of HCl molecules by resonantly enhanced third-harmonic generation, driven by midinfrared laser pulses*. Phys. Rev. A **103**, 052808 (2021).
- [56] E. A. Stappaerts. *Limitations and optimization of (near) two-photon-resonant frequency up-converters*. IEEE J. Quantum Electron. **15**, 110–118 (1979).
- [57] H. Scheingraber and C. R. Vidal. *Near resonant third harmonic generation*. Opt. Commun. **38**, 75–80 (1981).
- [58] A. F. Linskens, I. Holleman, N. Dam, and J. Reuss. *Two-photon Rabi oscillations*. Phys. Rev. A - At. Mol. Opt. Phys. **54**, 4854–4862 (1996).
- [59] J. F. Ward and A. V. Smith. *Saturation of two-photon-resonant optical processes in cesium vapor*. Phys. Rev. Lett. **35**, 653–656 (1975).
- [60] K. M. Murdoch, D. E. Thompson, K. A. Meyer, and J. C. Wright. *Modeling window contributions to four-wave mixing spectra and measurements of third-order optical susceptibilities*. Appl. Spectrosc. **54**, 1495–1505 (2000).
- [61] U. Fano. *Effects of configuration interaction on intensities and phase shifts*. Phys. Rev. **124**, 1866–1878 (1961).
- [62] A. C. Eckbreth. *Laser diagnostics for combustion temperature and species*, 305–364 (CRC Press, 1996).
- [63] Z. W. Sun, Z. S. Li, B. Li, M. Aldén, and P. Ewart. *Detection of C<sub>2</sub>H<sub>2</sub> and HCl using mid-infrared degenerate four-wave mixing with stable beam alignment: Towards practical in situ sensing of trace molecular species*. Appl. Phys. B Lasers Opt. **98**, 593–600 (2010).
- [64] R. F. Curl and F. K. Tittel. *7 Tunable infrared laser spectroscopy*. Annu. Rep. Prog. Chem., Sect. C Phys. Chem. **98**, 219–272 (2002).
- [65] D. C. Scott, R. L. Herman, C. R. Webster, R. D. May, G. J. Flesch, and E. J. Moyer. *Airborne laser infrared absorption spectrometer (ALLAS-II) for in situ atmospheric measurements of N<sub>2</sub>O, CH<sub>4</sub>, CO, HCl, and NO<sub>2</sub> from balloon or remotely piloted aircraft platforms*. Appl. Opt. **38**, 4609 (1999).
- [66] J. Kiefer and P. Ewart. *Laser diagnostics and minor species detection in combustion using resonant four-wave mixing*. Prog. Energy Combust. Sci. **37**, 525–564 (2011).
- [67] M. Aldén, P.-E. Bengtsson, H. Edner, S. Kröll, and D. Nilsson. *Rotational CARS: a comparison of different techniques with emphasis on accuracy in temperature determination*. Appl. Opt. **28**, 3206 (1989).

- 
- [68] Z. W. Sun, Z. S. Li, B. Li, and M. Aldén. *Flame temperature diagnostics with water lines using mid-infrared degenerate four-wave mixing*. *J. Raman Spectrosc.* **42**, 1828–1835 (2011).
- [69] B. J. Drouin. *Temperature dependent pressure-induced lineshape of the HCl J=10 rotational transition in nitrogen and oxygen*. *J. Quant. Spectrosc. Radiat. Transf.* **83**, 321–331 (2004).
- [70] G. Li, I. E. Gordon, P. G. Hajigeorgiou, J. A. Coxon, and L. S. Rothman. *Reference spectroscopic data for hydrogen halides, Part II: The line lists*. *J. Quant. Spectrosc. Radiat. Transf.* **130**, 284–295 (2013).
- [71] J. Olivero and R. Longbothum. *Empirical fits to the Voigt line width: A brief review*. *J. Quant. Spectrosc. Radiat. Transf.* **17**, 233–236 (1977).
- [72] A. S. Pine and A. Fried. *Self-broadening in the fundamental bands of HF and HCl*. *J. Mol. Spectrosc.* **114**, 148–162 (1985).
- [73] R. H. Dicke. *The effect of collisions upon the Doppler width of spectral lines*. *Phys. Rev.* **89**, 472–473 (1953).
- [74] D. Ramachandra Rao and T. Oka. *Dicke narrowing and pressure broadening in the infrared fundamental band of HCl perturbed by Ar*. *J. Mol. Spectrosc.* **122**, 16–27 (1987).
- [75] A. S. Pine and J. P. Looney. *N<sub>2</sub> and air broadening in the fundamental bands of HF and HCl*. *J. Mol. Spectrosc.* **122**, 41–55 (1987).
- [76] N. V. Vitanov, B. W. Shore, L. Yatsenko, K. Böhmer, T. Halfmann, T. Rickes, and K. Bergmann. *Power broadening revisited: Theory and experiment*. *Opt. Commun.* **199**, 117–126 (2001).
- [77] M. De Rosa, C. Nardini, C. Piccolo, C. Corsi, and F. D’Amato. *Pressure broadening and shift of transitions of the first overtone of HCl*. *Appl. Phys. B* **72**, 245–248 (2001).
- [78] L. Meyer. *Resonant überhöhte Vierwellenmischung im Mittelinfrarot zum Nachweis von HCl-Molekülen*. BSc thesis (TU Darmstadt, 2020).
- [79] B. C. Stuart, M. D. Feit, A. M. Rubenchik, B. W. Shore, and M. D. Perry. *Laser-induced damage in dielectrics with nanosecond to subpicosecond pulses*. *Phys. Rev. Lett.* **74**, 2248–2251 (1995).
- [80] G. Li, A. Serdyukov, M. Gisi, O. Werhahn, and V. Ebert. *FTIR-based measurements of self-broadening and self-shift coefficients as well as line strength in the first overtone band of HCl at 1.76 $\mu$ m*. *J. Quant. Spectrosc. Radiat. Transf.* **165**, 76–87 (2015).
- [81] R. Rollefson and A. H. Rollefson. *The optical dispersion of HCl in the infrared*. *Phys. Rev.* **48**, 779–785 (1935).
- [82] J. E. Chamberlain, F. D. Findlay, and H. A. Gebbie. *The measurement of the refractive index spectrum of HCl gas in the near infrared using a Michelson interferometer*. *Appl. Opt.* **4**, 1382 (1965).
- [83] J. W. Johns. *Absolute intensity and pressure broadening measurements of CO<sub>2</sub> in the 4.3- $\mu$ m region*. *J. Mol. Spectrosc.* **125**, 442–464 (1987).
-

## Publications and contributions to conferences

### Publications in peer-reviewed journals

- J. F. Kinder, F. Cipura, T. Halfmann:  
*Detection of HCl molecules by resonantly enhanced third harmonic generation, driven by mid-infrared laser pulses*  
Physical Review A 103, 052808 (2021)

### Manuscripts in preparation

- J. F. Kinder, B. Moneke, T. Halfmann:  
*Optical parametric oscillator and amplifier providing tunable, narrowband nanosecond laser pulses in the mid-infrared with mJ pulse energy*

### Posters on international conferences

- J. F. Kinder, T. Halfmann:  
*Detection of HCl molecules by resonantly enhanced third harmonic generation in the mid-IR*  
HICONO 2019 - ICFO, Castelldefels (Barcelona), Spain, September 2019

# Supervisions and contributions to teaching

## Master's thesis

- Susanne Otto, "*Aufbau und Charakterisierung eines optisch parametrischen Verstärkers für mittel-infrarote ns-Pulse*", 2018
- Florian Pelz, "*Aufbau und Charakterisierung eines optisch-parametrischen Verstärkers und Detektion der dritten Harmonischen in HCl*", 2019

## Bachelor's thesis

- Niklas Stewen, "*Simulation von resonant überhöhter Erzeugung der dritten Harmonischen in HCl*", 2020
- Nam Nguyen, "*Automatisierung eines optisch parametrischen Oszillators für mittelinfrarote Strahlung*", 2020
- Luca Meyer, "*Resonant überhöhte Vierwellenmischung im Mittelinfrarot zum Nachweis von HCl-Molekülen*", 2020

## Internships and laboratory courses

- Supervision of the advanced lab course "Laserresonator" (10/2017 - 02/2021)
- Supervision of laboratory internship "Schülerpraktikum"
  - Luca Geissler, "*Infrarot-Spektroskopie in Chlorwasserstoff*", TU Darmstadt, 2018
- Supervision of laboratory internship "Miniforschung"
  - Nam Nguyen, "*Ansteuerung und Charakterisierung eines Piezo-Spiegels zur Anpassung der Resonatorlänge eines optisch-parametrischen Oszillators*", TU Darmstadt, 2020

## Contributions to teaching

- Supervision of exercise groups "Experimentalphysik I" and "Experimentalphysik II" (01/2015 - 09/2016)
- Supervision of the talk "*Nd:YAG-Laser: Strahlprofilanalyse und Formung*" in the seminar Laserphysik & Lasertechnologie, 2020
- Labtours 2016 - 2020



## Erklärung gemäß §9 Promotionsordnung

Hiermit versichere ich, dass ich die vorliegende Dissertation selbstständig angefertigt und keine anderen als die angegebenen Quellen und Hilfsmittel verwendet habe. Alle wörtlichen und paraphrasierten Zitate wurden angemessen kenntlich gemacht. Die Arbeit hat bisher noch nicht zu Prüfungszwecken gedient.

Darmstadt, 30. September 2021

---

(Jan Frederic Kinder)